High Resolution Soft X-ray Fourier Transform Holography

vorgelegt von
Jan Geilhufe, M. Sc.
aus Freiberg (Sachsen)

Von der Fakultät II – Mathematik und Naturwissenschaften
der Technischen Universität Berlin
zur Erlangung des akademischen Grades

Doktor der Naturwissenschaften
– Dr. rer. nat. –

genehmigte Dissertation

Promotionsausschuss:

Vorsitzender: Prof. Dr. Mario Dähne
1. Gutachter: Prof. Dr. Stefan Eisebitt
2. Gutachter: Prof. Dr. Thomas Wilhein

Tag der wissenschaftlichen Aussprache: 24. November 2014

Berlin 2015

D83

To my wife, O Teemane yame! Ke a leboga. Pula!

Abstract

Fourier transform holography is a coherent, lensless imaging method. In the most common soft X-ray implementation of Fourier transform holography, the source of the phase encoding reference beam is a small pinhole which is integrated into a metal film adjacent to an object aperture that defines the field-of-view. By illuminating this integrated mask with coherent X-rays, a hologram can be recorded in the far-field. The reconstruction of the exit wave in the object aperture is retrieved by Fourier transforming the hologram. While this configuration is very robust against sample drifts and vibrations, the efficiency is limited by the reference pinhole. Smaller reference pinholes improve the resolution whereas the reference signal on the detector and ultimately the image contrast in the reconstruction diminishes. The choice of the reference pinhole size is therefore a compromise that trades image resolution for photon efficiency.

The first part of this thesis contains a theoretical discussion of the imaging properties for X-ray Fourier transform holography (FTH) and derives a model for the determination of reasonable pinhole diameters that ensure photon efficient imaging. Typical imaging artifacts are characterized and strategies for their prevention are discussed. Two of these strategies can additionally be utilized to enhance the spatial resolution for certain configurations of reference pinhole based FTH. The findings are successfully verified by a proof-of-principle experiment.

The second part presents a new approach that replaces the reference pinhole by a Fresnel zone plate lens (FZP). The method drastically enhances the signal strength of the reference beam and effectively decouples the spatial resolution in the reconstruction from image contrast. Related to the FZP diffraction orders, the method yields several differently strong defocused reconstructions which superpose along the beam axis. The FZP diffraction efficiency is much improved by combining several focal order reconstructions which are individually refocused by numeric wave field propagation. To separate a focused reconstruction of a particular FZP focal order from the remaining defocused reconstructions, a novel algorithm is proposed. The superiority of the FZP based reconstruction over the conventional pinhole reconstruction is experimentally demonstrated.

The extraction of depth information from three-dimensional specimen imaged by conventional FTH with pinhole references is discussed and experimentally demonstrated in the third part. The approach exploits the holographically encoded phase information from a hologram of an artificial three-dimensional test structure. Object features outside the depth-of-field are numerically refocused by propagating the reconstructed object wave along the beam axis into focus. Contrary to tomographic approaches, a three-dimensional model of the test structure is obtained from a single view measurement.

Zusammenfassung

Fourier-Transformationsholographie ist eine linsenlose Abbildungsmethode, die sich ausgezeichnet für Experimente mit kohärenten Röntgenstrahlen eignet. Eine gebräuchliche Implementierung von Fourier-Transformationsholographie für kohärente Röntgenstrahlung (FTH) baut auf einem integrierten Maskendesign auf. Dabei maskiert ein absorbierender Metallfilm die Objektebene. Ein kleines Pinhole in dieser Maske dient als Quelle für den Referenzstrahl. Das Bildfeld ist durch eine Objektapertur definiert, die auf der Maske neben dem Referenzpinhole integriert wird. Das Hologramm entsteht durch Interferenz zwischen Objekt- und Referenzwelle und wird durch einen Detektor im Fernfeld aufgenommen. Aufgrund dieses integrierten Maskendesigns reagiert FTH außerordentlich tolerant auf Vibrationen und Verschiebungen der Probe relativ zum Strahl. Ein Nachteil dieser Konfiguration ist jedoch, dass die Größe des Referenzpinholes die Photoneneffizienz limitiert. Kleine Referenzdurchmesser verbessern einerseits die Auflösung, schwächen jedoch auch das Referenzsignal und verschlechtern dadurch den Bildkontrast in der Rekonstruktion. Die Wahl der Referenzlochgröße erfolgt daher oftmals als Kompromiss indem die gewünschten Auflösung gegen die erforderlichen Photoneneffizienz abgewogen wird.

Im ersten Teil dieser Arbeit geht es um die Charakterisierung von FTH Systemen mit Pinholereferenzen. Dabei wird die theoretisch mögliche Abbildungsleistung in Abhängigkeit von verschieden FTH Designparametern diskutiert. Mit den Erkenntnissen aus dieser Diskussion wird ein Ansatz zur Bestimmung einer idealen Referenzlochgröße für FTH Experimente abgeleitet. Ein weiterer Schwerpunkt dieses Teils der Arbeit ist die Charakterisierung von für bestimmte FTH Konfigurationen typische Bildartefakte sowie deren Beseitigung. Abgesehen von der Beseitigung der Bildartefakte, ermöglichen zwei der vorgestellten Strategien dabei eine Erhöhung der räumlichen Auflösung in der Rekonstruktion. Die Erkenntnisse aus diesem Abschnitt konnten durch ein FTH Experiment mit kohärenter Röntgenstrahlung bestätigt werden.

Der zweite Teil der Arbeit beschäftigt sich mit einer neuen Methode zur Effizienzsteigerung von FTH. Bei dieser Methode wird sowohl die Photoneneffizienz, als auch die theoretisch erreichbare, räumliche Auflösung erhöht, indem anstatt eines Pinholes eine *Fresnel Zonenplatte* (FZP) als Quelle für den Referenzstrahl genutzt wird. Abgesehen von der erhöhten Effizienz, hat diese Methode den Vorteil, dass die räumlichen Auflösung in der Rekonstruktion unabhängig vom Bildkontrast ist. Im Gegensatz zum konventionellen Ansatz mit Pinholereferenzen, liefert dieses Verfahren für jede FZP Beugungsordnung eine Rekonstruktion. Diese Rekonstruktionen sind verschieden stark defokussiert und überlagern sich auf der Strahlachse. Die Effizienz der verwendeten FZP-Referenz kann weiterhin gesteigert werden, indem mehrere Rekonstruktionen von verschieden Bergungs-

ordnungen kombiniert werden. Dazu können die Rekonstruktion der verschiedenen FZP Ordnung individuell refokussiert werden, indem die rekonstruierte Objektwelle numerisch entlang der Strahlachse propagiert wird. Der fokussierte Anteil wird dabei durch einen neuartigen Ansatz vom defokussierten Anteil der übrigen Beugungsordnungen getrennt. Die gesteigerte Effizienz der FZP Referenz gegenüber dem konventionellen Referenzpinhole konnte experimentell verifiziert werden.

Ein dritter Schwerpunkt der Arbeit ist die Extraktion von Tiefeninformationen von konventionellen Fourier-Transformationhologrammen dreidimensionaler Testobjekte. Der experimentell gezeigte Ansatz nutzt die holographisch encodierten Phaseninformationen, um die rekonstruierte Objektwelle numerisch entlang der Strahlachse zu propagieren. Anteile der Probe die außerhalb des Schärfentiefebereichs liegen werden so refokussiert. Auf diese Art kann das Testobjekt vermessen und dreidimensional dargestellt werden. Im Gegensatz zu tomographischen Verfahren werden dabei die Tiefeninformationen der Probe aus einer einzigen Perspektive gewonnen.

Contents

List of Figures

Acronyms

CCD	charge-coupled device
EUV	extreme ultraviolet
FEL	free-electron laser
FTH	X-ray Fourier transform holography
FZP	Fresnel zone plate
HHG	high harmonic generation
NA	numerical aperture
PSF	point-spread function
MTF	modulation transfer function
PhTF	phase transfer function
FWHM	full width at half maximum
FIB	focused ion beam

1 Introduction and motivation

The development of scientific theories that formed the present understanding of our world, considerably relied on microscopic imaging. Simple microscopes used as early as in the 17^{th} century were nothing more than magnifying glasses (cf. *van Leeuwenhoek microscope*) which already reached magnifications of 270 and led to fundamental insights such as the discovery of the red blood cells [Bur01]. Since then, microscopy evolved into numerous techniques, utilizing not only photons as a probe but also atomic forces, electrons or even neutrons. Modern microscopes are capable to resolve single atoms and to give insight into ultra-fast processes at nanometer resolution. Furthermore, present day microscopy can be used to visualize magnetic fields or to map distributions of elements or molecules.

Conventional light microscopy in the visible spectrum relies on refractive lenses and the resolution limit is in the order of the wavelength of the illumination light. In this spectral region, the photon energies are resonant to the valance electron transitions. In order to perform element specific experiments, it is necessary to increase the photon energy to probe the core electrons with higher binding energies. The spectral band of electromagnetic radiation that covers primary atomic resonances of numerous elements extends from extreme ultraviolet (EUV) radiation (30eV) to soft X-rays ($\approx$ 4keV). Photons within this energy band provide accurate means for element specific experiments such as magnetic imaging or elemental and chemical identification for instance. Furthermore, the wavelength in this spectral region is much decreased compared to the visible spectrum, facilitating significantly higher resolution limits. On the other side, the large number of atomic resonances lead to short absorption lengths in condensed matter of typically around one micrometer or less. Experiments relying on the EUV/soft-X-ray spectrum of photon energies are therefore performed in an evacuated environment. Additionally, the materials refractive index for these energies is close to unity and significant refraction can not be obtained within one absorption length [Att07].

For this reason, microscopy with soft X-rays can not rely on refractive lenses to form real spaces images. At EUV energies, image formation is oftentimes provided by curved reflective, multilayer optics. Common soft X-ray microscopes however, rely on circular diffraction gratings called Fresnel zone plate (FZP). Soft X-ray microscopy with FZPs is a powerful method that yields high quality images with record resolution and strong contrast over a large field of view. The measurement can be evaluated instantaneously as the real space image is directly retrieved from the detector and does not necessitate further processing [Att07]. While lens based techniques have pioneered soft X-ray microscopy, the application of FZPs has also disadvantages for some applications.

The fabrication of state of the art FZPs is very challenging and the implementation

into the experiment is mechanically difficult due to short FZP focal lengths. State of the art FZPs have focal lengths of only a few hundred micro meter [Cha12] and need to be positioned in close proximity of the object. The positioning of the FZP relative to the object needs to be very accurate and robust in order to avoid motion blur caused by drifts or vibrations. Access to the sample is much restricted and it is difficult to implement special sample environments such as cryostats, heaters or magnetic fields in the experiment. Also for time resolved studies, FZP based imaging methods are often disadvantageous. Apart from the fact that it is very difficult to reach the sample with an optical pump laser, time resolved experiments are often performed at free-electron laser (FEL) facilities in a *diffract-before-destruct* approach [Cha06a; Sei10]. Such experiments utilize a very bright, ultra-short and destructive X-ray pulse to capture the diffraction pattern just before destruction takes place. This is possible since the destruction of the sample by the illumination pulse occurs at timescales much longer than the time the scattered light wave is propagating to the detector. For common lens based, soft X-ray microscopes, such experiments bear the risk that the illumination pulse destroys not only the sample but also the FZP.

Imaging of nanoscopic structures and their dynamic behavior on ever shorter timescales is an emerging research area of multidisciplinary importance. For such experiments, the application of FZPs is impractical or even impossible and lensless approaches are an alternative. X-ray Fourier transform holography (FTH) is a lensless imaging technique that attracted much attention in recent years [Eis04]. The method found its application mainly in the research of magnetic nano-structures [Gün08; Gün10; Hau08; Pfa11] but also of biological specimen [Gue09; Gue10; Gue12; Mar08]. In FTH, the interference pattern of the scattered wave field from the sample and an additional reference wave is directly recorded on a two-dimensional detector. The reference wave that encodes the phase information originates from a small aperture that is fabricated into an X-ray opaque metal film, next to an object aperture defining the field of view. The image is reconstructed by a Fourier transform of the recorded hologram. The main advantages of the method lie in the easy implementation without the need for dedicated instrumentation and in the simple, robust and unambiguous image reconstruction process. In contrast to lens-based microscopy, information on the complex wave field leaving the sample is recorded, i.e., the reconstruction contains both amplitude and phase information. FTH enables a vast amount of empty space around the sample suitable for the realization of various sample environments and in particular the possibility of optical pump-probe experiments. Contrary to lens based imaging methods which are ideally diffraction limited, resolution in soft X-ray FTH is usually set by the lateral extent of the reference pinhole. Most common resolution criteria however, were developed for diffraction limited systems and are not directly applicable to FTH.

One objective of this thesis is to provide a frame work to calculate the resolving power of FTH experiments and to derive suggestions for optimized FTH setups. The drawback of FTH with pinhole references is the low photon efficiency. The interference signal that encodes the object wave field on the detector is typically limited by the number of photons

coherently scattered by the reference structure. Small reference pinholes as desired for high-resolutions therefore adversely affect the efficiency of FTH. Improving the efficiency of FTH by utilizing a novel mask design is another key aspect of this thesis. A third major topic is the exploitation of the holographically recorded phase information in FTH, to extract depth information from three-dimensional specimen.

1.1 Structure

A short review of the FTH imaging method is given subsequently to this introduction in chapter 2. In addition to the generalized FTH imaging theory, this chapter describes how FTH is implemented for soft X-rays.

Theoretical resolution limits of X-ray FTH with pinhole references are investigated and discussed in chapter 3. This chapter contains a closer examination of the X-ray FTH imaging properties and identifies some aspects that fundamentally differ from conventional diffraction limited systems. Two-point resolution limits are developed for reference and diffraction limited soft X-ray FTH systems. This chapter also yields new insights about how to optimize the experimental FTH design and introduces methods that improve the image quality of typical reference-limited holograms. The chapter closes by presenting results of a proof-of-principle resolution test experiment.

In chapter 4, a new method which drastically improves the efficiency of high resolution X-ray Fourier transform holography while retaining the mechanical stability is described. The approach generates an out-of-focus reconstruction which is refocused post-experimentally by numerical wavefield propagation.

The extraction of depth information from a conventional soft X-ray Fourier transform hologram is described in chapter 5. For the experiment, the hologram of an artificial three-dimensional test specimen with dedicated nanometer and micrometer scale features is recorded. Contrary to tomographic approaches, the method relies on just one hologram view and can thus be utilized for single shot experiments. Depth information is extracted from the object by numerically propagating the reconstructed wave fronts emerging from particular object features into focus.

A summary of the results from chapter 3-4 is provided in chapter 6. This chapter also gives an outlook for future FTH experiments.

Sections of this thesis including figures that have been published at peer reviewed journals are marked at the end with the following identifiers:

† J. Geilhufe, B. Pfau, M. Schneider, F. Büttner, C. M. Günther, S. Werner, S. Schaffert, E. Guehrs, S. Frömmel, M. Kläui & S. Eisebitt, *Monolithic Focussed Reference Beam X-ray Holography*, Nat. Comm. **5**, 3008 (2014).

♯ J. Geilhufe, C. Tieg, B. Pfau, C. M. Günther, E. Guehrs, S. Schaffert, & S. Eisebitt, *Extracting depth information of 3-dimensional structures from a single-view X-ray Fourier-transform hologram*, Optics Express **22**, 24959 (2014)

Minor modifications such as changes to the format of text and figures as well as small adaptions of the text such as stylistic improvements or adjustments to the current context may have been performed without further notice.

2 X-ray Fourier transform holography

Holography is a lensless imaging method which was first proposed by Denise Gabor in 1948 [Gab48]. In this context, the term *lensless* refers to the image forming objective lens. Instead of a real space image of the object wave's intensity as delivered by conventional lens based systems, a holographic wavefront reconstruction yields the entire (greek, *holos;* whole) object wave information, i.e., amplitude and phase. The reconstructed object wave can be utilized to retrieve three-dimensional object information or phase contrast images of weakly scattering specimen.

Since image formation for soft X-rays cannot rely on refraction, the prospect of a lensless imaging method is a major motivation to use holographic approaches. For common lens based systems, the objective lens works as a Fourier transformer which accepts the complex wave information scattered by the specimen in the far field. The result is a real space image which is either directly recorded on a detector or serves as an intermediate image for subsequent optics such as an ocular for instance. The quantity recorded by the detector is the light field's intensity. Intensity however represents the squared modulus of the light field and the measurement is incomplete as it lacks the phase information. As long as the object wave is recorded in real space, this circumstance is not very tragic since the intensity image is oftentimes sufficient.

If the intensity of the diffraction pattern is however recorded in reciprocal space, the object's real space image can not be retrieved by a Fourier transform. In order to obtain a real space image of the object, the availability of the phase information in the diffraction pattern is essential. In holography, the diffraction pattern's phase information is exploited in two distinct operations: a recording or detection step, and a reconstruction step. In the first step, the diffracted object wave's intensity pattern is directly recorded in the far field. In order to retain the complete objects wave's complex information, the phase needs to be converted into an intensity variation. Therefore, the object wave is coherently superposed with a well defined reference wave. The phase information is thereby interferometically encoded into the diffraction pattern. If such an inference pattern is recorded on a holographic film, the object wave field can be reconstructed in the second step by re-illuminating the hologram with the reference wave. For holograms that are recorded with electronic detectors such as a charge-coupled device (CCD), the reconstruction is obtained computationally. [Goo96]

Since it was first proposed, holography evolved into numerous techniques with different constraints and capabilities. One technique that is particularly well suited for microscopic X-ray imaging is Fourier transform holography. In the following, basic principles of X-ray Fourier transform holography are reviewed and typical setups are discussed.

2.1 X-ray Fourier transform holography image formation

The lensless Fourier transform holography method applies primary to transparency objects and was first demonstrated by George W. Stroke [Str65] for coherent illumination light in the visible spectrum. The reference beam is provided by a lens which produces a focal spot representing the *point reference* in the object plane. The object and the focusing lens are coherently illuminated by a far away point source. The wave scattered by the object interferes with the reference wave and the diffraction pattern is recorded in the far field (Fig 2.1).

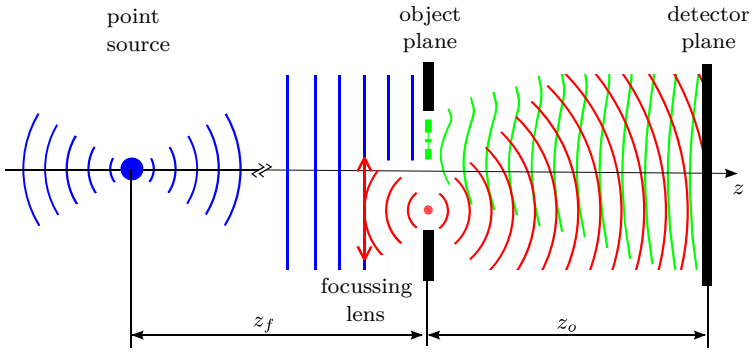

Figure 2.1: Schematic representation of the original Fourier transform holography setup as proposed by G. W. Stroke. The reference wave is focused in the object plane. The interference pattern of object wave and reference wave is recorded in the far field.

In general, Fourier transform holography necessitates a reference structure in the object plane ($\boldsymbol{r} = [x; y]$). In its simplest implementation, this reference structure is a point reference which is separated from the object by $\boldsymbol{r_0} = [x_0; y_0]$. For the transmission functions of an object $o(\boldsymbol{r})$ and a reference pinhole $h(\boldsymbol{r} - \boldsymbol{r_0})$, the hologram which is recorded as the intensity distribution in the far field can be described as follows:

$$\begin{aligned} I_h(\boldsymbol{f_r}) &= |\mathcal{F}[h(\boldsymbol{r} - \boldsymbol{r_0})] + \mathcal{F}[o(\boldsymbol{r})]|^2 \\ &= \mathcal{F}[h(\boldsymbol{r} - \boldsymbol{r_0}) + o(\boldsymbol{r})]\mathcal{F}[h(\boldsymbol{r} - \boldsymbol{r_0}) + o(\boldsymbol{r})]^* \\ &= |H(\boldsymbol{f_r})|^2 + |O(\boldsymbol{f_r})|^2 + O(\boldsymbol{f_r})^* H(\boldsymbol{f_r}) \mathrm{e}^{i(\boldsymbol{f_r} \boldsymbol{r_0})} \\ &\qquad + O(\boldsymbol{f_r}) H(\boldsymbol{f_r})^* \mathrm{e}^{-i(\boldsymbol{f_r} \boldsymbol{r_0})}, \end{aligned} \tag{2.1}$$

where capital letters correspond to the wave fields in reciprocal space and $\boldsymbol{f_r} = [f_x; f_y]$ are the corresponding frequency coordinates. The complex conjugation is indicated by *. The first two terms of Eq. 2.1 are the intensities of the object and the reference waves whereas the last two terms represent the object wave field which is modulated by the reference wave.

If such a interference pattern is recorded on holographic film, the object wavefront can be reconstructed by utilizing a plane wave which is focused by a Fourier transforming lens

after transmission through the hologram [Str65]. For electronically recorded holograms, the Fourier transform is done numerically. The reconstruction of the hologram can be described by:

$$\begin{aligned}\mathcal{F}^{-1}[I_h(\boldsymbol{f_r})] = & \, o(\boldsymbol{r}) \otimes o^*(-\boldsymbol{r}) + h(\boldsymbol{r}) \otimes r^*(-\boldsymbol{r}) \\ & + o(\boldsymbol{r}) \otimes h^*(\boldsymbol{r}+\boldsymbol{r_0}) + o^*(-\boldsymbol{r}) \otimes h(\boldsymbol{r}-\boldsymbol{r_0}),\end{aligned} \tag{2.2}$$

where $\otimes$ indicates the convolution operation. Eq. 2.2 can be simplified by applying shifting theorem and by expressing the convolution of a function with its mirror by the auto-correlation:

$$\begin{aligned}\mathcal{F}^{-1}[I_h(\boldsymbol{f_r})] = & \, o(\boldsymbol{r}) \star o(\boldsymbol{r}) + h(\boldsymbol{r}) \star h(\boldsymbol{r}) \\ & + o(\boldsymbol{r}+\boldsymbol{r_0}) \otimes h(\boldsymbol{r}) + o^*(-\boldsymbol{r}-\boldsymbol{r_0}) \otimes h(\boldsymbol{r}),\end{aligned} \tag{2.3}$$

where $\star$ denotes the correlation operation. The last two conjugated terms of Eq. 2.3 describe the reconstructions as a convolution of the transmission functions of reference and object. For a object diameter d_{obj} and separation distance $|\boldsymbol{r_0}| > 1.5 d_{\mathrm{obj}}$, the two redundant reconstructions are spatially separated from the central auto-correlation in the reconstruction.

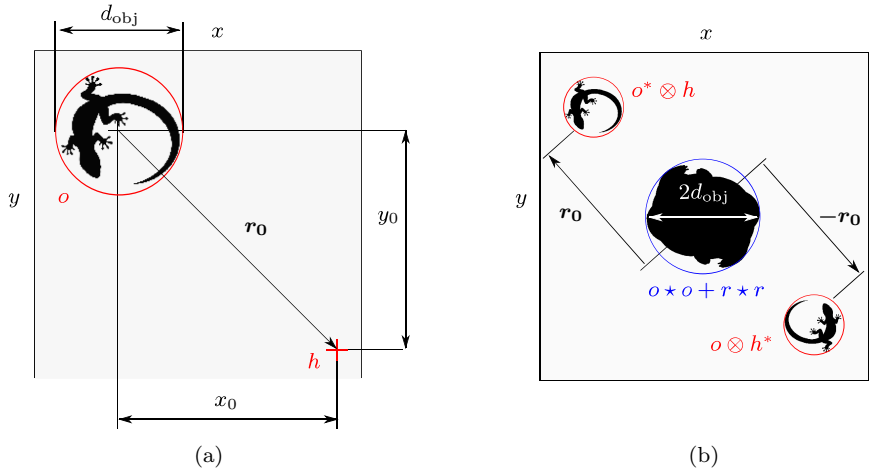

Figure 2.2: Object plane in Fourier transform holography and holographic reconstruction. (a) In order to obtain a focused reconstruction, the reference source (h) is a small spot in the object plane. (b) The reconstruction yields central auto-correlations of object and reference as well as two redundant, conjugated reconstructions. In order to assure that the central auto-correlation does not overlap with the desired reconstructions, the point reference needs to be sufficiently separated from the object

For the experimental layout, the distance z_o defines the system's opening angle $\alpha \approx \mathrm{asin}(d_d/(2z_o))$ in Fourier transform holography, where d_d is the detector diameter. As

further discussed in chapter 3, the opening angle affects the imaging properties in Fourier transform holography. Furthermore, the distance z_o has not only to consider the size of the detector but also the detector's resolution. In this context, the resolution of the detector needs to be sufficient to sample the phase encoding high frequency modulation $p = z_o\lambda/|\boldsymbol{r_o}|$ in the hologram. This frequency is related to $|\boldsymbol{r_o}|$ which represents the largest spatial separation in the mask plane.

The choice of z_f needs to assure that the illumination with a point source of diameter d_s yields approximately plane waves in the object plane. Most importantly, the spatial coherence length $l_{trans} = z_f\lambda/(2\pi d_s)$ [Att07] is required to cover reference optics as well as object.

2.2 Focussed reference X-ray Fourier transform holography

The X-ray implementation of Fourier transform holography was first demonstrated by Ian Mc. Nulty in 1992 [McN92]. The refractive lens that produces the point reference by generating a focal spot in the object plane is replaced by a FZP. One benefit of this configuration is that the object can be illuminated through the FZP. This is possible as diffractive optics share the property that a significant proportion of the incident flux transverses them without changing the propagation direction. The illumination of the object with this undiffracted light (the FZP's zero order) is beneficial as location and size of the focusing FZP is not directly restricted by $|\boldsymbol{r}|$. Apart from this detail, the experimental setup is virtually identical with the setup for visible light as proposed by George W. Stroke.

In the following, design and imaging properties of FZPs are briefly reviewed. Subsequently, characteristics of the X-ray Fourier transform holography setup with FZPs are discussed.

2.2.1 Fresnel zone plate lenses

The FZP is effectively a rotationally symmetric transmission grating with grating periods that decrease for larger radii. For X-ray optics, the FZP usually has a binary profile, i.e., a rectangular profile that ideally shows lines and spaces of equal width. The numerical aperture (NA) of a FZP is set by the outermost zone width Δr:

$$\mathrm{NA} = \frac{\lambda}{2\Delta r}. \tag{2.4}$$

Therefore, the focal spot diameter d_f is directly connected to Δr:

$$d_f = \frac{1.22\lambda}{\mathrm{NA}} = 2.44\Delta r \tag{2.5}$$

For a FZP with focal length f, the radius r_n for the n^{th} zone can be calculated by

$$r_n^2 = n\lambda f + \frac{n^2\lambda^2}{4}. \tag{2.6}$$

The second term of Eq. 2.6 represents spherical aberrations and can be neglected for small NAs with $f \gg n\lambda/2$ [Att07]. Due to the small diffraction angles for high photon energies, X-ray FZPs cannot be fabricated with a Δr that allows for large NA's as known from refractive lenses in the visible spectrum. For this reason, NAs for X-ray FZPs remain relatively small and Eq. 2.6 can be simplified to:

$$r_n = \sqrt{n\lambda f}. \tag{2.7}$$

Focusing light by relying on diffraction causes several implications. Most importantly, the FZP has several diffraction orders. Contrary to refractive lenses that either disperse the light or focus it, a FZP acts like a focusing lens and a dispersing lens simultaneously. This effect is attributed to the negative and positive diffraction orders. Additionally, the FZP has several focal lengths f_1/m originating from the rectangularly shaped zones and the corresponding orders m. For ideal FZPs where subsequent opaque and transparent zones have an equal width, even diffraction orders m cancel at focus. The diffraction efficiency for the remaining m considering an ideal FZP is given by:

$$\eta_m = \frac{1}{m^2\pi^2} \;\; \forall \; m \text{ odd} \qquad \text{and} \qquad \eta_0 = 0.25 \;\; \text{for } m = 0. \tag{2.8}$$

A large fraction of the light incident on the FZP transmits the FZP thus undisturbed while only a factor of $\eta_1 \approx 0.1$ is focused into a particular first order focus. Compared to refractive lenses, FZP are thus much less efficient. The theoretical diffraction efficiency represents the optimum for ideal binary zone plates where the transparent zones do not absorb any light and the opaque zones fully block the beam [Att07].

The diameter of a FZP with a total amount of N zones is given by $D = 4N\Delta r$. The first order focal length dependent on the diameter is $f_1 = D\Delta r/\lambda$. Typical X-ray imaging FZPs with $N = 100$ therefore have diameters of a few µm and hence short focal lengths (contrary to their small NA) [Att07]. For high resolution X-ray imaging, the FZP needs to be placed very close to the specimen. High resolution X-ray imaging with FZPs is thus mechanically challenging.

Another disadvantage is that FZPs are strongly chromatic. FZPs utilized for imaging applications with an illumination light of broad spectral bandwidth yields thus a poor image quality. For such applications, the illumination light needs to be monochromatized. For Fourier transform holography with coherent illumination light of narrow spectral bandwidth, chromatic aberrations are however irrelevant [Att07].

2.2.2 Focussed reference X-ray Fourier transform holography setup

By producing a strongly focused point reference in the object plane, the object wave is amplified as the reconstructed contribution of the diffraction pattern is the modulation of reference and object wave (Eq. 2.1). In real space, this amplification turns out as the convolution of the object transmission function with a spot that is much more intense than the object (Eq. 2.3).

Since the resolution in Fourier transform holography is defined by the size of the point reference, the reference wave needs to be focused by a FZP with small Δr. Due to the corresponding small focal length, the FZP needs to be positioned in close proximity to the object. The separation of reference source and object potentially causes relative drift and vibration between both elements. The spatial resolution might thus be degraded by motion blur. Stability of the setup is thus of considerable importance [McN92]. Additionally, modern X-ray sources such as FELs and high harmonic generation (HHG) sources that deliver fs pulses, typically feature a very low pointing stability. This leads to focal spot locations that vary from shot to shot. For exposures over many shots, the moving reference leads to resolution degradation similar to motion blur [Mal13].

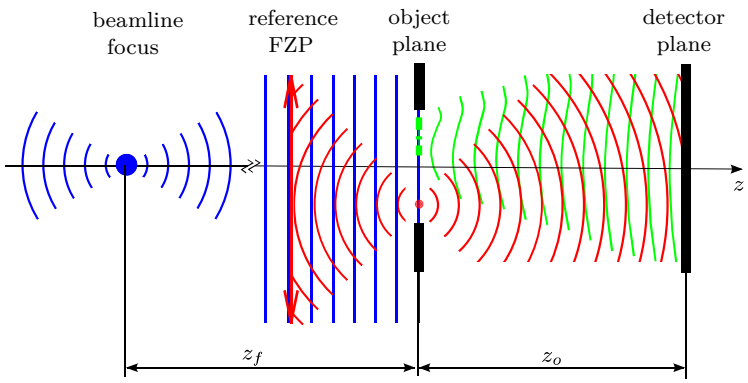

Figure 2.3: Schematic representation of a Fourier transform holography experiment. The mask is coherently illuminated monochromatic light. A reference wave originates from a small pinhole fabricated into the mask. The interference pattern of object and reference wave is recorded in the far field.

2.3 Monolithic reference X-ray Fourier transform holography

The image quality of X-ray Fourier transform holography was much improved by utilizing an approach that monolithically couples the reference source to the object. The object is placed in an aperture that is produced into a X-ray opaque metal film and defines the field of view. Instead from a FZP focal spot, the point reference originates from a small pinhole that is generated adjacent to the object. This *integrated mask* design which was first proposed by Stefan Eisebitt in 2004 [Eis04] has triggered an avalanche of X-ray

holography experiments, in particular with applications in the field of nanomagnetism [Büt13; Gün10; Pfa11; Sti11; Wan12] and bio-imaging [Gue09; Gue10; Gue12; Mar08]. In the following, the abbreviation FTH specifically refers to this integrated mask soft X-ray implementation of Fourier transform holography.

Due to the fixed relation between the reference wave source and the object, the method is inherently insensitive against drift, vibration and pointing instabilities of the source. In addition, the integrated mask design enables a vast amount of empty space around the sample for the realization of various sample environments, in particular the possibility of pump-probe experiments.

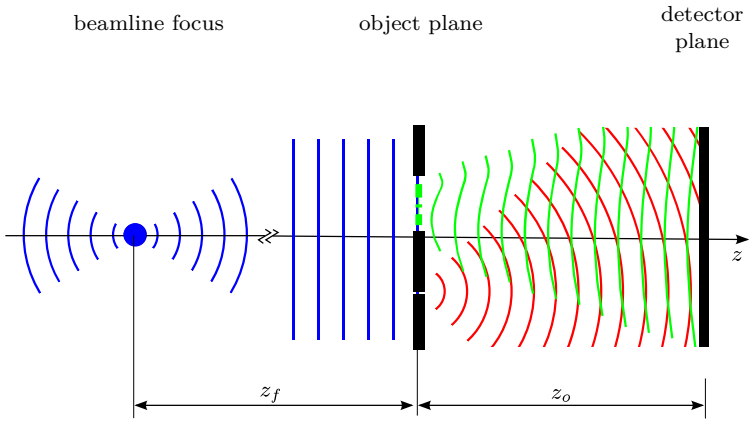

Figure 2.4: Schematic representation of a FTH experiment with an integrated mask. The mask is coherently illuminated with X-rays. A reference wave originates from a small pinhole fabricated into the mask. The interference pattern of object and reference wave is recorded in the far field.

The drawback of point-like apertures generating reference waves is the entanglement of spatial resolution and contrast in the reconstruction. If the reference diameter is decreased, the resolution limit will scale linearly with the reference size while the reference signal strength, and ultimately the image contrast, is reduced quadratically. A high-resolution FTH imaging experiment is therefore commonly designed as a compromise between the desired resolution and the required reference signal. As long as the reference signal exceeds the detector's noise level, the decrease in flux through an ever smaller reference could in principle be accounted for by extending exposure times up to a certain practical limit. However, resolution limits as reported for Fresnel zone plate (FZP)-based X-ray microscopy [Cha12] have not been achieved for FTH using reference pinholes with high aspect ratio up to now.†

The maximum diffraction angle recorded by the detector is determined by the detector size and the distance of the detector from the holographic mask, i.e., the distance z_o. Due to the trade off between flux and spatial resolution, a reasonable choice of the FTH system's opening angle considers the diameter of the reference pinhole. A reasonable

configuration of the FTH system's parameters for optimal resolution is discussed in chapter 3.

2.4 Numeric wave field propagation

Due to the *Hygens-Fresnel principle*, the knowledge of the object's wave complex amplitude in a certain reconstruction plane allows to anticipate how the wave is advancing along the optical axis. In FTH, it is therefore possible to obtain a focused reconstruction by utilizing a point reference that is not located in the object plane. From the physics perspective, the hologram can be thought to represent the object's transmission function that is decomposed into amplitude and phase of elementary plane waves. Dependent on their scattering angle, all plane waves are mapped to points in the hologram, i.e., on the recording medium in the far field. Upon reconstruction, the plane waves are recomposed in proper phase relation. An elementary plane wave can be described by:

$$\psi(x, y, z) = e^{i(k_x x + k_y y + k_z z)}, \tag{2.9}$$

where $\boldsymbol{k} = [k_x; k_y; k_z]$ is the wave-vector [Pag06]. For our discussion, let z be the optical axis while the xy plane is the initial reconstruction plane containing the reference point. With $k_z = \sqrt{|\boldsymbol{k}|^2 - k_x^2 - k_y^2}$, Eq. 2.9 can be written as:

$$\psi(x, y) = e^{i(k_x x + k_y y)} e^{izk_z} = e^{i(k_x x + k_y y)} e^{iz\sqrt{|\boldsymbol{k}|^2 - k_x^2 - k_y^2}}. \tag{2.10}$$

The first factor of Eq. (2.10) describes the plane wave recorded on the hologram for $z = 0$. The second factor is called *free-space propagator* [Pag06]. In order to calculate the particular, elementary wave front at any distance z from the reference plane, the corresponding point in the hologram needs to be multiplied by this phase factor. In order to retrieve the whole reconstruction after propagation to z, the free space propagator can be applied point by point to the entire hologram. The object wave field at distance z is obtained by recomposing all elementary waves with their new phase factor by Fourier transforming the modified hologram. In the real space, the object wave front reconstruction retrieved by such a calculation, however, assumes that the propagated distance is free of disturbances. Strongly absorbing features within the propagation distance or a propagation through a medium with real valued, inhomogeneous refractive index, will lead to deviations from the predictions via free space propagation. An error evaluation for applications in the water-window is provided in chapter 5.1.1.

3 Spatial resolution in X-ray Fourier transform holography

The spatial resolution of an imaging system is one of the most important performance figures when determining whether or not the system is appropriate to investigate a certain specimen of interest. Generally, the resolving power of imaging systems is fundamentally limited by a lower boundary. This phenomenon was first described by Ernst Abbe in 1873. Abbe investigated the resolution limit of a full field optical microscope by imaging line gratings under coherent illumination with monochromatic light of wavelength λ. In order to resolve a line grating with spatial period p, which is illuminated by a far away point source located on the optical axis (*central illumination* or *collinear illumination*), the microscope's entrance pupil needs to be sufficiently large to collect not only the gratings zero diffraction order but also at least the grating's first orders [Abb73].

The first diffraction orders appear at an angle $\alpha = \arcsin(\lambda/p)$ to the optical axis and a grating enclosed in a medium of refractive index n can be resolved for microscopes with numerical apertures $\mathrm{NA} > \lambda/p$. Here, the numerical aperture is defined as $\mathrm{NA} = n\sin\alpha$. For a given opening angle, the microscopes resolving power can be improved if the illumination light contains rays that do not originate from the optical axis *(oblique illumnination)*. For such off-axis rays, the image formation relies on the collection of just one of the first diffraction orders besides the central zero order. In practice, such an off-axis illumination is achieved by using a condenser lens to illuminate the specimen. For aberration free microscopes and a condenser lens with a numerical aperture equal or larger than the numerical aperture of the objective lens, the ideal resolution limit is thus doubled compared to the central illumination type. The smallest feature size (d_{ang}) that ideally can be resolved by a diffraction limited imaging system ,i.e., the *angular resolution limit*, is therefore determined by [Abb73]:

$$d_{\mathrm{ang}} = \frac{\lambda}{2n\,\sin(\alpha)} = \frac{\lambda}{2\mathrm{NA}}. \tag{3.1}$$

Nearly perfect imaging systems that fulfill relation (3.1) are said to be *diffraction limited*. Only in special cases it is possible to accomplish a resolution beyond the diffraction limit. Approaches to break the diffraction barrier include methods based on non-uniform illumination types [Gus05; Hel94; Sch03] or near field detection of the specimen diffraction pattern [Amb56].

Lens based systems that do not reach the diffraction limit are usually regarded as deviations from the theoretical ideal with degraded resolution caused by imaging aberrations.

The most common criteria for resolution limits were developed for diffraction limited imaging systems with circular entrance pupils, due to the overwhelming abundance of such systems. In the case of X-ray FTH however, the resolution is often limited by the reference pinhole and not by the system's opening angle [Eis04]. One purpose of this chapter is to discuss the applicability of the resolution theory of conventional diffraction limited lens-based systems for FTH. Therefore, the image formation of diffraction limited systems is briefly reviewed. Subsequently, important aspects are adapted to the FTH system and the effects of the reference limitation on the image quality are discussed. From the insights of this discussion, theoretical FTH resolution limits are defined and suggestions for optimized FTH experiments with pinhole references are derived.

3.1 Image formation for diffraction limited systems

The resolving capabilities of diffraction limited imaging systems depend on the question of how the information on the object's spatial frequencies are processed and transferred into the image. The modification of the input spatial frequencies induced by an imaging system can conveniently be modeled by the linear systems formalism as described in Ref. [Goo96] and as briefly summarized here. This formalism is later used to develop a description of the image formation in FTH (Chap. 3.4).

In the following, a generalized imaging system is briefly reviewed and the terminology necessary for the system's characterization in the Fourier formalism is introduced. For instance, a single magnifying lens is a good representative for a simple imaging system. The maximum diffraction angle accepted by such a system is defined by the lens's numerical aperture. The system thus accepts diffraction angles up to the corresponding NA by an amplitude transmission that is non-zero. Depending on the lens properties, incident waves with diffraction angles accepted by the system might be transferred into the image with amplitude and/or phase distortions.

The complex valued *pupil function* P describes how the lens affects amplitude and phase of the incoming wave dependent on the position in the entrance pupil. The pupil function P can thus be evaluated by probing the lens point-by-point with the corresponding diffraction angles or equivalently, by the associated spatial periods in the object plane. Due to the system's property of linearity, such an evaluation can be done more conveniently by utilizing a point-like input signal with a wide and uniform spatial frequency spectrum. In Fourier theory, such an *impulse signal* is represented by the Dirac delta function (δ). The Fourier transform of a δ-like object is constant and the system's response to that input is called point-spread function (PSF).

An unknown linear and space-invariant imaging system $\mathcal{S}$ can thoroughly be characterized by utilizing a δ-pulse as input and by analyzing the impulse response, i.e., the system's PSF. In this context, the unknown system can be understood as a black box. The response of a system to an arbitrary input is then expressed in terms of the responses to elementary functions into which the input can be decomposed. Depending on the

illumination conditions – coherent or incoherent – the system's linear quantity is either the electric field amplitude (U) or the intensity (I) of the output signal. The linear system is called *space-invariant*, if the response to a point-like input signal does not change in shape but only in location as the input signal moves within the object field.

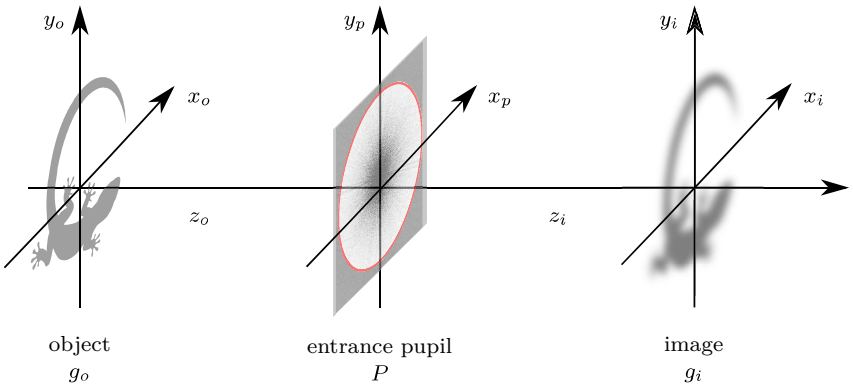

Figure 3.1: Generalized imaging system illuminated from the left side. The object g_o is given by the transmission function in the object plane. The system accepts only the fraction of the objects diffraction pattern that lies within the system's finite entrance pupil P. The frequency distribution of the image g_i is thus low pass filtered, i.e., the image is blurred

With the notations given in Fig. 3.1, the response (g_i) of a linear and space-invariant imaging system in the image plane to an arbitrary input g_o is filtered by the system's P in the system's entrance pupil. If g_o is a unit impulse δ located at $x_\mathrm{o} = x'_\mathrm{o}, y_\mathrm{o} = y'_\mathrm{o}$ in the object plane, the image g_i produced by $\mathcal{S}$ defines the system's impulse response h:

$$h(x_\mathrm{i} - x'_\mathrm{o}, y_\mathrm{i} - y'_\mathrm{o}) = \mathcal{S}\{\delta(x_\mathrm{o} - x'_\mathrm{o}, y_\mathrm{o} - y'_\mathrm{o})\}. \tag{3.2}$$

The image $g_\mathrm{i}(x_\mathrm{i}, y_\mathrm{i})$ of more complex objects produced by a space-invariant linear system is the convolution of the image predicted by geometrical optics, $g_\mathrm{o}(x'_\mathrm{o}, y'_\mathrm{o})$ with the elementary function h:

$$g_i(x_\mathrm{i}, y_\mathrm{i}) = \iint_{-\infty}^{+\infty} g_o(x'_o, y'_o) h(x_i - x'_o, y_i - y'_o)\, \mathrm{d}x'_o \mathrm{d}y'_o = h \otimes g_o \tag{3.3}$$

For diffraction limited systems, the PSF represents therefore a low-pass filtered point signal and h is therefore entirely described by the shape of the low-pass filter P. Both h and P define the imaging system equivalently and can be converted into each other. Instead of P which is a function of the location in the entrance pupil, it is more convenient to express the transmission of amplitude and phase in terms of the object's spatial frequencies f_x and f_y. The resulting function is known as the system's *transfer function*. The relation between h, P and the system's transfer function depends thereby on the spatial coherence

of the illumination light.

3.1.1 Coherent illumination

Under coherent illumination, the diffraction limited system is linear in amplitude and the transfer function is also called *amplitude transfer function* (H). All primary waves that are originating from a coherent light source have a fixed phase relation which results in a combined superpositioned secondary plane wavefront. Also the waves that illuminate the imaging system's entrance pupil after diffraction by the object, are well defined and constant over time. For a δ-like object on the optical axis, the far field distribution within the imaging system's entrance pupil under coherent illumination is thus the Fourier transform of the (centered) δ-function, i.e., a plane wave with constant phase. Therefore, H resembles the pupil function P with a constant field within the entrance pupil and zero field outside. Due to the plane-wave illumination, also extended objects result in time-constant wave fronts incident to the system's entrance pupil in the far field. The image intensity I_i for coherent illumination is given by the squared modulus of the convolution of the amplitude image predicted by geometric optics U_g with h:

$$I_\mathrm{i} = |h \otimes U_\mathrm{g}|^2. \tag{3.4}$$

The amplitude transfer function H can be expressed as the Fourier transform of the system's impulse response h:

$$H(f_x, f_y) = \mathcal{F}[h(x_\mathrm{i}, y_\mathrm{i})] = \frac{A}{\lambda z_\mathrm{i}} P(\lambda z_\mathrm{i} f_x, \lambda z_\mathrm{i} f_y), \tag{3.5}$$

where f_y and f_x are the spatial frequencies in the object plane and A is a constant amplitude. By applying the autocorrelation theorem and denoting the autocorrelation by $\star$, the impact of H on the image intensity frequency spectrum can be expressed by:

$$\mathcal{F}\{I_\mathrm{i}\} = HG_\mathrm{g} \star HG_\mathrm{g}, \tag{3.6}$$

where G_g represents the spatial frequency spectrum of the object's transmission function. To conclude, for coherent illumination, the input frequency spectrum G_g is affected by a point-by-point multiplication with H in the frequency domain. For an aberration free and diffraction limited imaging system, the frequency components within the system's passband are not distorted, neither in phase nor in amplitude (see also Fig. 3.2).

3.1.2 Incoherent illumination

The incoherently illuminated system is linear in intensity and the image is given by:

$$I_\mathrm{i} = |h|^2 \otimes |U_\mathrm{g}|^2. \tag{3.7}$$

While the coherent H is a scaled image of P, the incoherent transfer function ($\mathcal{H}$) is given by the scaled autocorrelation of P:

$$\begin{aligned}\mathcal{F}[|h(x_i, y_i)|^2] &= P(\lambda z_\mathrm{i} f_x, \lambda z_\mathrm{i} f_y) \star P(\lambda z_\mathrm{i} f_x, \lambda z_\mathrm{i} f_y) \\ &= H(f_x, f_y) \star H(f_x, f_y) = \mathcal{H}(f_x, f_y). \end{aligned} \tag{3.8}$$

Compared to the coherent H, the incoherent transfer function $\mathcal{H}$ has thus a doubled cut-off frequency (see Fig. 3.2(b)). $\mathcal{H}$ is also called *optical transfer function*.

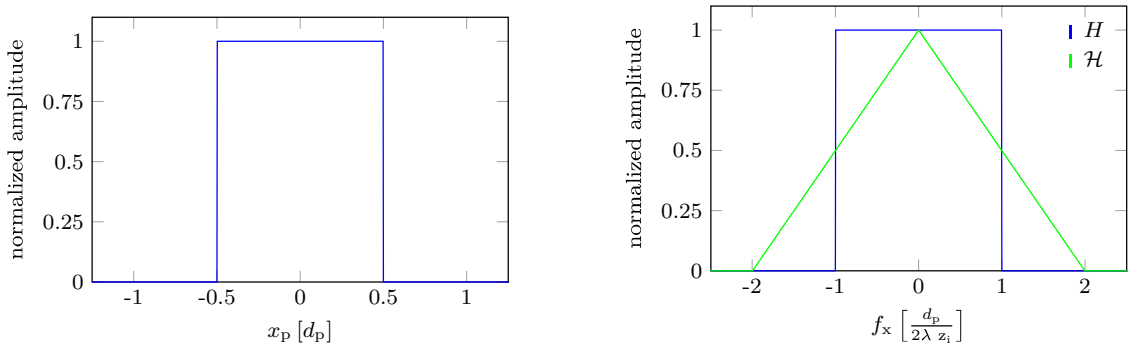

Figure 3.2: (a) Profile of the pupil function P in units of the entrance pupil diameter d_p for a diffraction limited imaging system (b) The coherent amplitude transfer function H and the incoherent optical transfer function $\mathcal{H}$ for the pupil function shown in panel (a). The coherent H represents a scaled image of the pupil function P whereas the incoherent $\mathcal{H}$ is the scaled autocorrelation of P.

An intuitive explanation from the physics perspective for Eq. (3.8) can be derived from the insight that under incoherent illumination, there is no fixed phase relation between the primary waves approaching the object. The superposition of these waves results in a combined secondary wavefront that is not planar and changes rapidly over time. For a single δ-like object on the optical axis, the result is still similar to the coherent illumination type as the impulse response h is independent on the illumination's degree of spatial coherence (a single δ-like point source in the object plane will always illuminate the entrance pupil in the far field spatially coherently). Contrary to coherent illumination however, the waves that approach the system's entrance pupil after diffraction by an extended object under incoherent illumination have time-varying wave vectors. Since the wave vector corresponds to the propagation direction of the wave front, the entrance pupil appears to be illuminated from directions that statistically vary over time. The extension of the frequency passband due to a low degree of coherence can thus be seen as analogous to off-axis illumination where the spatial frequency cut-off is also twice as large compared to the on-axis illumination type.

In frequency space, the image formation can be described by:

$$\mathcal{F}\{I_\mathrm{i}\} = [H \star H][G_\mathrm{g} \star G_\mathrm{g}] = \mathcal{H}[G_\mathrm{g} \star G_\mathrm{g}]. \tag{3.9}$$

Even though the frequency cut-off of $\mathcal{H}$ is doubled compared to the coherently illuminated system's H, it can be shown that the resolution limit is not generally superior compared to the coherent illumination type [Goo96]. The modulus of $\mathcal{H}$ is the system's *modulation transfer function* (MTF) while the phase is called *phase transfer function* (PhTF). The MTF is usually of greater interest compared to the PhTF when characterizing an imaging system. The MTF describes how the contrast of a thoroughly modulated periodic signal with a certain frequency in the object plane is affected by the imaging system. Spatial shifts of this input signal in the image are determined by PhTF. The image contrast depends on the extremal values of the image intensity I_i:

$$C = \frac{\max(I_\mathrm{i}) - \min(I_\mathrm{i})}{\max(I_\mathrm{i}) + \min(I_\mathrm{i})}. \tag{3.10}$$

Descriptions of *contrast* or *image contrast* throughout this thesis refer to Eq (3.10).

The normalized intensity of h in the image plane depending on the radius $\boldsymbol{r_i} = (x_i; y_i)$ from the central maximum for a circular pupil function of diameter d_p is given by:

$$I_i(r_i) = \left[\frac{2J_1(kd_p r_i/2z_\mathrm{i})}{kd_p r_i/2z_\mathrm{i}}\right]^2, \tag{3.11}$$

where, J_1 is the Bessel function of the first kind, grade one and $k = 2\pi/\lambda$ is the wave number. The intensity distribution described by Eq. (3.11) is also called *Airy pattern*. The inner part of the Airy pattern within the radius of the first minimum at $r_\mathrm{min} = 1.22\lambda/d_p$ is often referred to as the *central Airy disk*.

The diffraction limited FTH system's entrance pupil is usually a charge-coupled device (CCD) detector of rectangular – most commonly square – shape. The impulse response h of a such shaped entrance pupil is a two-dimensional sinc function (see Eq. (3.22)). Fig. 3.3 shows the impulse response of a circular and a rectangular entrance pupil. Compared to the Airy pattern of a circular entrance pupil with diameter d_p, the intensity profile of the square-shaped aperture with a side length of $s_\mathrm{ccd} = d_p$ is more confined in its central region and shows more pronounced side-lobes. Apart from the shape of the pupil function of the typical FTH setup, another notable difference to most common imaging systems is that the reconstructed quantity is not the transmission intensity but the complex amplitude of the wave field at the exit of the object. As further discussed in chapter 3.4, both properties affect the theoretical resolution limit for the diffraction limited FTH setup.

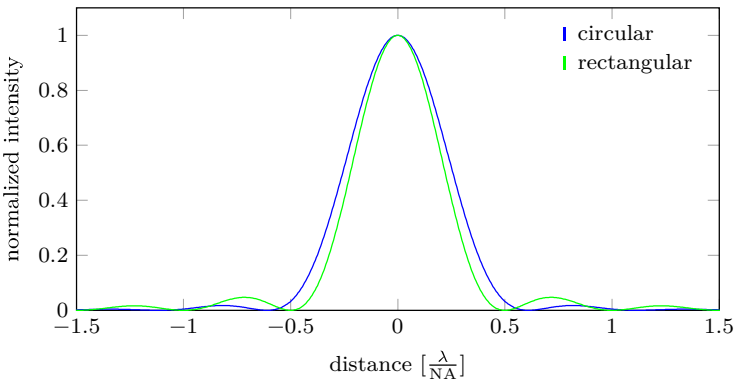

Figure 3.3: Normalized impulse response (intensity) of a diffraction limited system with a circular and a rectangular entrance pupil. The plot shows the profile through the center of the PSF in the image plane. For the circular pupil function, the intensity profile of the PSF describes an Airy-pattern, which shows the first minimum at $r_i = 0.61\lambda/\mathrm{NA}$. The PSF for a rectangular entrance pupil is a two-dimensional sinc pattern with first minima at $x_i = \pm 0.5\lambda/\mathrm{NA}$ or $y_i = \pm 0.5\lambda/\mathrm{NA}$

3.2 The Rayleigh criterion

The Rayleigh criterion describes the minimal distance between two incoherent point sources that allows to just resolve these two points when imaged by a diffraction limited imaging system with circular aperture. For systems described in the linear system's formalism, the two incoherent points are represented by δ-distributions and the point-spread function h is an Airy disk. If the distance between the two δ-peaks is gradually reduced, the system will eventually fail to reproduce the point-sources distinctly in the image. The Rayleigh criterion states that the imaged points are barely resolved when the maximum of one Airy disk coincides with the first minimum of the other Airy disk. The distance between both points – commonly referred to as the *Rayleigh-distance* – is hence the radius of the central Airy disk, i.e., $0.61\lambda/\mathrm{NA}$. In the superposed intensity image, an intensity reduction of 27% of the maximum value separates the images of the two points and makes them distinguishable. Instead of imaged intensity, the rayleigh resolution can also be expressed in terms of contrast. The image contrast for two point sources separated by one Rayleigh distance is 15.3% [Goo96].

For imaging applications like microscopy, the usability of δ-like test objects with various spacings has practical implications since such features deliver weak signals and are difficult to manufacture. In microscopy the Rayleigh criterion is thus oftentimes adapted to different test objects like line gratings, sector stars or sharp edges. Fig. 3.4 shows the convolution of an Airy profile with different input functions. The results suggest that a strict interpretation of the Rayleigh criterion actually forbids its direct application to the most common class of test objects, namely periodic structures, especially those with equally wide lines and spaces (Fig. 3.4(c)). For such test patterns, the 15.3% image

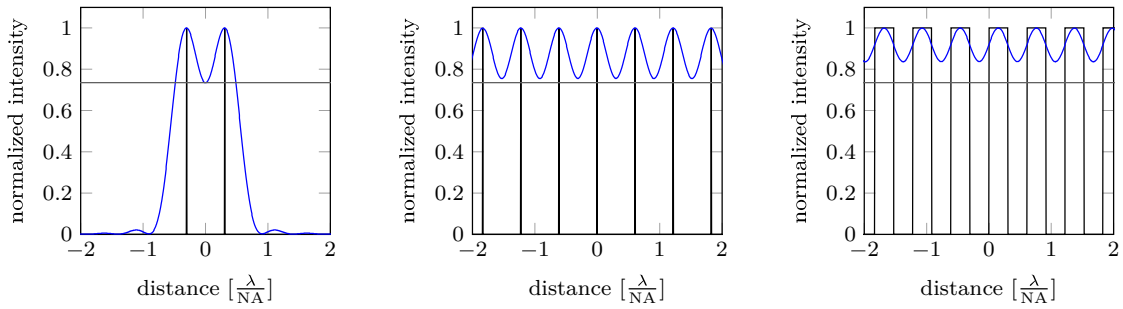

Figure 3.4: Rayleigh criterion as applied for two points and periodic test structures. These plots show the profile of the diffraction limited system response. The geometric input is convolved with an Airy disk. Input functions are: (a) two δ-peaks, (b) a Dirac-comb and (c) a line grating with equally wide lines and spaces. The distance between the δ-peaks as well as the period of the Dirac-comb and the line grating corresponds to $0.61\lambda/\mathrm{NA}$

contrast criterion may be applied to determine the resolution cut-off by analyzing the contrast of the imaged gratings for different grating-periods. However, the period that corresponds to the resolution limit found by such a measurement exceeds the (two-point resolution) Rayleigh distance of $0.61\lambda/\mathrm{NA}$ (Fig. 3.4(a)). For gratings with much wider lines than spaces ,i.e., gratings that resemble a Dirac comb, the difference in contrast is marginal compared to the image of two points (Fig. 3.4(b)). If applied to periodic patterns, the Rayleigh distance corresponds to a full spatial period [Att07]. Another type of convenient resolution test structures are knife-edge patterns. The intensity transition of the imaged edge over the distance $0.61\lambda/\mathrm{NA}$ is approximately 10% to 90% [Hec98].

Since the Rayleigh criterion is strictly defined for incoherently illuminated objects, the degree of coherence of the illumination needs to be sufficiently small for its direct application. For coherent illumination, the actual two-point resolution limit depends strongly on the phase between both points [Goo96]. Fig. 3.5 shows the profile of two imaged point-sources spaced by one Rayleigh distance [Tho69]. In panel (a), the two point sources have fixed phase relations, i.e., the illumination is coherent. The image intensity between both points for coherent illumination depends on the points phase difference. For a relative phase of $\theta = 0$ the intensity midway between both points shows a global maximum, resulting in a contrast of 0%. For $\theta = \pi$ the normalized intensity profile between both points shows a minimum with zero intensity and the image contrast reaches thus 100%. For $\theta = \pi/2$ the normalized intensity profile shows a local minimum between both points. Similarly to incoherent illumination, the intensity at this local minimum is reduced by 27% and the image contrast is 15.3%. Fig. 3.5(b) shows two point-sources spaced by one Rayleigh distance with similar phase for different degrees of coherence (γ). For $\gamma > 0$, the local minimum of the normalized intensity profile vanishes and transforms into a global maximum for $\gamma > 0.5$

Also for imaging applications with coherent object illumination and a uniform phase across the image, the resolution limit can be determined similar to the Rayleigh criterion by defining the contrast cut-off for closely spaced points to 15.3%. In this case, the maximum of one Airy disk does not coincide with the minimum of its counterpart and the corresponding distance between the two barely resolved point sources in the intensity image yields $0.82\lambda/\mathrm{NA}$ [Bor99]

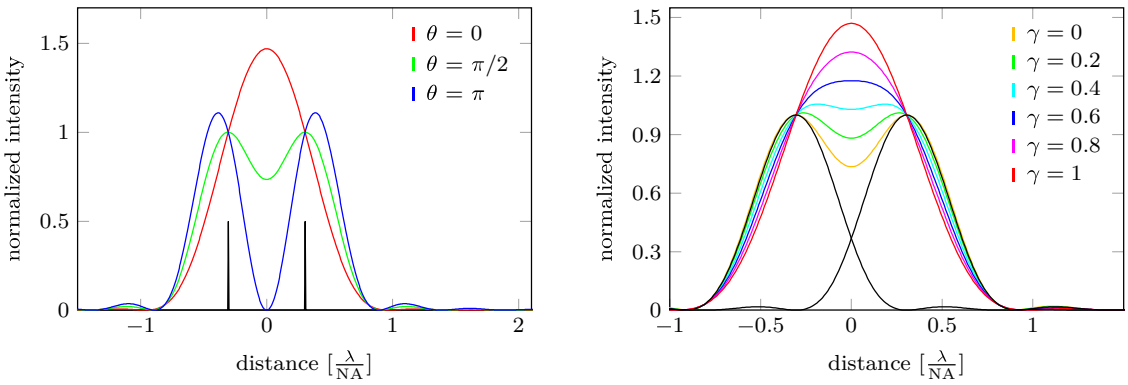

Figure 3.5: Rayleigh criterion applied to fully coherent and partly coherent point-sources. (a) Two coherently superposed Airy disks spaced by one Rayleigh distance for different relative phases. The vertical lines represent the positions of the point-sources. Only for a phase difference of $\theta = \pi/2$, the contrast between the two Airy patterns equals 15.3% while for $\theta = \pi$ the contrast is unity and in case of a similar phase both points can not be resolved, i.e., the contrast is zero. (b) Two Airy disks of similar phase separated by one Rayleigh distance, superposed with different degrees of coherence.

3.3 Sparrow criterion

The Sparrow-criterion defines the smallest resolvable separation between two closely spaced and just resolved point-sources as the distance, at which the second derivative of the resultant image intensity vanishes midway between the connection of both points. The intensity profile yields thus a plateau with maximum intensity between the two points. The Sparrow criterion has been extensively used to characterize imaging systems with partially coherent illumination. The Sparrow resolution limits for incoherent and coherent illumination are $0.47\lambda/\mathrm{NA}$ and $0.73\lambda/\mathrm{NA}$ respectively [Tho69].

Fig. 3.6 shows the Sparrow criterion for two closely spaced points for incoherent and coherent illumination. The separation (s) between both points is expressed in units [λ/NA]. Panel (a) shows the normalized intensity profile of both points for incoherent illumination. For small separations between the two point-sources, the maxima of the intensity profile deviate the more from the corresponding δ-peak positions (colored circles)

the closer the Sparrow resolution limit is approached. The mismatch of the actual separation of the two points relative to the separation of the intensity maxima is shown in panel (b). For separations larger than the Rayleigh distance ($s = 0.61\lambda/\mathrm{NA}$), the intensity maxima approximate the positions of the points. Fig. 3.5(c) and (d) show similar graphs for coherent illumination. Here, the positions of the intensity maxima match the positions of the points for the adapted Rayleigh distance of $s = 0.82\lambda/\mathrm{NA}$. Compared to incoherent illumination, the position of the intensity maxima for separations $s > 0.82\lambda/\mathrm{NA}$ deviates more strongly from the actual point positions [Tho69]. Imaging small features with coherently illuminated diffraction limited imaging systems, can therefore lead to misinterpretations.

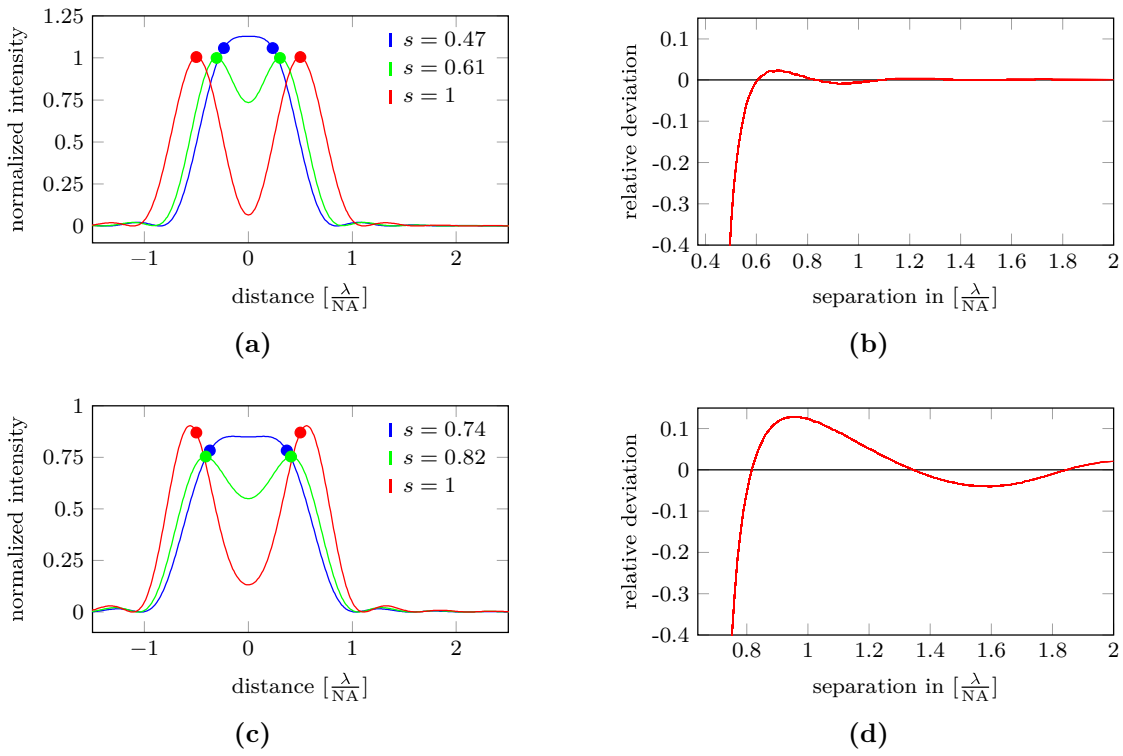

Figure 3.6: Illustration of the Sparrow criterion for spatial resolution. (a) Profile of two incoherently superposed Airy disks with spacings approaching the Sparrow-limit. The positions of the centers of the individual Airy disks are indicated with colored circles. (b) Deviation of the separation between the two maxima of an incoherently superposed intensity profile similar to (a) relative to the distance between both Airy disks. Panels (c) and (d) show similar curves for coherently superposed Airy disks. For small separations around the resolution limit, the separation of the maxima in the image does not match the separation between both Airy disks. For coherent illumination, the mismatch is more significant compared to incoherent illumination.

3.4 Resolution as applied to X-ray Fourier transform holography

For the definition of common resolution criteria as reviewed above, it was possible to rely on an Airy shape of the PSF. However, such a PSF is typical for a certain class of imaging systems, i.e., diffraction limited, space-invariant imaging systems that produce intensity images and have with a circular entrance pupil. In FTH, the form of the PSF differs from the shape of an Airy-pattern for several reasons. Firstly, the reconstructed quantity upon Fourier transforming the hologram is usually not the intensity but rather the complex amplitude of the wave-field within the field of view in the object plane. Secondly, the resolution is typically not diffraction limited and thirdly, the pupil function P in FTH cannot be described by a circular disk that transmits all spatial frequencies without distorting amplitude or phase. For these reasons, FTH can not rely on common two-point resolution criteria such as the Rayleigh criterion or the Sparrow limit. This also applies to *knife-edge* resolution tests that relate the intensity transition of an imaged edge to two point resolution limits like the Rayleigh criterion [Hec98]. For instance, the transition of the signal over an imaged edge from 10% to 90% in an FTH reconstruction does not correspond to any common two-point resolution limit.

For the layout of FTH imaging experiments, it is desirable to precisely predict the diffraction limited resolution cut-off in order to determine the reference pinhole diameter that ensures imaging with maximum photon efficiency without loss of resolution. For a definition of an FTH resolution limit, the form of the PSF and the corresponding transfer function needs to be evaluated. In order to review FTH using the notations of Fig. 3.1, the distance z_i from the entrance pupil (i.e., the detector surface) to the image plane needs to be defined. While this quantity has no practical meaning in an FTH experiment, in the generalized model z_i relates the FTH system's magnified reconstruction to the image plane.

In the following, the detector is assumed to be aligned to the coordinate system in the pupil plane as shown in Fig 3.1, i.e., the edges of the detector are aligned in direction x_p and y_p. In FTH, the magnification is given by $p_\mathrm{ccd}/p_\mathrm{o}$, where p_ccd is the pixel size of the detector, $p_\mathrm{o} = z_\mathrm{o}\lambda/s_\mathrm{ccd}$ is the pixel size in the reconstruction, corresponding to the imaged object and s_ccd is the CCD's side length. The magnification in the generalized model is $M = z_\mathrm{i}/z_\mathrm{o}$ [Hec02] and the distance z_i is thus given by:

$$z_\mathrm{i} = Mz_\mathrm{o} = \frac{p_\mathrm{ccd}}{p_\mathrm{o}} z_\mathrm{o} = \frac{p_\mathrm{ccd} s_\mathrm{ccd}}{\lambda}. \tag{3.12}$$

For a generalized discussion of the FTH system, an expression for the FTH system's pupil function P_fth needs to be derived. A theoretical model of P_fth allows to derive expressions for the FTH system's transfer function (H_fth) and the point-spread function h_fth. Similar to the diffraction limited P, P_fth is a complex function of the location (x_p,y_p) in the entrance pupil which describes how amplitude and phase of an incoming wave is affected by the FTH system. Instead of the Fourier transforming lens of a diffraction-limited, lens based imaging system, the entrance pupil of the FTH system is the surface of the

hologram recording detector. For the coherent diffraction limited system, P is defined as the normalized, complex amplitude of a plane wave within the entrance pupil. As the plane wave originates from a δ-object on the optical axis, the phase of the plane wave is zero and P is real valued. Since P is constant over the entrance pupil, all spatial frequencies within the coherent, diffraction limited system's passband are transmitted with the same amplitude, i.e., the contrast of features within the system's passband is independent from the spatial frequency. The contrast in the FTH reconstruction however is determined by the interference of the reference beam with the object wave within the detector area. Depending on the reference size relative to the FTH system's NA, higher frequencies are more or less suppressed by the reference pinhole of an FTH system. For this reason, also the source of the phase encoding reference beam acts as a low-pass filter (besides the finite detector area). In order to discuss the resolving power of the FTH system, the impact of the reference pinhole on P_{fth} needs thus to be considered. For the following discussion, the reference pinhole in the object plane is assumed to be centered on the optical axis. According to this convention and due to the required separation between object and reference ($\boldsymbol{r_0}$, see Fig.2.2) the location of the object is then off-axis.

Corresponding to detector and reference pinhole, P_{fth} has two contributions. The first contribution is the *detector pupil function* P_{ccd}. Similarly to the description of P for the diffraction limited system in the Fourier formalism, P_{ccd} can be understood as the normalized, complex amplitude of a δ-object's diffraction pattern within the system's entrance pupil in the far field, i.e., the contribution of a plane wave that covers the detector. P_{ccd} is thus a complex function of the location in the detector plane and has an amplitude which is constant over the detector area and zero outside. Due to the off-axis layout of the FTH mask however, the δ-object is not centered on the optical axis and the resulting P_{ccd} has no constant phase of zero but rather a phase ramp. The second contribution is represented by the *reference pinhole pupil function* on the detector P_{ref}. Considering a perfectly circular symmetric disk as reference pinhole (and the above convention that the reference pinhole is centered on the optical axis), P_{ref} is a real valued function, representing the far-field amplitude pattern of the reference pinhole:

$$P_{\mathrm{ref}}(\boldsymbol{r}_{\mathrm{p}}) = \frac{2J_1(\pi d_{\mathrm{ref}}\ \boldsymbol{r}_{\mathrm{p}}/\lambda z_{\mathrm{o}})}{\pi d_{\mathrm{ref}}\ \boldsymbol{r}_{\mathrm{p}}/\lambda z_{\mathrm{o}}}, \tag{3.13}$$

where, J_1 is the Bessel function of the first kind, grade one and $\boldsymbol{r}_{\mathrm{p}} = (x_{\mathrm{p}}; y_{\mathrm{p}})$ is the radius from the optical axis on the detector plane. Note that P_{ref} is not an Airy intensity pattern but represents the reference pinhole's electric field amplitude on the detector.

With the theoretical models for P_{ccd} and P_{ref}, the FTH transfer function P_{fth} can be derived by probing the entire FTH system with a δ-object. Considering Eq. (2.1) The

hologram recorded by the detector is given by:

$$\begin{aligned}|\mathcal{F}[d_{\mathrm{ref}}(\boldsymbol{r})] + \mathcal{F}[\delta(\boldsymbol{r}-\boldsymbol{r_o})]|^2 = \\ |P_{\mathrm{ref}}(\boldsymbol{r_p}) + P_{\mathrm{ccd}}(\boldsymbol{r_p})|^2 = |P_{\mathrm{ref}}(\boldsymbol{r_p})|^2 + |P_{\mathrm{ccd}}(\boldsymbol{r_p})|^2 \\ + P_{\mathrm{ccd}}(\boldsymbol{r_p})P_{\mathrm{ref}}(\boldsymbol{r_p})^* + P_{\mathrm{ccd}}(\boldsymbol{r_p})^* P_{\mathrm{ref}}(\boldsymbol{r_p}),\end{aligned} \tag{3.14}$$

where $\boldsymbol{r} = (x_o; y_o)$ is the radius from the optical axis in the object plane. $|P_{\mathrm{ccd}}|^2$ is a constant offset while the intensity $|P_{\mathrm{ref}}|^2$ describes an Airy pattern. The contributions that yield the (redundant) conjugated reconstructions are the last two terms of Eq. (3.14). These two terms describe the interference pattern between the plane wave from the δ-peak and the diffraction pattern of the reference pinhole:

$$P_{\mathrm{ccd}}P_{\mathrm{ref}}^* + P_{\mathrm{ccd}}^* P_{\mathrm{ref}} = 2Re[P_{\mathrm{ccd}}P_{\mathrm{ref}}]. \tag{3.15}$$

The factor 2 corresponds to the two conjugated redundant images in the reconstruction and is therefore neglected in the following discussion. The FTH pupil function which determines the frequency distribution of the object's reconstructed wave field thus given by:

$$P_{\mathrm{fth}} = Re[P_{\mathrm{ccd}}P_{\mathrm{ref}}]. \tag{3.16}$$

Therefore, P_{fth} represents the FTH system's entrance pupil (P_{ccd}) which is modulated by a second contribution (P_{ref}) from the reference pinhole. The fact that the imaginary part is not transferred by the FTH-system, results in a Fourier transform of the hologram that is Hermitian symmetric, i.e., it consists of two redundant, conjugated twin images that are located symmetrically to the center of the matrix.

From the physics perspective, the two conjugated twin-images reflect the off-axis geometry of the FTH-system. The separation between object and reference pinhole ($\boldsymbol{r_0}$ in Fig. 2.2) results in a relative phase difference $\theta(\boldsymbol{r_p})$ between the object and the reference wave on the detector as both waves arrive at different angles to the optical axis. For this reason, the interference of $P_{\mathrm{ccd}}P_{\mathrm{ref}}$ is complex and P_{fth}=$Re[P_{\mathrm{ccd}}P_{\mathrm{ref}}]$ disposes the imaginary part. Apart from real and imaginary part, the encoded phase can also be seen as the cosine of the entire object wave's phase:

$$\begin{aligned}P_{\mathrm{ref}}P_{\mathrm{ccd}}^* + P_{\mathrm{ref}}^* P_{\mathrm{ccd}} &= A_{\mathrm{ref}}A_{\mathrm{ccd}}e^{i\theta(\boldsymbol{r_p})} + A_{\mathrm{ref}}A_{\mathrm{ccd}}e^{-i\theta(\boldsymbol{r_p})} \\ &= 2A_{\mathrm{ref}}A_{\mathrm{ccd}}\,\cos[\theta(\boldsymbol{r_p})],\end{aligned} \tag{3.17}$$

where A_{ref} and A_{ccd} are the amplitudes of the waves from the reference and the δ-object in the far field. This cosine represents the high frequency modulation that encodes the object wave's phase information into the diffraction pattern. From the cosine of the phase (or equivalently from the real part of the interference pattern) alone, it can not be determined whether the object wave originated from $\boldsymbol{r_o}$ or $-\boldsymbol{r_o}$ as both scenarios lead to identical

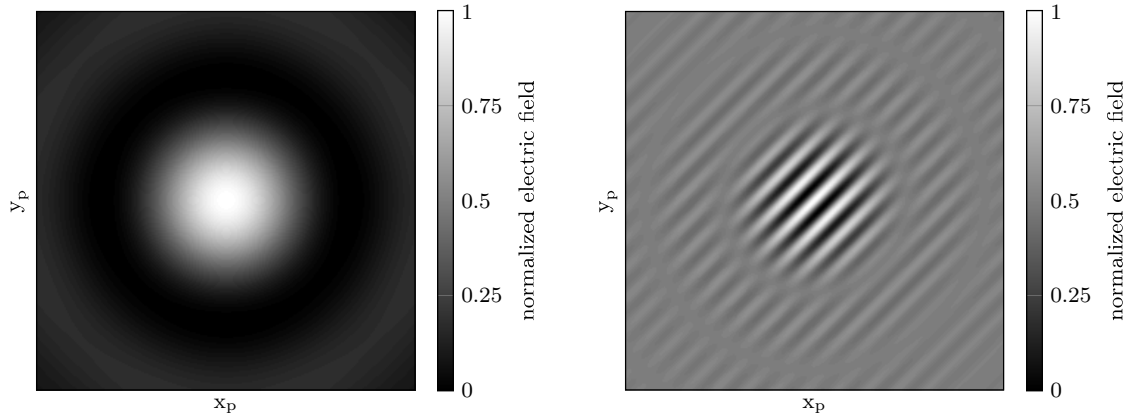

Figure 3.7: FTH pupil functions P_{ref} and P_{fth}. (a) The real valued reference pinhole pupil function P_{ref} on the detector. The reference source is centered on the optical axis. (b) The pupil function of the FTH system P_{fth} as generated by interference of P_{ref} with the detector pupil function P_{ccd}. The δ-function representing the object is separated from the reference pinhole by $\boldsymbol{r_0} = (c, c)$, where c is exemplary constant.

results. The reconstruction therefore shows two redundant "solutions" corresponding to both possible separation vectors.

Fig. 3.7(a) shows the central part of the real valued P_{ref}. The FTH transfer function P_{fth} for an exemplary constant c for the separation vector $\boldsymbol{r_o} = (c, c)$ is shown in panel (b). For $\boldsymbol{r_o} = (0, 0)$, P_{fth} equals P_{ref} on the detector as P_{ccd} is then real valued.

The modulation of P_{fth} describes the location of the two redundant object reconstructions in the Fourier transform of the hologram, whereas, the spatial frequency distribution of the desired object wave reconstructions within the object hole is determined by the shape of the reference diffraction pattern P_{ref} on the detector. For the following discussion of the FTH imaging properties, the modulation due to $\boldsymbol{r_o}$ is therefore ignored and the phase factor of P_{ccd} is dropped. P_{fth} is then represented by the real valued function of Eq. (3.13) multiplied by one within the detector area and zero outside.

From the pupil functions P_{ref} and P_{ccd}, the FTH system's transfer function $H_{\mathrm{fth}}(f_x, f_y) = H_{\mathrm{ccd}}(f_x, f_y) H_{\mathrm{ref}}(f_x, f_y)$ can be calculated. The pinhole's transfer function H_{ref} can be found by substituting $\boldsymbol{r}_{\mathrm{p}} = \boldsymbol{f}_{\mathrm{r}} \lambda z_{\mathrm{o}}$ in $P_{\mathrm{ref}}(\boldsymbol{r}_{\mathrm{p}})$:

$$H_{\mathrm{ref}}(\boldsymbol{f}_{\mathrm{r}}) = \frac{2J_1(\pi d_{\mathrm{ref}} \boldsymbol{f}_{\mathrm{r}})}{\pi d_{\mathrm{ref}} \boldsymbol{f}_{\mathrm{r}}}, \tag{3.18}$$

where $\boldsymbol{f}_{\mathrm{r}} = (f_{\mathrm{x}}; f_{\mathrm{y}})$ is the radius from the center (0;0) in the frequency domain. The PSF $h_{\mathrm{ref}} = \mathcal{F}[H_{\mathrm{ref}}]$ corresponds to an unfiltered reference pinhole of diameter d_{ref}. With the

system's magnification $M = p_{\mathrm{ccd}} s_{\mathrm{ccd}} / \lambda z_{\mathrm{o}}$ (Eq. (3.12)), h_{ref} can be specified by:

$$h_{\mathrm{ref}}(\boldsymbol{r}_{\mathrm{i}}) = \begin{cases} 1 & \text{if } \boldsymbol{r}_{\mathrm{i}} \leq \frac{d_{\mathrm{ref}} p_{\mathrm{ccd}} s_{\mathrm{ccd}}}{2\lambda z_{\mathrm{o}}} \\ 0 & \text{if } \boldsymbol{r}_{\mathrm{i}} > \frac{d_{\mathrm{ref}} p_{\mathrm{ccd}} s_{\mathrm{ccd}}}{2\lambda z_{\mathrm{o}}} \end{cases} \tag{3.19}$$

where $\boldsymbol{r}_{\mathrm{i}} = (x_{\mathrm{i}}; y_{\mathrm{i}})$ is the radius from the center of the object reconstruction in the image plane. The pupil function of the CCD is a square:

$$P_{\mathrm{ccd}}(x_{\mathrm{p}}, y_{\mathrm{p}}) = \mathrm{rect}\left(\frac{x_{\mathrm{p}}}{s_{\mathrm{ccd}}}\right) \mathrm{rect}\left(\frac{y_{\mathrm{p}}}{s_{\mathrm{ccd}}}\right), \tag{3.20}$$

The transfer function of the CCD (H_{ccd}) can be found by the substitutions $x_{\mathrm{p}} = f_x \lambda z_{\mathrm{o}}$ and $y_{\mathrm{p}} = f_y \lambda z_{\mathrm{o}}$:

$$H_{\mathrm{ccd}}(f_x, f_y) = \mathrm{rect}\left(\frac{f_x \lambda z_{\mathrm{o}}}{s_{\mathrm{ccd}}}\right) \mathrm{rect}\left(\frac{f_y \lambda z_{\mathrm{o}}}{s_{\mathrm{ccd}}}\right), \tag{3.21}$$

where f_x and f_y represent the object's spatial frequencies in x_{o} and y_{o} direction. The PSF $h_{\mathrm{ccd}} = \mathcal{F}[H_{\mathrm{ccd}}]$ is then given by:

$$\begin{aligned} h_{\mathrm{ccd}}(x_{\mathrm{i}}, y_{\mathrm{i}}) &= \mathrm{sinc}\left(\frac{x_{\mathrm{i}} s_{\mathrm{ccd}}}{\lambda z_{\mathrm{i}}}\right) \mathrm{sinc}\left(\frac{y_{\mathrm{i}} s_{\mathrm{ccd}}}{\lambda z_{\mathrm{i}}}\right) \\ &= \mathrm{sinc}\left(\frac{x_{\mathrm{i}}}{p_{\mathrm{ccd}}}\right) \mathrm{sinc}\left(\frac{y_{\mathrm{i}}}{p_{\mathrm{ccd}}}\right). \end{aligned} \tag{3.22}$$

From the transfer function H_{fth}, the FTH system's PSF h_{fth} can be calculated as follows:

$$h_{\mathrm{fth}} = \mathcal{F}(H_{\mathrm{fth}}) = \mathcal{F}(H_{\mathrm{ccd}} H_{\mathrm{ref}}) = h_{\mathrm{ccd}} \otimes h_{\mathrm{ref}} \tag{3.23}$$

Considering Eq. (3.19) and Eq. (3.22), the PSF of an FTH system with a circular pinhole reference is given by the convolution of a two-dimensional sinc pattern and a circular disk. The particular shape of h_{fth}, however, depends on the geometric setup, the reference pinhole diameter and the energy of the illumination light. In the following, the extremes of diffraction limited and reference limited resolution are examined. In the first case, h_{fth} is strongly dominated by h_{ccd} and h_{ref} is assumed to be a constant which is neglected. In the second case, h_{ccd} is constant (over an infinite area) and h_{fth} is thus represented by h_{ref}. Subsequently, the insights of how detector and reference affect the reconstruction are combined and the FTH system is examined for more realistic conditions.

In the following treatment of diffraction limited FTH, conditions are idealized as follows: (i) a square-shaped CCD is assumed to be sufficiently far away from the object to justify the far field approximations of the Fraunhofer diffraction theory, (ii) the object is assumed to be illuminated by a fully coherent plane wave, and (iii) the FTH system is assumed to be space-invariant.

3.4.1 Ideal diffraction limited resolution

The idealized, diffraction limited FTH system has a reference source that is assumed to be an infinitesimally small δ-like point-source which yields a plane wave-front at the CCD of finite size. The system's response to a second δ-peak representing the object is the diffraction limited PSF h_{ccd}. The system's transfer function H_{ccd} has the square-shape of the CCD and the PSF h_{ccd} describes a two-dimensional sinc pattern (Eq. (3.22)). Similar to the coherent, two-point resolution limit for circular entrance pupils, it is reasonable to define the diffraction limited resolution cut-off for FTH as the distance between two coherently superposed h_{ccd}-profiles that yields an image contrast of 15.3%. Such a defined separation can be found empirically by increasing the displacement between two coherently superposed sinc profiles continuously, starting from full overlap. For a square shape CCD, the diffraction limited resolution cut-off that yields 15.3% image contrast of the reconstructed wave field in y_{i} as well as in x_{i} direction is:

$$d_{\mathrm{amp}} = 0.755\lambda/\mathrm{NA}. \tag{3.24}$$

The distance d_{amp} thus represents the displacement between two point sources that can just be resolved by the diffraction-limited FTH-system. Fig. 3.8 shows an illustration of the diffraction limited resolution determination for the square-shaped H_{ccd}. The sinc-profile of h_{ccd} for the reconstructed wave field has pronounced side-lobes (see blue curve in Fig. 3.8(a)). Corresponding to an intensity image, the green curve in Fig. 3.8(a) shows the squared modulus ($|h_{\mathrm{ccd}}|^2$) of the sinc profile. The side-lobes for $|h_{\mathrm{ccd}}|^2$ are much suppressed compared to h_{ccd}. Additionally, $|h_{\mathrm{ccd}}|^2$ is more confined compared to h_{ccd}. The separation between two coherently superposed h_{ccd}-profiles that yields 15.3% image contrast is thus slightly larger compared to the distance that yields similar contrast for two coherently superposed $|h_{\mathrm{ccd}}|^2$ profiles (green curve in Fig. 3.8(b)). The corresponding resolution cut-off for the reconstructed intensity is:

$$d_{\mathrm{int}} = 0.724\lambda/\mathrm{NA}. \tag{3.25}$$

The profile of two coherently superposed h_{ccd}s separated by d_{int}, shows only 7.7% contrast (blue curve in Fig. 3.8(b)). Fig. 3.8(c) shows the conditions for a separation of d_{amp}. Here, the coherently superposed $|h_{\mathrm{ccd}}|^2$-profiles (green curve) yield 29.9% image contrast (cf. 15.3% contrast for the coherently superposed h_{ccd} profiles). In special cases of (non-magnetic) FTH applications with complete diffraction patterns (without a central beam stop shadow), it might be worth wile to use the squared modulus of the reconstruction ,i.e., the reconstructed intensity, rather than the wave field's complex amplitude to suppress ringing artifacts and improve the image contrast of high frequency features.

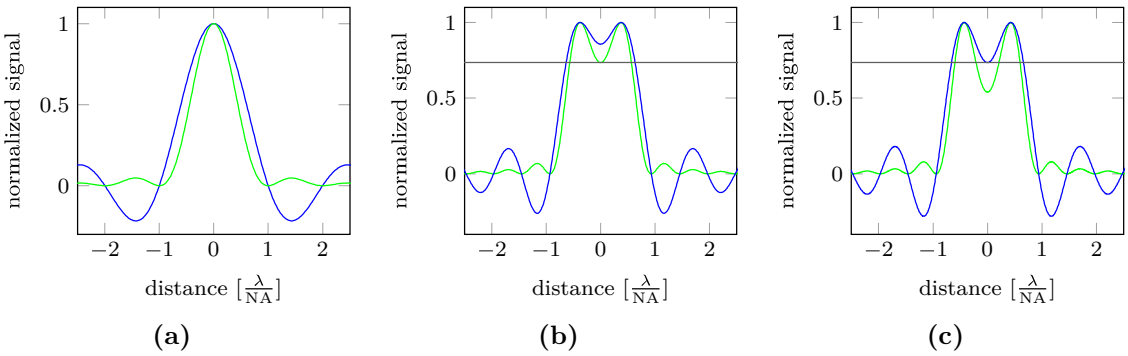

Figure 3.8: Resolution limit for the rectangular transfer function H_{ccd}. The green colored curves correspond to reconstructed intensity while the blue color represents the reconstructed wave field. (a) Line-profile of the diffraction-limited PSFs h_{ccd} (blue) and $|h_{\mathrm{ccd}}|^2$ (green). (b) Two-point resolution for a separation of $0.724\lambda/\mathrm{NA}$. Corresponding to 15.3% image contrast, the signal in the center between both maxima in the intensity reconstruction (green) is diminished by 27%. (c) Two-point resolution for a separation of $0.755\lambda/\mathrm{NA}$. Here, the amplitude reconstruction (blue) shows an image contrast of 15.3% while the intensity profile shows a contrast of 29.9% (green).

3.4.2 Ideal reference limited resolution

The idealized reference-limited FTH system has a circular reference source with a finite diameter of d_{ref} and an infinite-size detector area. The system's impulse response h_{ref} is thus the geometric image of the reference pinhole (see Eq. (3.19)). Contrary to diffraction-limited PSFs which have a point-like maximum in the center, h_{ref} is a circular disk so that the profile through the center is a rectangle.

Considering two closely spaced δ-peaks as objects, the results in the image can be characterized by analyzing the convolution of the δ-peaks with the rect-profile of h_{ref}. For a clear distinction of the two points in the image, the separation between the δ-peaks needs to be larger than d_{ref}. Separations of both δ-peaks smaller than d_{ref}, result in an overlap of the circular h_{ref}s in the image and thus yield an extended central maximum with a signal strength twice of h_{ref} (Fig. 3.9(a)). For separations larger than d_{ref}, the overlap disappears and the contrast inverses as the reconstructed amplitude between both h_{ref}-profiles drops to zero (Fig. 3.9(b)). Contrary to incoherent diffraction limited systems where the Rayleigh resolution limit corresponds to the radius of the PSF, the two-point resolution limit of the reference limited FTH system is the diameter d_{ref}.

Considering a binary grating of equally wide lines and spaces as a test pattern, the resolution capabilities of the FTH system can conveniently be evaluated by a gradual variation of the grating period. In Fig. 3.9, the resolution cut-off of such periodic test patterns is illustrated by convolving the rect-function of h_{ref} with a rectangular pulse-train of period p which represents the grating (see red curve in Fig. 3.9(f)). In order to afford a

comparison to conventional diffraction limited, incoherent systems with a circular entrance pupil, the pulse-train is also convolved with an Airy pattern (see green curve in Fig. 3.9(f)). The diameter of the central Airy disk equals thereby d_{ref}, i.e., $d_{\mathrm{ref}} = 1.22\lambda/\mathrm{NA}$.

This result shows that the contrast of the grating in the image vanishes when the grating-period approaches d_{ref}. Unlike diffraction limited systems where the contrast decreased strictly monotonic and features with sizes beyond the resolution limit are absent in the image, reference limited FTH may yield high contrast images also for feature-sizes smaller than d_{ref}. The contrast for reference limited FTH alternates around zero for decreasing p and culminates at -33% in a global minimum for p=2/3d_{ref}. The simulations presented in Fig 3.9(f) show that the grating contrast in the image dependent on p has zeros for:

$$p = \frac{d_{\mathrm{ref}}}{c} \;\forall\; c \in \mathbb{N} \;, \tag{3.26}$$

and extremal values for:

$$p = \frac{2d_{\mathrm{ref}}}{(2c+1)} \;\forall\; c \in \mathbb{N} \;. \tag{3.27}$$

The analysis of (strongly scattering) unknown features with sizes smaller than d_{ref} in the reconstruction of a reference-limited FTH setup is thus difficult and may result in misinterpretation.

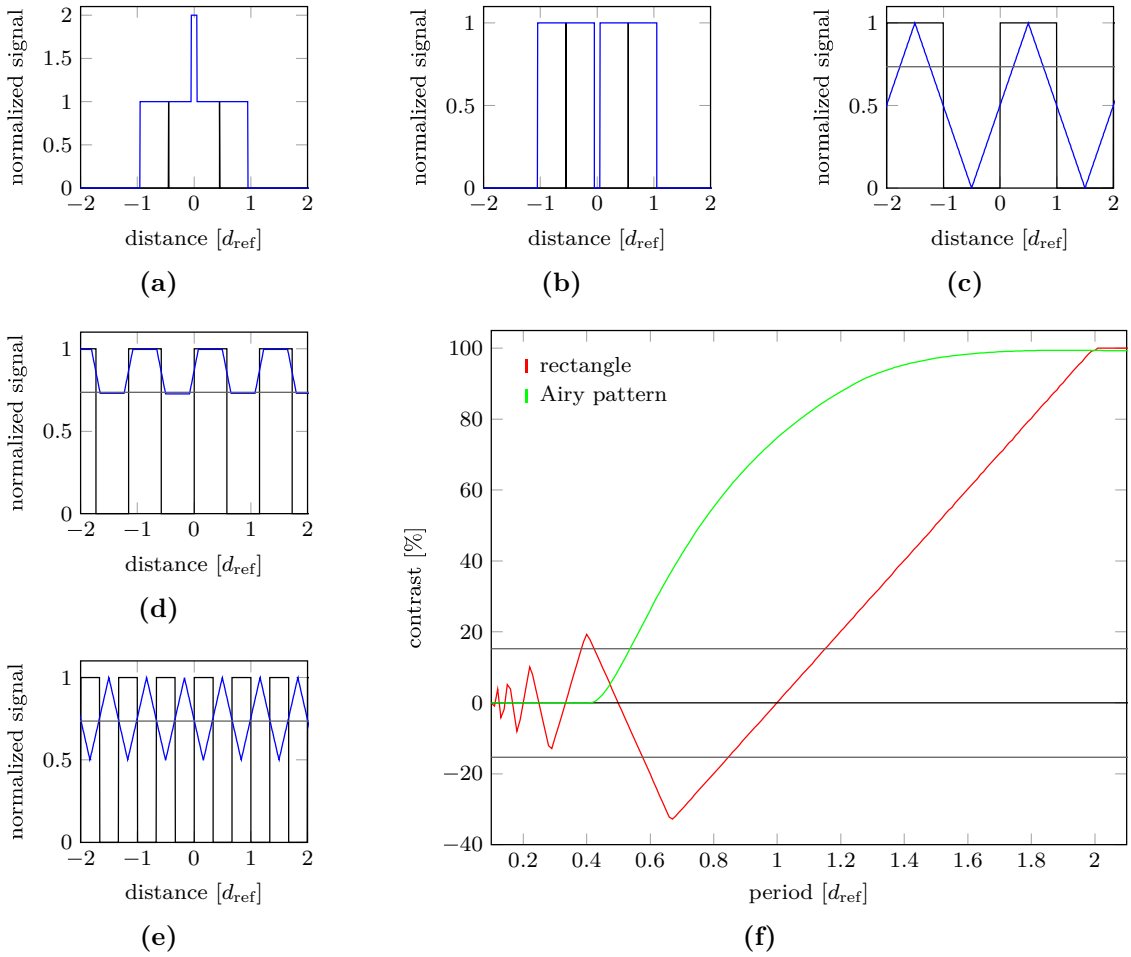

Figure 3.9: Reference-limited FTH contrast inversion simulated for small features. All line-profiles (blue) are obtained by convolving the input function (black) with the rectangular profile of h_{ref}. Input functions are two δ-peaks separated by $0.9d_{\mathrm{ref}}$ (a) and $1.1d_{\mathrm{ref}}$ (b) as well as profiles of binary line gratings with equally wide lines and spaces. For periods $p{>}2d_{\mathrm{ref}}$ the contrast is 100% (c). For $p{=}1.54d_{\mathrm{ref}}$ the contrast is 15.3% (d). Periods approaching $p{=}d_{\mathrm{ref}}$ yield a vanishing contrast which inverses for periods with $0.5d_{\mathrm{ref}}{<}p{<}d_{\mathrm{ref}}$. A peak contrast of -33% is reached for $p{=}2/3d_{\mathrm{ref}}$ (e). Panel (f) shows the grating contrast in the image dependent on p. For $p{<}d_{\mathrm{ref}}$ the contrast alternates and converges to zero for $p \ll d_{\mathrm{ref}}$. The green curve shows the contrast dependent on the grating period for a conventional diffraction limited system with an Airy disk PSF. The central Airy disk has a diameter of d_{ref}.

Plane of least confusion

The specific shape of h_{ref} may also impact reference-limited FTH reconstructions of features that are not in the plane of the integrated mask ,e.g., extended three-dimensional objects (see chapter 5), particularly if imaged with references that are much larger than the FTH system's diffraction limited PSF h_{ccd}. Such applications rely on a numeric refocusing

of the reconstruction by an application of the free-space propagator [Goo96; Pag06]. The refocus distance is then found as the plane of least confusion, i.e., the plane of optimal sharpness.

For small δ-like features in the object plane, the circumstances can be simulated by a numeric propagation of h_{ref}. Figure 3.10(a) shows the beam shape for a propagated pinhole of diameter d_{ref} in units of $d_{\mathrm{ref}}^2/4\lambda$, i.e., in units of the inverse *Fresnel number* (F^{-1}). For comparison to a conventional, diffraction limited system with circular entrance pupil, an Airy-disk is propagated in units of $d_{\mathrm{min}}^2/4\lambda$ (Fig. 3.10(b)). Here, d_{min} corresponds to the diameter of the central Airy disk. In order to recognize the beam's full width at half maximum (FWHM), the colormap is adjusted so that a signal strength of 0.5 corresponds to the color red.

For a propagation distance of $l_{\mathrm{prop}} = 0$ ($F = \infty$), the simulation for the diffraction limited system shows the Airy pattern which is the most confined form (in terms of FWHM) of the diffraction limited beam and shows maximum signal strength in the center (Fig. 3.10(d) and (f)). The depth-of-field for the diffraction limited case corresponds to the distance from the focus position on-axis where the signal drops by 20% [Att07].

The simulation for the reference limited FTH setup indicates that due to the extended maximum of h_{ref}, the plane of the mask does neither coincide with the plane of least confusion nor with the plane of maximum signal on axis (Fig. 3.10(c) and (e)). Instead, the diffraction pattern of the circular reference pinhole for different propagation lengths results in two beam waists that are located symmetrically before and behind the mask at $l_{\mathrm{prop}} = \pm d_{\mathrm{ref}}^2/4\lambda$ ($F = 1$). In between the two waists, the beam-diameter in terms of FWHM cannot continuously be specified as the central beam shows on-axis minima and side-lobes stronger than half of the maximum. The on-axis signal at the beam waist positions has a maximum and drops sharply for a propagation in mask direction (Fig 3.10(c)). The two depth-of-fields therefore extend asymmetrically around the planes of least confusion.

Fig. 3.11 shows the beam profiles at the waist positions in comparison to the initial PSF in the mask plane. The beam-width can be further reduced by high-pass filtering the hologram. As discussed in chapter 3.4.3, the resolution limit of two-dimensional, strongly reference limited reconstructions can be improved by propagating the reconstructed object wave field into one of the beam waists (such a reconstruction can be further treated to remove superimposed artifacts from the opposite beam-waist, see chapter 4). In this context, the reference pinhole may be regarded as a primitive single-zone FZP and the waist positions at $l_{\mathrm{prop}} = \pm d_{\mathrm{ref}}^2/4\lambda$ can be interpreted as focal lengths. The relation between focal length and beam waist becomes clear if d_{ref} is understood as the diameter $2r_{\mathrm{fzp}}$ of the first FZP zone. The first order focal lengths for an FZP with N zones are given by $f_{\mathrm{fzp}} = \pm r_{\mathrm{fzp}}^2/(N\lambda)$ and coincide for $N = 1$ with $\pm d_{\mathrm{ref}}^2/4\lambda$.

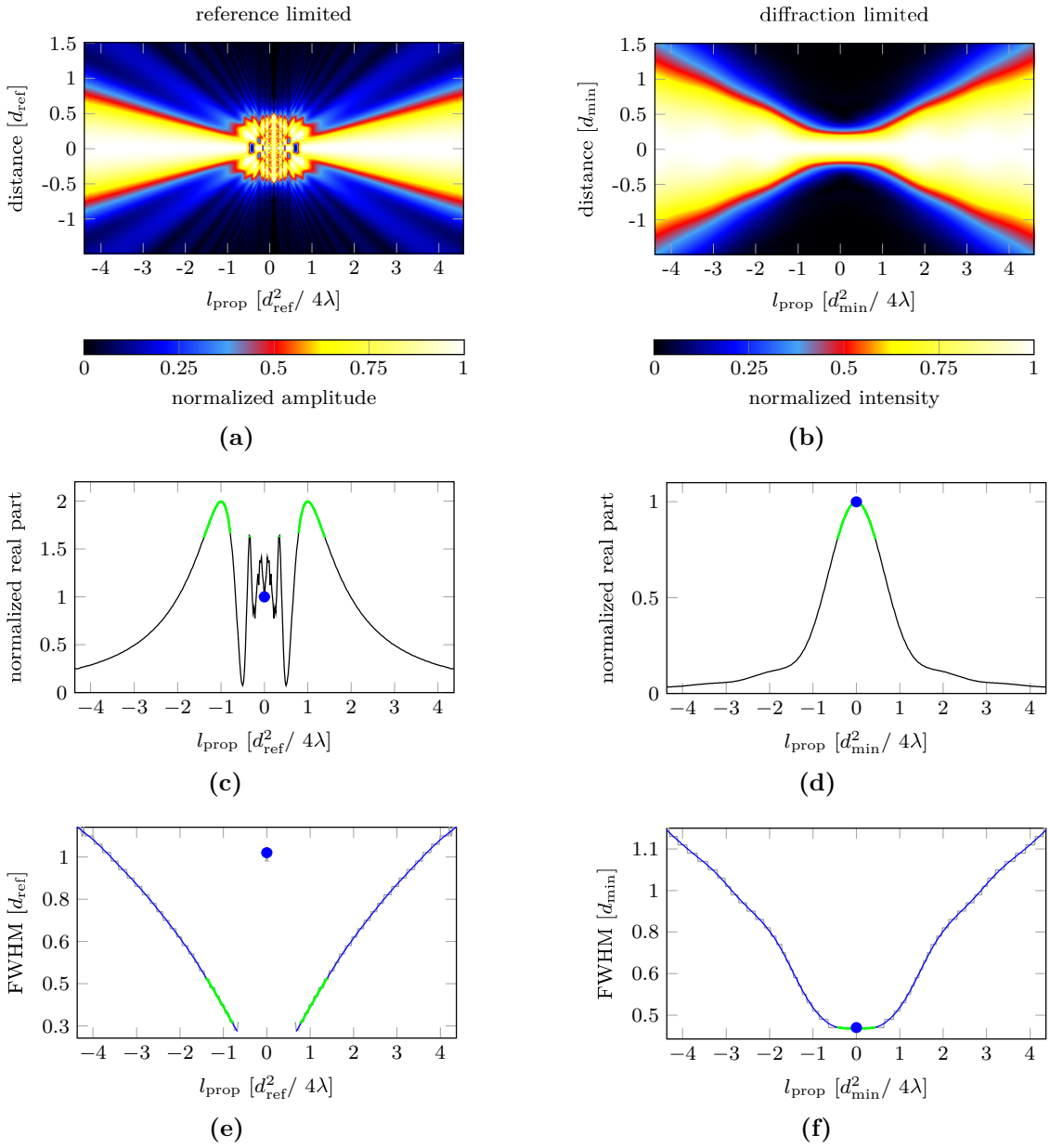

Figure 3.10: Longitudinal shape and signal of the reference PSF h_{ref} compared to a PSF of a conventional diffraction limited system with circular aperture. (a) Shape of h_{ref} along the beam axis. The diameter for propagation distance $l_{\mathrm{prop}} = 0$ is d_{ref} (b) Shape of a diffraction limited beam along the beam axis. Here, d_{min} corresponds to the diameter of the central Airy disk at $l_{\mathrm{prop}} = 0$. Plots (a) and (b) are obtained by numerical propagation of the respective PSF. The signal for each propagation distance is normalized to the maximum signal at the particular propagation distance. Panels (c) and (d) show the signal on axis, normalized to the signal at $l_{\mathrm{prop}} = 0$ dependent on the propagation distance. The depth-of-field corresponding to a 20% drop of signal intensity on axis is indicated by the green color. The initial position of distance $l_{\mathrm{prop}} = 0$ is indicated by a blue circle. The gray line in (e) and (f) show the full width at half maximum (FWHM) dependent on $l_{\mathrm{prop}} = 0$ as obtained from the pixelated simulation. The blue curve is a smoothing spline which was fitted to the measured FWHM. The FWHM is minimal at the zero position only for the diffraction limited beam (f). The FWHM of the simulation for the reference limited beam (e) can not continuously be specified. Maximum signal intensity on-axis as well as minimal beam width do not match the zero propagation distance.

A pinhole that is large compared to the diffraction limited h_{ccd} of an FTH setup may thus be seen as a defocused image of a more confined PSF. In fact, artifacts similar as discussed for Fig. 3.9 have also been described for diffraction limited imaging systems as *defocus aberrations*. The shape of the defocused, diffraction limited PSF then deviates from the Airy pattern which results in frequency-dependent contrast inversions in the image [Goo96].

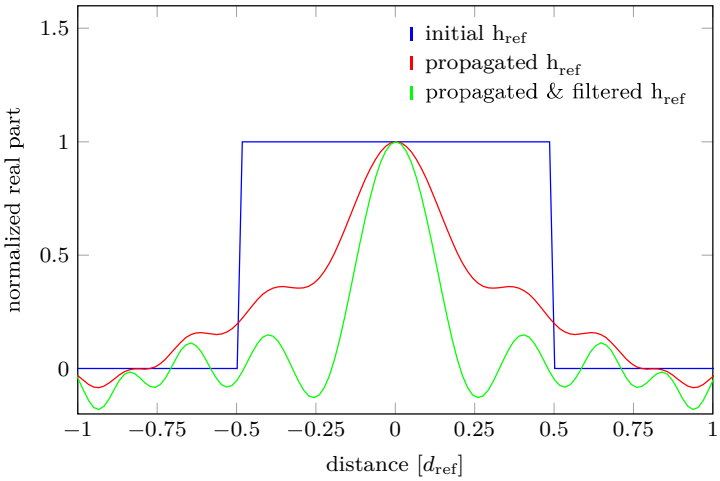

Figure 3.11: Profiles of the reference PSF in the mask plane (blue) and after propagation by $l_{\mathrm{prop}} = \pm d_{\mathrm{ref}}^2/4\lambda$ (red). The beam width is further reduced if the hologram is high-pass filtered (green)

3.4.3 High resolution imaging with X-ray Fourier transform holography

So far, the determination of the resolution cut-off and the descriptions of imaging characteristics of the FTH system were based on idealized assumptions. Some of these assumptions, namely, infinitesimally small references or infinite-sized detectors, are extremes and can not represent reality. The next step is to anticipate how high spatial frequency features are transferred into the image by a more realistically modeled FTH system. In the following, the FTH system is assumed to have a reference of finite diameter, as well as a finite size CCD detector. Technical limitations like limited photon flux or detector noise are ignored and the resolution capabilities of the FTH setup can be understood as a limiting boundary which can be achieved when conditions are ideal.

The square-shaped H_{ccd} as well as the finite-sized reference pinhole impact the system's transfer function (H_{fth}) contiguously. Depending on the side length of the CCD (s_{ccd}) relative to the diameter of the central Airy disk of the reference pinhole on the detector ($d_{\mathrm{Airy}} = 2.44 z_o \lambda / d_{\mathrm{ref}}$), the system's impulse response is filtered by the CCD transfer function H_{ccd}. In FTH, the relation of the diameter of the central Airy disk versus the detector dimensions is a decisive factor, even though the reference pinhole's pupil function

P_{ref} is actually not an Airy intensity pattern and rather corresponds to the real part of the reference wave on the detector (see Eq. (3.13)). Nevertheless, P_{ref} has identical zero values with the corresponding Airy pattern $|P_{\mathrm{ref}}|^2$. The central contribution of P_{ref} within the region bound by the first zero value has therefore the same size as the reference pinhole's central Airy disk. In order to investigate FTH image formation, the ratio R_{Airy} can thus be defined as follows:

$$R_{\mathrm{Airy}} = \frac{d_{\mathrm{ref}} s_{\mathrm{ccd}}}{2.44 z_o \lambda}. \tag{3.28}$$

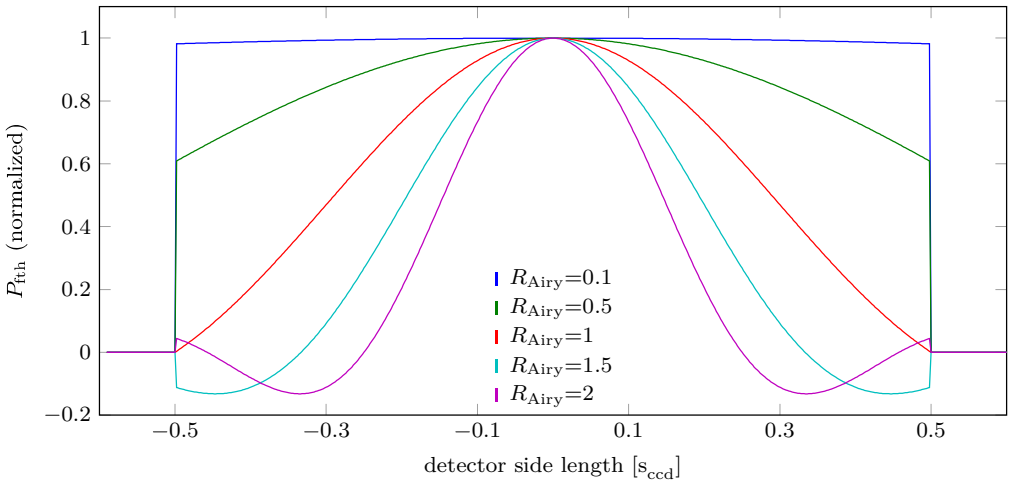

Figure 3.12: Normalized FTH pupil function P_{fth} for different ratios of R_{Airy}. For detector dimensions much smaller than the central Airy disk of the reference on the detector ($R_{\mathrm{Airy}} \ll 1$), the FTH pupil function is approximately constant (blue curve). For more common configurations, the central reference Airy disk fits on the detector ($R_{\mathrm{Airy}} \gtrapprox 1$) and high spatial frequencies are strongly suppressed by the FTH system. Transfer functions with $R_{\mathrm{Airy}} > 1$ have negative contributions and show contrast inversion for corresponding frequencies (cyan and purple curves).

Fig. 3.12 shows normalized FTH pupil functions for different values of R_{Airy}. For $R_{\mathrm{Airy}} > 1$, the diameter of the central Airy disk from $|P_{\mathrm{ref}}|^2$ is smaller than the detector side length s_{ccd}. In this case, P_{fth} contains frequency bands that negate the amplitudes of the corresponding spatial frequencies of the object. For $R_{\mathrm{Airy}} < 1$, the CCD side length is smaller than the central part of the reference pinhole's Airy disk. Fig. 3.12 indicates that for high-resolution FTH, the aim of nearly diffraction limited imaging is challenging. For coherent, diffraction-limited imaging, P_{fth} is required to be constant. An approximately constant P_{fth} can only be realized by using a small R_{Airy}, i.e., a small reference pinhole. However, the reference signal is proportional to the pinhole area and depends thus quadratically on the reference diameter. Due to the fact that the resolution

of an approximately diffraction-limited FTH setup is not set by the reference pinhole diameter but by the system's opening angle, the decrease in signal strength of the reference beam does not necessarily pay off with significantly improved resolution. For this reason, the aim of diffraction limited imaging necessitates unreasonably small reference diameters and thus contradicts a highly photon efficient FTH setup.

Realistically, large diffraction angles within the angular resolution limit of the detector are more or less suppressed by common FTH systems, depending on the finite reference pinhole diameter d_{ref} and the resulting shape of H_{fth}. Therefore, the signal for finer features declines in the image, even for specimen that generate strong scattering signals at large diffraction angles. Fig. 3.13 shows h_{fth} for different R_{Airy}. For $R_{\mathrm{Airy}} \lessapprox 1$, h_{fth} strongly deviates from the circular symmetric shape of h_{ref} due to the rectangular shape of H_{ccd}. The resolution limit in the reconstruction depends thus on the angle in the image plane. Utilizing a $R_{\mathrm{Airy}} \gg 1$ results in a h_{fth} that approximates the circular symmetric h_{ref} and yields an angle independent resolution in the reconstruction.

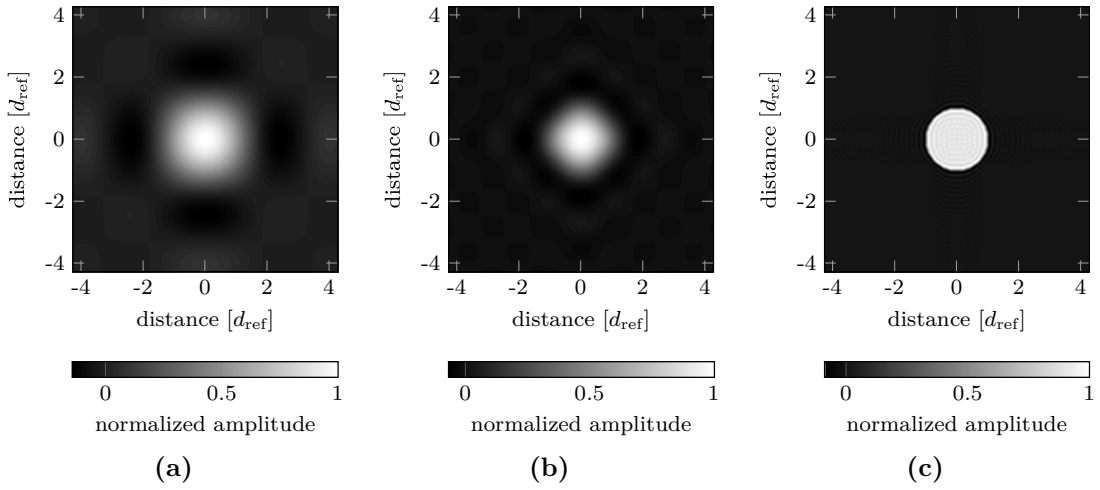

Figure 3.13: The PSF h_{fth} dependent on R_{Airy} (amplitude). (a) $R_{\mathrm{Airy}} = 0.5$, h_{fth} is dominated by the detector PSF h_{ccd}. (b) h_{fth} for $R_{\mathrm{Airy}} = 1$, the impact of h_{ccd} and the reference PSF h_{ref} is clearly visible. (c) For $R_{\mathrm{Airy}} = 10$, h_{fth} is dominated by h_{ref}.

Since the resolution limit is directly connected to the width of the PSF, it is desirable to anticipate an optimal configuration which yields the most confined PSF. Fig. 3.14(a) shows the profile of h_{fth} for characteristic R_{Airy}. For large $R_{\mathrm{Airy}} \gg 1$, the shape of h_{fth} approximates rectangular profile of h_{ref} whereas for small $R_{\mathrm{Airy}} < 1$, h_{fth} converges to the diffraction limited sinc profile of h_{ccd}.

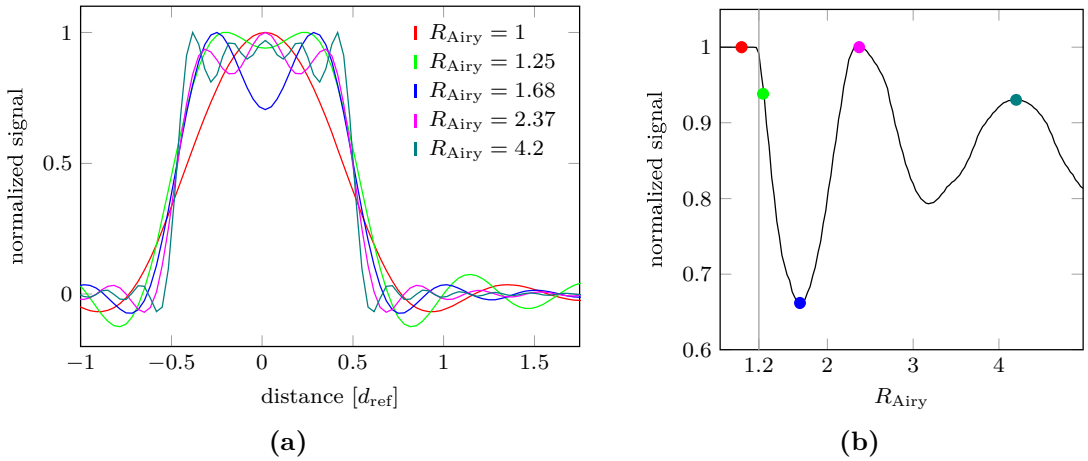

Figure 3.14: (a) Profile of h_{fth} in x_{i} direction dependent on R_{Airy} normalized to the maximum signal. For $R_{\mathrm{Airy}} = 1$, h_{fth} shows a global point-like maximum in the center. Larger R_{Airy} show secondary local extrema for the central part of h_{fth} within the radius of the first zero value. (b) The signal in the center of h_{fth}, normalized to the maximum of h_{fth} dependent on R_{Airy}. Only for $R_{\mathrm{Airy}} < 1.2$ the central part of h_{fth} shows a global maximum without secondary extrema within the radius of the first zero.

Apart from the width of the PSF, also the signal in the center of h_{fth} dependent on R_{Airy} is interesting. Airy-shaped PSFs with a central, point-like maximum are optimally confined, i.e., the shape corresponds to the beam-waist (Fig. 3.10(f)). Additionally, such PSFs do not cause imaging artifacts of small features beyond the resolution limit (Fig. 3.9(f)). Similar to the Airy pattern, a beneficial shape of h_{fth} presumably shows a global maximum in the center without additional local extrema within the radius of the first zero value. The signal in the center of h_{fth} normalized to the global maximum of h_{fth} dependent on R_{Airy} is shown in panel (b). For R_{Airy} approaching 1.2, the central maximum flattens out and changes into an extended plateau. For $R_{\mathrm{Airy}} > 1.2$, the central part of h_{fth} within the first zero shows several local extrema.

Enhancing reference limited FTH by applying a low-pass filter

From Fig. 3.14 it can be concluded that large R_{Airy} are not beneficial for the following reasons. Firstly, the width of h_{fth} for $R_{\mathrm{Airy}} \gg 1$ does not significantly improve, secondly, spatial frequencies beyond the first zero value of H_{ref} potentially cause imaging artifacts, and thirdly, h_{fth} does not seem to be optimally confined. The imaging artifacts can already be inferred from the transfer function (Fig. 3.12). Frequencies outside the radius of the first zero of H_{fth} do thus not contribute to the resolving power of the FTH system when imaging unknown specimen. For these reasons it should be possible to low-pass filter the hologram (hence effectively reducing R_{Airy}) and thereby avoid imaging artifacts without

degrading the resolution in the reconstruction.

In order to find the optimal filter radius (r_{cut}) for the low-pass filter that filters the hologram, a cut-off ratio (C_{Airy}) is defined as:

$$C_{\mathrm{Airy}} = \frac{d_{\mathrm{ref}}\, r_{\mathrm{cut}}}{1.22 z_o \lambda}. \tag{3.29}$$

C_{Airy} is thus the ratio of the cut-off radius of the low-pass filter in the detector plane, relative to the radius of the central Airy disk on the detector. In order to find an optimal C_{Airy}, the FWHM of h_{fth} is evaluated while r_{cut} is varied. Fig. 3.15(a) shows the FWHM dependent on C_{Airy} with a global minimum for $C_{\mathrm{Airy}} = 1$. The FWHM of h_{fth} is thus most confined if all frequencies outside the radius of the first zero of H_{fth} are deleted. Panel (b) shows $h'_{\mathrm{fth}} = \mathcal{F}[H'_{\mathrm{fth}}]$, with H'_{fth} representing the FTH transfer function cut at $f_{\mathrm{cut}} = 1.22/d_{\mathrm{ref}}$, i.e., in the recorded hologram, all pixels with $r_{\mathrm{cut}} > 1.22 z_o \lambda / d_{\mathrm{ref}}$ are multiplied by zero. The shape of h'_{fth} is now transformed into a more beneficial form with a central, point-like maximum and the FWHM is reduced to $0.78 d_{\mathrm{ref}}$. The two-point resolution limit for a such filtered h'_{fth} that yields 15.3% image contrast (Fig. 3.15(c)) is reduced to $d_{\mathrm{fth}} = 0.93 d_{\mathrm{ref}}$. Since the filtered H'_{fth} is apodized, h'_{fth} has less pronounced side-lobes compared to h_{fth}. Therefore, ringing artifacts that potentially affect the reconstruction of strongly scattering specimen are suppressed.

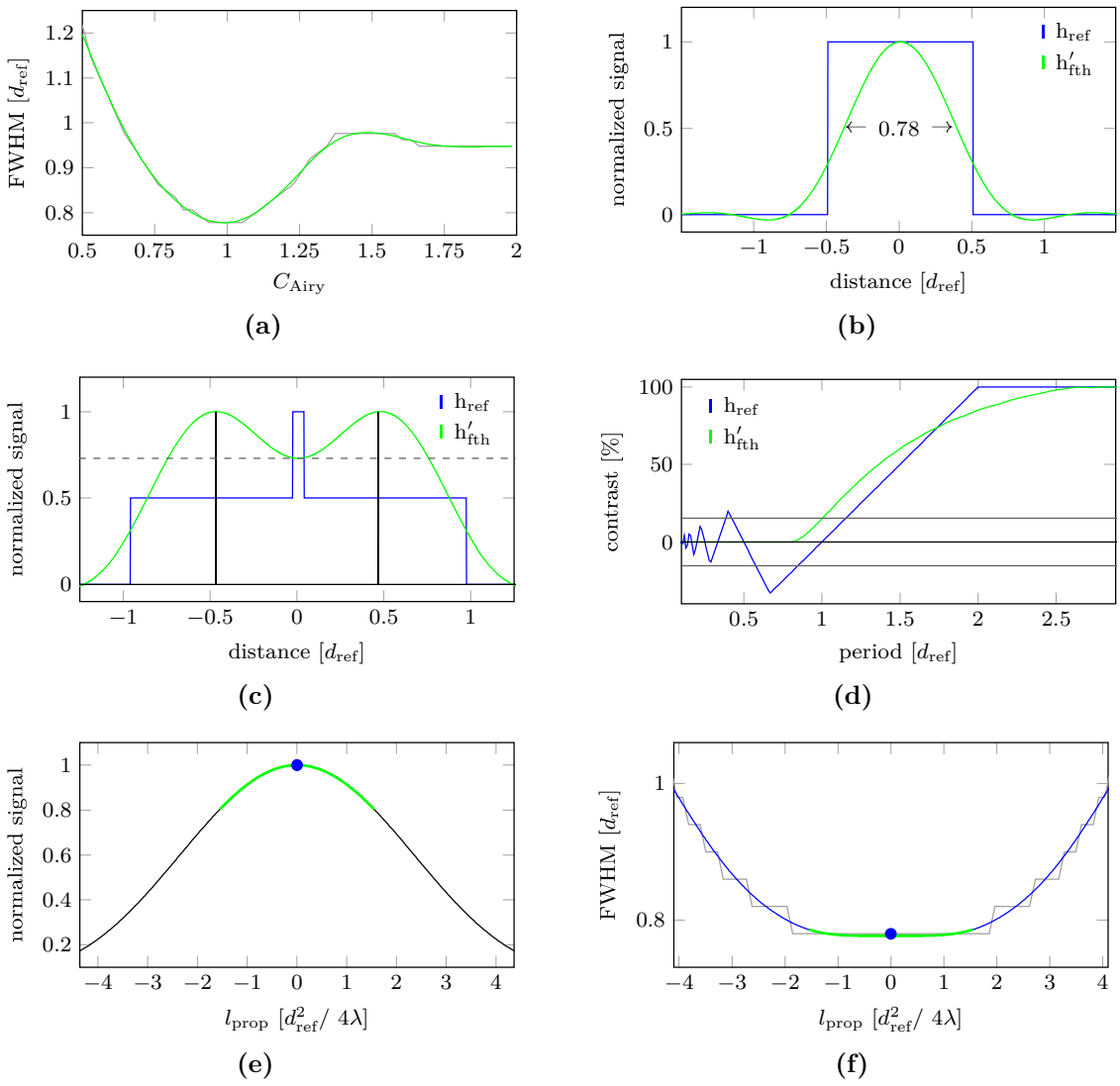

Figure 3.15: Resolution obtained by low-pass filtering of h_{ref}. (a) The FWHM of h_{fth} after low-pass filtering in units of d_{ref} dependent on C_{Airy}. For $C_{\mathrm{Airy}} = 1$ ($r_{\mathrm{cut}} = 1.22\lambda z_o/d_{\mathrm{ref}}$), the FWHM is minimal and h_{fth} is optimally confined. (b) The line profile of the unfiltered h_{ref} versus h'_{fth} which is low-pass filtered with $C_{\mathrm{Airy}} = 1$, the FWHM of h'_{fth} is reduced by a factor of 0.78. (c) For h'_{fth}, two points separated by $0.93d_{\mathrm{ref}}$ yield 15.3% image contrast. (d) Contrast of line gratings dependent on grating period. The contrast inversion as seen for h_{ref} is circumvented by the filtered h'_{fth}. (e) Normalized signal on axis for different propagation lengths of h'_{fth}. The signal shows a global maximum for $l_{\mathrm{prop}} = 0$. (f) The beam width of h'_{fth} (FWHM) dependent on the propagation length. The FWHM shows a global minimum for $l_{\mathrm{prop}} = 0$. The green color in panels (e) and (f) show the depth-of-field corresponding to a 20% drop of the signal on axis. The gray line in panel (a) and (f) show the FWHM obtained from the pixelated simulation. The green and blue curves in panel (a) and (f) are smoothing splines.

Fig. 3.15(d) shows the image contrast for gratings of period p with equally wide lines and spaces convoluted with h'_{fth}. For such gratings, the 15.3% contrast criterion for h'_{fth} improves to $1d_{\mathrm{ref}}$ versus $1.15d_{\mathrm{ref}}$ for unfiltered h_{fth}. Furthermore, the contrast inversion of h_{ref} which occurs for small features can be avoided.

Fig. 3.15(e) and (f) show the on-axis signal and FWHM of h'_{fth} for different propagation distances l_{prop} respectively. Unlike h_{ref} (Fig. 3.10), the filtered h'_{fth} has a single beam waist which extends symmetrically around the plane of least confusion at $l_{\mathrm{prop}} = 0$. Similar to the diffraction limited depth-of-field of Airy-shaped PSFs, the signal on axis is maximal at $l_{\mathrm{prop}} = 0$. Another advantage of h'_{fth} over the unfiltered h_{fth} is that h'_{fth} is circular symmetric and the resolution in the reconstruction is thus expected to be angle-independent.

As already suggested for the diffraction limited case, the image quality is theoretically further improvable if the reconstruction of the image intensity instead of the complex amplitude is considered (Fig. 3.16). In such an intensity reconstruction, the much suppressed side-lobes of h'_{fth} almost vanish and the contrast of small features in the image is enhanced. The FWHM for $|h'_{\mathrm{fth}}|^2$ improves to $0.56d_{\mathrm{ref}}$ (c.f. $0.78d_{\mathrm{ref}}$ for h'_{fth}). For two points spaced by $0.93d_{\mathrm{ref}}$, the contrast improves from 15.3% to 30.5%. The resolution limit defined by 15.3% image contrast for two closely spaced points in the intensity reconstruction is improved to $0.87d_{\mathrm{ref}}$. A non-linear manipulation such as squaring the modulus of the reconstruction might be justifiable since intensity images are the standard for most imaging systems including the human eye.

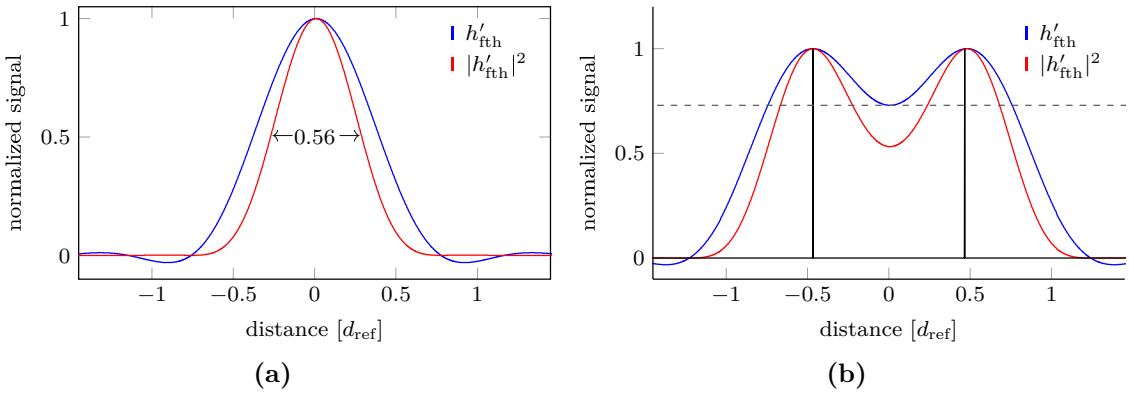

Figure 3.16: Beam width (FWHM) and two-point resolution limit for a low pass filtered $|h'_{\mathrm{fth}}|^2$ compared to h'_{fth}. (a) The width of h'_{fth} compared to the width $|h'_{\mathrm{fth}}|^2$. For the reconstructed image intensity, the width of the PSF reduces to $0.56d_{\mathrm{ref}}$. Compared to the reconstructed amplitude (blue), the side-lobes for $|h'_{\mathrm{fth}}|^2$ are significantly suppressed. (b) Two points spaced by $0.93d_{\mathrm{ref}}$ show 30.5% image contrast for reconstructed intensity.

Apart from the resolution limit, it is desirable that the reconstruction represents the transmission function of the object as realistically as possible. Another way to approach

the question whether low pass filtering a reference limited hologram is beneficial or not is to compare the reconstruction of a specimen with a broad bandwidth of spatial frequencies (g_i) to the original test pattern (g_o). A reasonable frequency cut-off for H'_fth should deliver an output that optimally resembles the input. Such a resemblance can be determined by comparing the correlation coefficients of input and output for different cut-offs r_cut of the FTH pupil function (P'_fth). The correlation coefficient (CC) is a measure of the linear association between two variables and is defined as follows [Bod09]:

$$CC = \frac{\sum\limits_{x_i,y_i} [g_\mathrm{i}(x_i,y_i) - \overline{g_\mathrm{i}}][g_\mathrm{o}(x_o,y_o) - \overline{g_\mathrm{o}}]}{\sqrt{\sum\limits_{x_i,y_i} [g_\mathrm{i}(x_i,y_i) - \overline{g_\mathrm{i}}]^2}\sqrt{\sum\limits_{x_o,y_o} [g_\mathrm{o}(x_o,y_o) - \overline{g_\mathrm{o}}]^2}}, \tag{3.30}$$

where $\overline{g_\mathrm{o}}$ and $\overline{g_\mathrm{i}}$ are the arithmetic means of the original test pattern in the object plane and the reconstruction in the image plane respectively. For identical g_o and g_i, the CC is one while for an inverse relationship between both variables the CC is minus one. For entirely uncorrelated g_o and g_i CC is zero. Fig 3.17 shows a comparison of the correlation coefficient for different sector stars with outermost periods (p_o) between $4d_\mathrm{ref}$ and $10d_\mathrm{ref}$. The correlation coefficient is plotted dependent on C_Airy and shows a maximum for a cut-off radius r_cut that coincides with the first zero of P_fth, i.e., at $C_\mathrm{Airy} = 1$. For specimen with larger features, the curves in Fig. 3.17(a) become more flat, indicating that the results of filtering H_fth are less significant for such patterns. While filtering the hologram seems to be advantageous for specimen with small features, it does not seem to negatively affect the reconstruction of larger features.

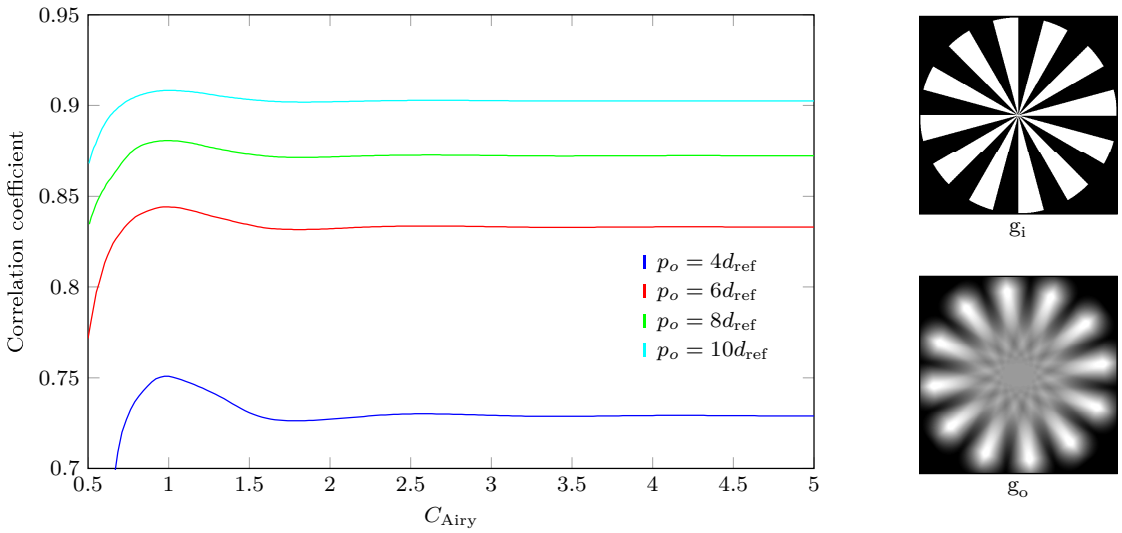

Figure 3.17: Correlation coefficient of a simulated FTH reconstruction (g_i) correlated with the original input (g_o) dependent on C_{Airy}. The test pattern for the simulation are sector stars with differently large outermost periods p_o. In all cases, the correlation coefficient is maximal at $C_{\mathrm{Airy}} = 1$

Resolution enhancement of strongly reference limited FTH

For transfer functions H_{fth} with sufficiently large R_{Airy}, the evaluation in chapter 3.4.2 indicates that the resolution is improvable by propagating the reconstruction into one of the reference beam waists. So far, the beam waist positions for $R_{\mathrm{Airy}} \gg 1$ were identified to $l_{\mathrm{prop}} = \pm d_{\mathrm{ref}}^2/4\lambda$. For $C_{\mathrm{Airy}} \leq 1$, the beam-waist is at $l_{\mathrm{prop}} = 0$. In order to estimate whether or not a propagation into the reference beam waist is beneficial, the FWHM for different values of C_{Airy} is evaluated.

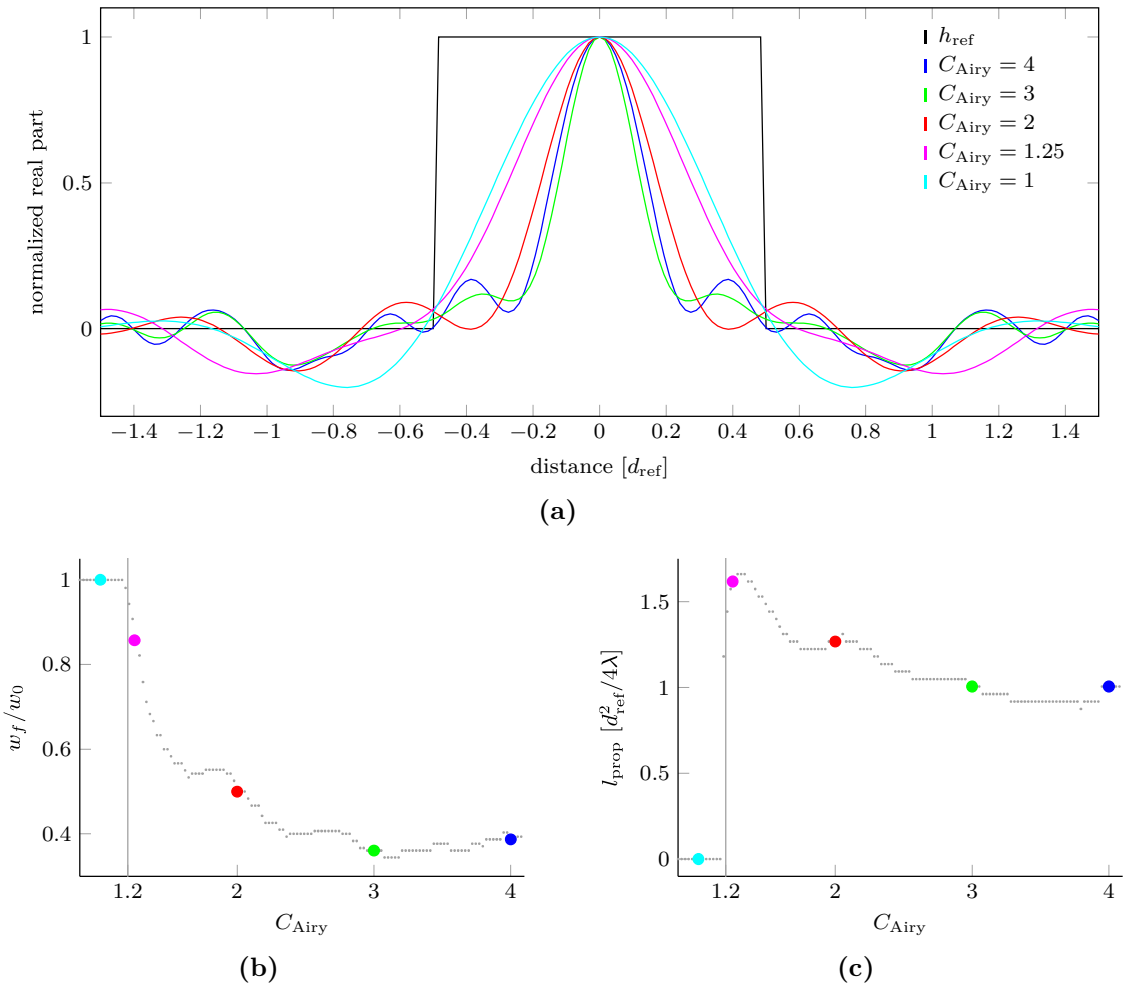

Figure 3.18: Focused h_{fth} for different C_{Airy}. (a) Profile in x_{i} direction of h_{fth} for different C_{Airy} after propagating into the beam waist. The dashed line represents the unfiltered profile of h_{ref} at $l_{\mathrm{prop}} = 0$. In order to remove the pinhole's undiffracted zero order contribution, h_{fth} is high pass filtered. (b) Beam width of the focused h_{fth} (w_f) relative to the width of h_{fth} in the mask plane (w_0) dependent on C_{Airy}. (c) Beam waist positions of h_{fth} dependent on C_{Airy}. The colored circles in panel (b) and (c) correspond to the legend in panel (a)

Fig 3.18(a) shows the beam profiles of h_{fth} in their respective beam waist position for different C_{Airy} between 1 and 4. The beam waist positions were found by observing the FWHM dependent on l_{prop}. In order to remove undiffracted zero order light, the propagated h_{fth} are high-pass filtered. The ratio of the beam width (FWHM) for h_{fth} at the beam waist position (w_f) relative to the width at $l_{\mathrm{prop}} = 0$ (w_0) dependent on C_{Airy} is shown in Fig. 3.18(b). For $C_{\mathrm{Airy}} > 2$ the beam width approximates 40% (FWHM) of the initial value (before propagation) and does not improve significantly for larger

C_{Airy}. For large C_{Airy}, the FWHM of the beam in the mask plane is therefore larger by a factor of approximately 2.5 compared to the FWHM of the reference beam in one of the beam waists. The beam waist position in units of $d_{\mathrm{ref}}^2/4\lambda$ is shown in Fig. 3.18(c). For $C_{\mathrm{Airy}} < 1.2$, h_{fth} is not most confined at $l_{\mathrm{prop}} = 0$ and shows two distinct beam waists. The beam waist position approximate $l_{\mathrm{prop}} = \pm d_{\mathrm{ref}}^2/4\lambda$ for $C_{\mathrm{Airy}} > 2$.

Apart from a numerical propagation of the reconstruction into the reference beam waist, also the knowledge of the transfer function H_{fth} allows to circumvent the contrast inversion and to improve the resolution of a strongly reference limited FTH reconstruction. In this case, an enhanced image can be retrieved by the deconvolution of the object wave reconstruction from the PSF $h_{\mathrm{fth}} = \mathcal{F}(H_{\mathrm{fth}})$. In an FTH experiment, H_{fth} can be retrieved by measuring the reference intensity pattern ($|P_{\mathrm{fth}}|^2$) without the object wave on the detector. From $|P_{\mathrm{fth}}|^2$, P_{fth} can easily be calculated as the zeros are identical and the function is real valued (Eq. (3.16)). Also the sign of the side-lobes between the zeros is known (central positive maximum with alternating side-lobes for larger radii). Another more simple way to improve the reconstruction is to negate the negative parts of H_{ref}. This can already be accomplished if only the zeros of H_{ref} are known. The zeros of H_{fth} can be measured with a sector star which is manufactured next to the object to be imaged. Object and sector star can be arranged that their reconstructions rely on the same reference.

Fig. 3.19(a) shows the transfer function and the simulated reconstruction of a sector star test pattern. In consistency with the transfer function, the simulation shows the contrast inversion for small periods as described above. Panel (b) shows the reconstruction after multiplying specific regions of the hologram by minus one. The negated regions thereby correspond to the negative parts of the original transfer function. The enhanced transfer function is non-negative but the zeros are still unchanged. Therefore the reconstruction of the sector star shows very weak contrast at corresponding periods. The reconstruction might be further improvable – via reference multiplexing [Sch06] – by utilizing a second reference with a transfer function that shows a local maximum at the first zero position of the initial transfer function. By combining the reconstructions of both pinholes, the spatial frequencies at the first zero of H_{fth} can be retained.

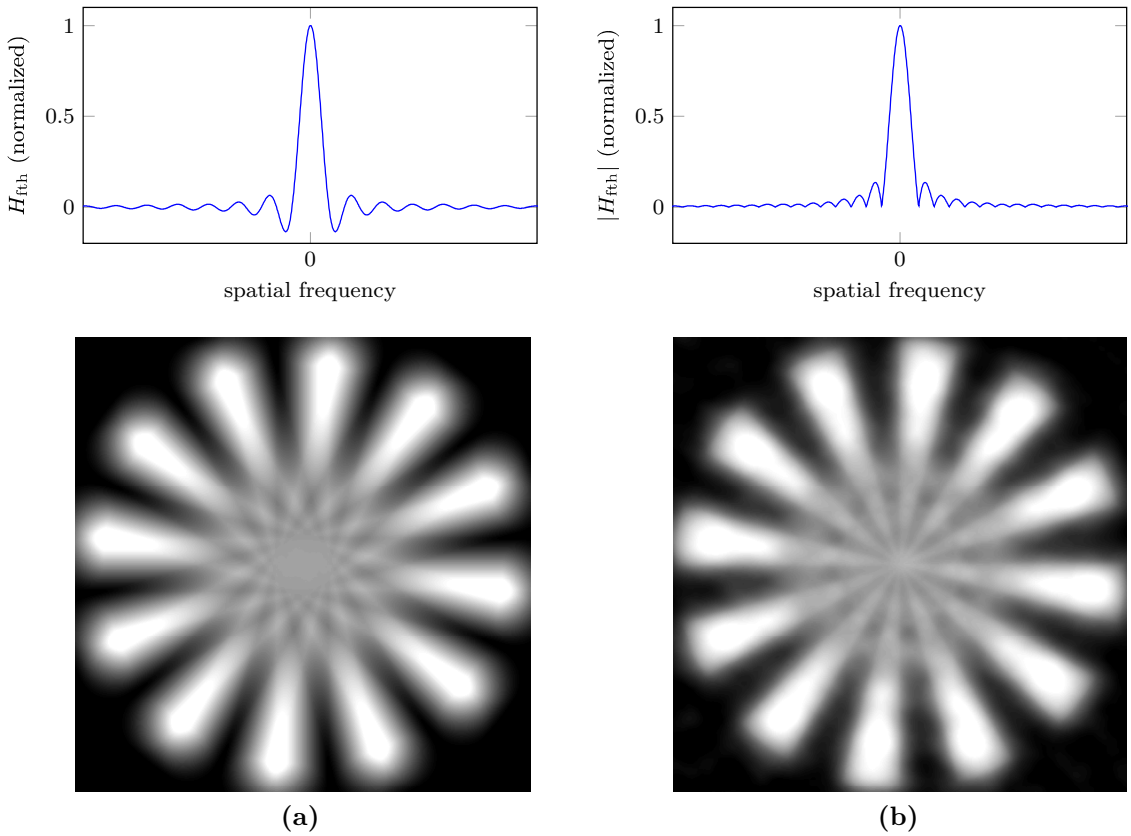

Figure 3.19: Resolution enhancement by modifying the FTH transfer function H_{fth}. (a) Transfer function and simulated reconstruction of a sector star test pattern. The center shows an inverse contrast at frequencies that correspond to the negative contributions of the transfer function. (b) The same reconstruction with a non-negative transfer function. Spatial frequency bands within the hologram that correspond to negative values of the transfer function are multiplied by minus one. The reconstruction shows very weak contrast at the periods corresponding to the zero positions of the transfer function

Experimental verification

In order to verify the results of the simulations, a simple FTH experiment with soft X-rays was carried out at BESSY II beamline U41-PGM. The sample consists of a sector star which was fabricated by focused ion beam (FIB) lithography into a 1 µm thick gold film on a silicon nitride membrane. The sector star has a diameter of 5.27 µm and consists of 24 zones, i.e., the outermost sector star period is 1.38 µm. In order to investigate the effects of reference limited FTH, a reference pinhole with a diameter of 370 nm was milled into the metal mask at a distance of 12 µm from the center of the sector star. Fig 3.20 (a) shows the integrated mask test sample.

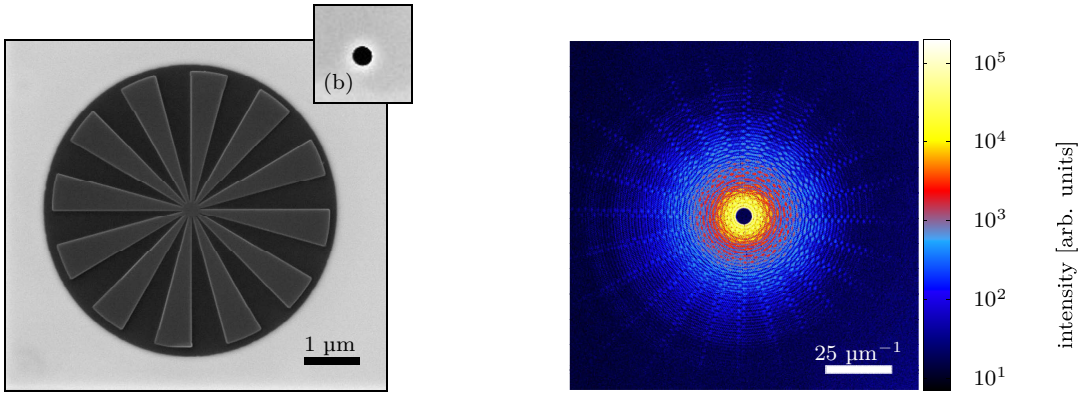

(a) (c)

Figure 3.20: Scanning electron micrograph of a sector star test sample. (a) The sector star was milled into a 1 µm thick gold film utilizing a focused ion beam. The sector star has a outer period of 1.38 µm and a diameter of 5.27 µm.(b) The reference pinhole is fabricated into the same metal film at a distance of 12 µm from the sector star center. The reference diameter is 370 nm. (c) Diffraction pattern in logarithmic intensity scale.

For the experiment, the mask was illuminated with coherent light of $E = 400\ eV$ and the detector was placed 332 mm downstream of the mask. The experimental setup yields a numerical aperture of NA $= 0.042$ and results in a diffraction limited resolution cut-off of 15.3% image contrast for $d_{\text{ang}} = 0.755\lambda/\text{NA} = 55$ nm (see Eq. (3.24)). With $R_{\text{Airy}} \approx 4$, the setup is strongly reference limited. A central beam stop was used to extend the CCD's dynamic range by blocking the intense central part of the (unscattered) beam. The beam stop effectively works as a high pass filter and shapes the propagated PSF to the more confined form described in Fig. 3.18.

Fig 3.20(b) shows the recorded diffraction pattern, depicted in logarithmic intensity scale. Fig 3.21(a-d) show the reconstruction and the sector star contrast averaged over all sectors dependent on the sector star period. The faint colors and the error bars corresponds to the threefold standard deviation of the contrast. The reconstruction of the sector star is given in the upper left of the diagrams. A zoom-in of the sector star center is presented in the lower right.

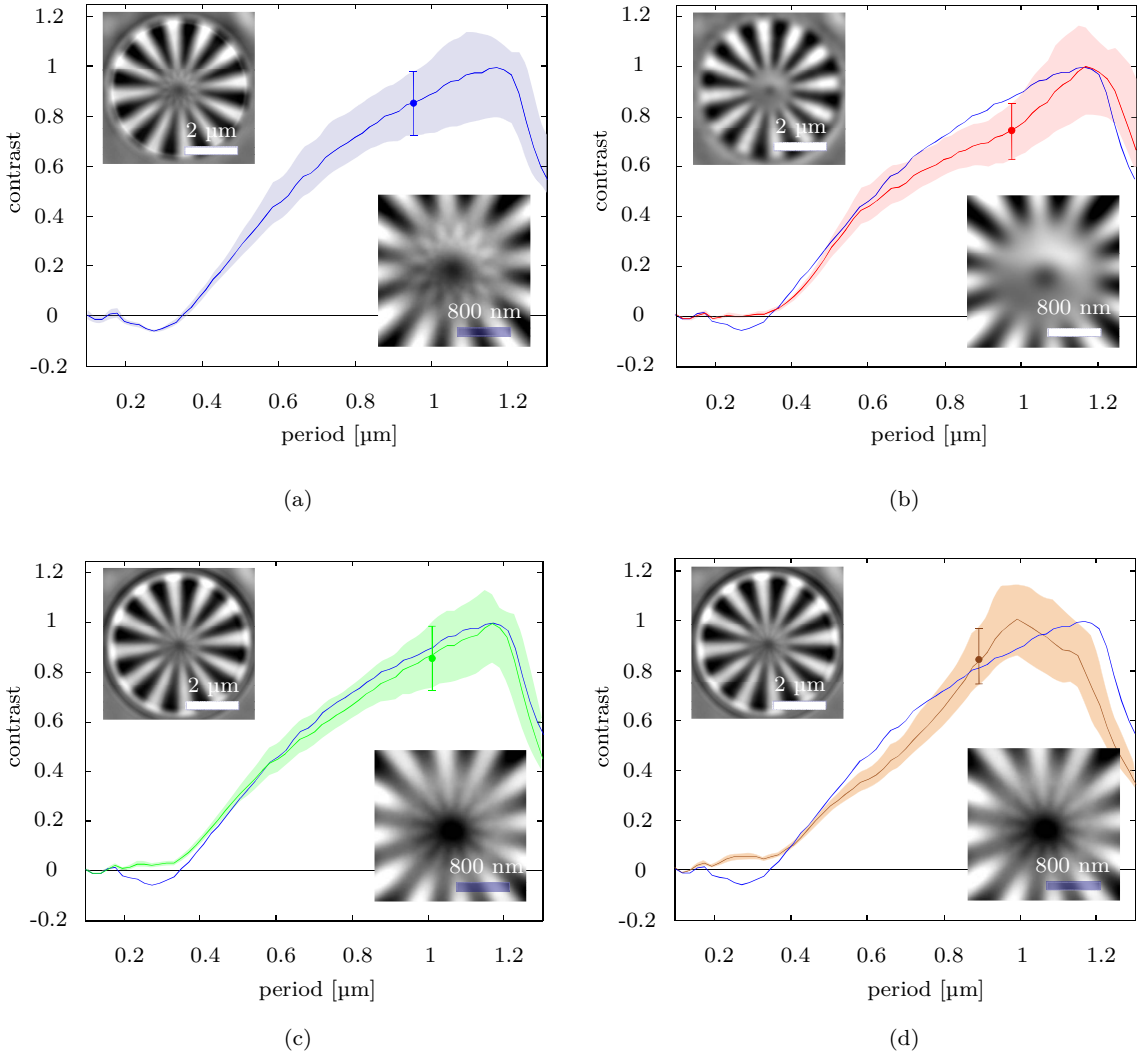

Figure 3.21: Resolution test experiment with large R_{Airy}. The reconstruction of the sector star is shown in the upper left of the diagrams. A zoom-in of the sector star center is provided in the lower right. The curves show the contrast of the sector star averaged over all sectors dependent on the corresponding period. The contrast is normalized to the maximum value. The faint colored areas and the error bars correspond to the three-fold s.d. of the contrast. (a) Untreated reconstruction in the mask plane. The center of the sector star appears inverted. (b) Low pass filtered reconstruction obtained by erasing all pixels in the hologram with radii larger than the reference Airy disks first minimum. The previously inverted center of the sector star is now blurred while the resolution limit is not significantly affected. (c) Reconstruction after propagating the unfiltered reconstruction by $l_{\mathrm{prop}} = 16$ µm. (d) Reconstruction with non-negative transfer function H_{fth}. Pixels in the hologram that correspond to negative frequencies in the reconstruction were multiplied by minus one. In panel (c) and (d), the center of the reconstruction is not inverted and resembles the sector original star pattern.

The initial reconstruction upon Fourier transforming the hologram (Fig 3.21(a)) shows the contrast inversion described above in the center of the sector star with maximum inverse contrast at a spatial period of $p = 270$ nm. For larger periods p, the contrast increases (i.e., decreases in magnitude) and reaches zero for $p = 350$ nm. For $p = 420$ nm the contrast reaches 15.3%. At the outer parts of the sector star where $p > 2d_{\mathrm{ref}}$ the contrast saturates.

Fig 3.21(b) shows the reconstruction after low-pass filtering by multiplying all pixels of the hologram with $r_{\mathrm{cut}} > 1.22 z_o \lambda / d_{\mathrm{ref}}$ by zero. Contrary to the initial reconstruction (blue), the filtered hologram shows a diminishing contrast (red) towards the center of the sector star without any contrast inversion. The 15.3% contrast resolution criteria is reached at $p = 440$ nm and does not deviate significantly from the unfiltered reconstruction.

The contrast inversion can also be precluded if the reconstructed wave field is propagated by 16 µm (Fig 3.21(c)). The propagation distance was found by visual inspection of the sector star. The theoretical value for the propagation distance with $d_{\mathrm{ref}} = 370$ nm is $l_{\mathrm{prop}} = d_{\mathrm{ref}}^2 / 4\lambda = 11$ µm. Instead of the inverse contrast artifact, the center of the test pattern now reproduces the sectors (green). Since the contrast in the center of the sector star is faint, the 15.3% contrast criterion is not significantly shifted towards smaller periods.

Panel (d) of Fig 3.21 shows the reconstruction for a non-negative transfer function. The zeros of the contrast curve in panel (a) where utilized to locate the negative sidelobe of the transfer function P_{fth}. The hologram was multiplied with minus one at locations that correspond to this negative side lobe. The contrast in the center is slightly better compared to the propagated reconstruction.

3.5 Conclusion

Based on the evaluations in this chapter it can be summarized that an FTH setup should ideally be adjusted such that the diameter of the central Airy disk of the reference pinhole matches the detector side length ($R_{\mathrm{Airy}} = 1$). Smaller references d_{ref} with $R_{\mathrm{Airy}} < 1$ unnecessarily decrease the reference signal and do not pay off with higher resolution. For nearly diffraction limited imaging ($R_{\mathrm{Airy}} \ll 1$) the resolution cut-off defined by the separation between two points that yields 15.3% image contrast of the reconstructed amplitude is $0.755\lambda/\mathrm{NA}$ (Eq. (3.24)). Apart from drastically decreased photon efficiency of such a configuration, it is also disadvantageous that the transfer function H_{fth} of the diffraction limited setup is not circular symmetric and has sharp boundaries. Depending on the application, the recorded hologram might need to be multiplied by a window function – which essentially is a low pass filter – to suppress ringing artifacts of strong scattering specimen.

For strongly reference limited setups ($R_{\mathrm{Airy}} \gg 1$), the resolution limit is equal to the diameter of the reference pinhole. Feature sizes below this resolution limit potentially result in imaging artifacts. The reconstruction in the plane of the reference ($l_{\mathrm{prop}} = 0$) does not match the plane of least confusion. For setups with $R_{\mathrm{Airy}} \geq 1$, it is thus advantageous

to filter the reconstruction by multiplying all pixels in the hologram with $\boldsymbol{r}_{\mathrm{ccd}} > 1.22 z_o \lambda d_{\mathrm{ref}}$ by zero to circumvent imaging artifacts and to shape of the reference beam along the optical axis into the common form with a single plane of least confusion. While such filtering seems to be reasonable especially for scattering signals with large diffraction angles, it does not show negatives effects in the simulations or in the experiment carried out in chapter 3.4.3. The central Airy disk of such a filtered hologram serves thereby as a naturally apodized window function, which suppresses ringing artifacts [Goo96]. The two-point resolution limit for such filtered holograms which yields 15.3% image contrast is $d_{\mathrm{fth}} = 0.93 d_{\mathrm{ref}}$. The image quality might be further improvable for experiments where an intensity reconstruction can be considered, i.e., holograms of amplitude modulating specimen without central beam stop shadow. For such experiments, the modulus of all pixels in the reconstruction of a complete hologram without central beam stop shadow can be squared to suppress ringing artifacts and improve the contrast of small features.

The resolution limit of strongly reference limited holograms with $R_{\mathrm{Airy}} \gtrapprox 2$ can potentially be improved by a factor of approximately 2.5 (cf. Fig. 3.19(b)) if the reconstruction is numerically propagated by $l_{\mathrm{prop}} = \pm d_{\mathrm{ref}}^2 / 4\lambda$. For this reason, the reference pinhole diameter can theoretically by increased by a factor of $\Delta_d = 2.5$ ($R_{\mathrm{Airy}} = 2.5$) without sacrificing resolution compared to the proposed configuration of $R_{\mathrm{Airy}} = 1$. However, such a strategy is disputable for the following reason. If the pinhole is regarded as a single zone FZP and by implying a first order diffraction efficiency equally good as for FZPs with many zones ($\eta = \pi^{-2}$) [Att07], the reference signal strength in a particular beam waist can be expected to deviate by factor of $\Delta_d^2 / 4\pi \approx 0.5$ from the configuration with $R_{\mathrm{Airy}} = 1$. Even if both beam waists are exploited for the reconstruction, the reference signal is therefore not stronger compared to the configuration with $R_{\mathrm{Airy}} = 1$. In order to reach a certain resolution limit, it is therefore not beneficial to intentionally plan a strongly reference limited FTH setup with $R_{\mathrm{Airy}} \gtrapprox 2$ in order to improve the resolution by propagation. Apart from the photon efficiency, another disadvantage of this configuration is the more complex reconstruction algorithm which potentially necessitates the removal of the defocused contribution from the opposite beam waist that superpose the reconstruction.

Enhancing the resolution of reference limited holograms with $R_{\mathrm{Airy}} > 1$ can be accomplished if the transfer function H_{fth} is known. A simple approach relies on the knowledge of the zeros of the transfer function H_{fth} and precludes imaging artifacts. The zeros of the transfer function can thereby be measured by utilizing a sector star test pattern which is fabricated next to the object to be imaged. In order to achieve efficient FTH imaging with large references, this is a promising method which can be further developed.

In addition to the theoretical motivation of these strategies to improve the spatial resolution, all concepts introduced for $R_{\mathrm{Airy}} > 1$ where verified experimentally.

4 Monolithic focused reference beam X-ray holography

One major disadvantage of conventional FTH with reference pinholes is the entanglement of the spatial resolution and contrast in the reconstruction. If the reference diameter is decreased, the resolution limit will scale linearly with the reference size while the reference signal strength, and ultimately the image contrast, is reduced quadratically. A high-resolution FTH imaging experiment is therefore commonly designed as a compromise between the desired resolution and the required reference signal. As long as the reference signal exceeds the detector's noise level, the decrease in flux through an ever smaller reference could in principle be accounted for by extending exposure times up to a certain practical limit. However, resolution limits as reported for Fresnel zone plate (FZP)-based X-ray microscopy [Cha12] have not been achieved for FTH using reference pinholes with high aspect ratio up to now. Moreover, for the growing class of dynamic studies relying on femtosecond X-ray pulses, the signal has to be collected from a limited number of photons [Cha07; Gau10; Rav09; Wan12]. It has been demonstrated that the image contrast can be improved in a monolithic approach by using multiple reference pinholes. The final image is then retrieved either by the sum of all independent reconstructions [Sch06; Sta08] or by a Hadamard convolution if the references have been arranged in a so-called uniform redundant array [Mar08]. However, the number of pinholes required to keep the total reference beam intensity constant while decreasing the pinhole diameters scales with the inverse square of the spatial resolution. At the same time, the space available for the object-reference arrangement shrinks according to the detector specifications [Pfa10]. With present-day nanofabrication tools, the density of pinholes is insufficient to prepare an adequate number of such reference holes in sub-10 nm spatial resolution-imaging experiments. To avoid the dilemma of entanglement between resolution and contrast in the object reconstruction, the reference beam cannot be provided by pinhole apertures.†

Following the original idea of holography as proposed by Denis Gabor [Gab48], we have replaced the pinhole aperture by an X-ray lens, realized by a FZP. The flux in the FZP focus, that is, the intensity integrated over the size of the focus, which determines the contrast in the image reconstruction, is proportional to the FZP's diameter D, whereas the focal spot size is defined by the outermost zone width Δr (ref. [Att07]). The FZP diameter D can easily be adjusted by altering the number of zones N such that ideally the flux through the FZP approximates the flux through the object. For conventional lens-based imaging techniques like X-ray microscopy, the small focal length f of high-resolution FZPs complicates sample positioning and limits the space available for additional instruments in

the vicinity of the sample. Similar to conventional soft-X-ray FTH [Eis04], and contrary to previous off-axis and in-line holography experiments employing FZPs [Gor11; Hei11; Mal13; McN92] we have fabricated the FZP directly into the integrated sample-mask structure, retaining the mechanical stability and flexibility with regard to sample environments of the FTH set-up. Particularly with respect to application scenarios at modern femtosecond X-ray sources such as high harmonic generation and free-electron laser sources, our method overcomes crucial limitations of previous implementations. First, our method is fully compatible with time-resolved optical pumping experiments as the reference FZP does not occupy the vicinity upstream of the sample and, second, owing to the monolithically integrated design, the resolution is not affected by pointing instabilities that are common at those sources [Mal13]. The high stability of our implementation allows for very long integration times over many thousand X-ray pulses as required at photon-limited sources like high harmonic generation to achieve high spatial resolution.†

4.1 Focused reference beam concept

For the integrated mask design, the FZP focal length can be chosen as a free parameter (since no mechanical restrictions need to be considered), facilitating the flexible adjustment of the remaining FZP parameters. In contrast to conventional FTH reconstructions, which yield a focused image of the object exit wave in the mask plane, the reconstruction of the FZP-generated hologram describes the object exit wave field in the FZP focal planes, as sketched in Fig. 4.1. The geometric separation of the FZP focus and the specimen along the optical axis can be accounted for by numerically propagating the reconstructed object wave from the focal plane to the sample plane [Goo96; Gue10; Pag06]. A binary FZP focuses up to 10% of the transmitted light into each first-order focus at a focal distance $\pm f$ (ref. [Att07]) and significant further efficiency increase is possible in more refined FZP schemes. The remaining light is either transmitted unperturbed (zeroth order) or focused at smaller focal distances f/n (where n is the FZP diffraction order that can take any odd positive or negative integer value). In our holographic imaging scheme, all FZP foci give rise to independent (defocused) images and by using the appropriate numerical propagation length ($p = -f/n$) each image can be brought into focus. The desired image is obtained as the cross-correlation between the specimen exit wave and the FZP focus beam profile. Depending on the propagation direction, the obtained image originates either from the real ($n > 0$) or the virtual focal plane ($n < 0$). Focused images related to different foci can be added together to further improve the signal-to-noise ratio. For an ideal binary FZP, the reference signal therefore approaches 25% of the flux incident on the FZP if many diffraction orders are considered for the reconstruction. In this case, the efficiency even approximates that of a perfect lens if FZPs with phase-shifting zones are utilized [Kir74]. †

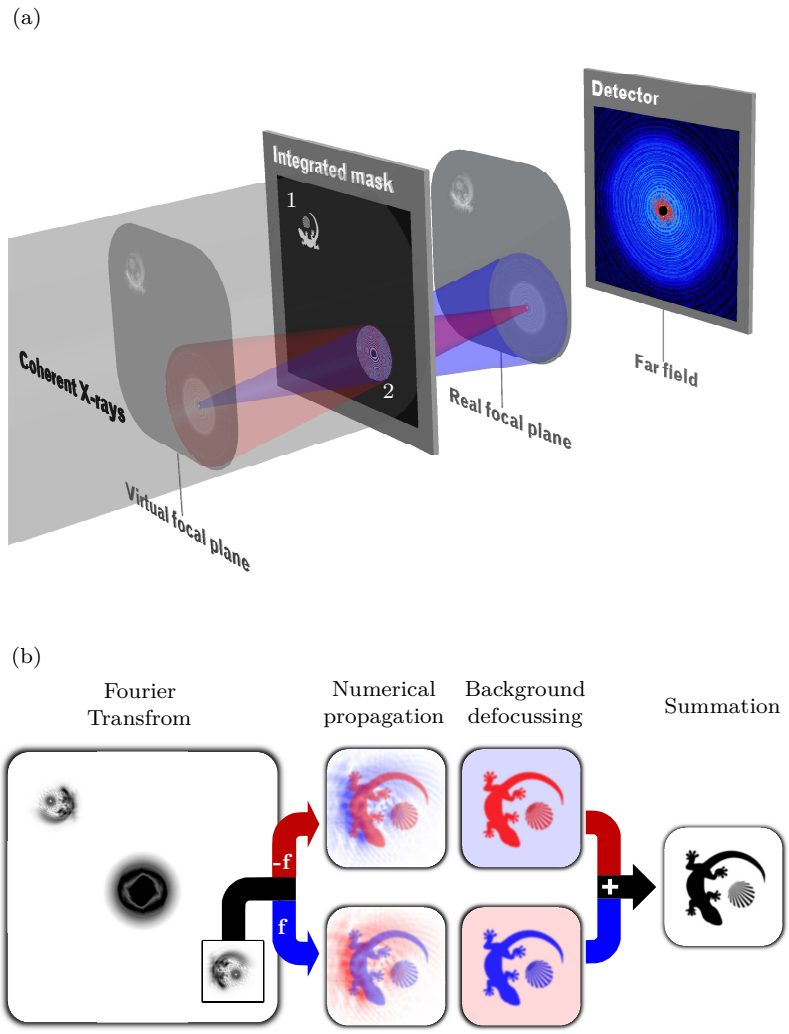

Figure 4.1: (a) Experimental geometry and imaging scheme for FTH with the FZP first-order foci. The integrated mask contains both the object (1) to be imaged as well as a FZP (2). Positive and negative FZP diffraction orders are focused in a real and a virtual focal plane, respectively. The reference beams corresponding to these focal planes encode the phase information of the object beam by interference. In each focal plane, the object exit wave appears to be defocused by the FZP focal length f. (b) The Fourier transform of the recorded hologram is depicted on the left side, containing a defocused holographic object reconstruction (black box). A focused reconstruction can be obtained by numerically propagating the defocused reconstruction by $\pm f$, yielding an in-focus image that is superimposed by the reconstruction of the opposite focal plane (middle). After defocusing the undesired opposite focal-plane contributions for both FZP diffraction orders, virtual and real-image reconstructions can be added to further improve the signal (right) †

In contrast to FZP-based full-field imaging, our method capitalizes exclusively on the FZP focal spot generated on-axis. Off-axis aberrations such as astigmatism and field curvature observed for FZPs with a low number of zones [You72] do not have to be considered. We can therefore use simple and disposable FZPs with very few zones, which make our method particularly suitable for destructive single-shot studies at free-electron laser facilities. Note that a correction of the hologram distortion due to a flat area detector may have to be considered for high scattering angles [Sch13].†

4.1.1 Image reconstruction

In the following, we describe our method on the basis of a first-order reconstruction as illustrated in Fig. 4.2. The numerical propagation of the initial reconstruction (R) from the real focal plane ($n = 1$) back to the mask plane ($p = -f$) yields the desired focused object reconstruction, which is superimposed by the cross-correlations of the remaining defocused FZP orders with the object. The intense zero-order offset can be eliminated by a central beam block, effectively acting as a high-pass filter, which is widely used in diffractive imaging experiments to protect the charge-coupled device (CCD) or to sense small signals at high diffraction angles without saturating the detector in the centre. Attention should be drawn to the contribution of the reconstructions related to the remaining unfocused FZP diffraction orders $n \neq 0$, in particular the contribution from the virtual FZP focus ($n = -1$). A similar problem is well known from in-line holography as the twin-image problem and several solutions have been proposed [Bra51; Bry68; Lat07; McE08].†

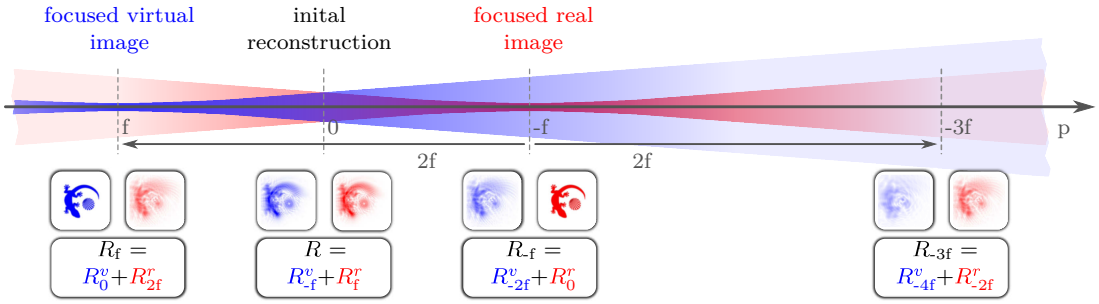

Figure 4.2: The superposed virtual image contribution (R^v_{-2f}) in the first-order reconstruction (R_{-f}) can be gradually defocused by subtracting equivalently defocused real-image reconstructions at different propagation distances p. Note that the propagated (cumulative) reconstructions (R_p) are indexed by the applied propagation distance p, while the individual contributions from the real image and virtual image have an index according to the displacement ($R^v_{\Delta p}$) from the respective focal plane.†

Methods requiring further measurements from reference beams or additional holograms recorded at different energy or distance are unsuitable for destructive single-shot imaging. Other methods are based on segmenting and erasing undesired on-axis reconstructions in their particular focal plane and imply some prior knowledge about the sample being

investigated. Since the desired object reconstruction arises as a defocused superposition in the opposite focal plane, the erasure of the unwanted reconstruction in the respective focal plane causes a loss of desired object information and therefore results in artefacts. Here we introduce a new, few-cycle iterative method that does not require additional information about the sample or the reference beam from a priori knowledge or reference measurements, illustrated in Fig. 4.2. Considering the reconstruction ($R_{-\mathrm{f}}$) propagated to $p = -f$, the most perturbing overlay ($R^{\mathrm{v}}_{-2\mathrm{f}}$) on the focused reconstruction (R^{r}_{0}) from the $n = 1$ focus is generated in the opposite (virtual) focal plane ($n = -1$). This overlay image is defocused corresponding to a propagation distance of $-2f$. A similar $-2f$ defocused image ($R^{\mathrm{r}}_{-2\mathrm{f}}$) is part of the $R_{-3\mathrm{f}}$ reconstruction obtained by propagating the specimen wave to the threefold focal distance $p = -3f$, that is, $R_{-3\mathrm{f}} = R^{\mathrm{v}}_{-4\mathrm{f}} + R^{\mathrm{r}}_{-2\mathrm{f}}$. Therefore, the $-2f$ defocused image is removed from the $R_{-\mathrm{f}}$ reconstruction via calculation of the difference $R_{-\mathrm{f}} - R_{-3\mathrm{f}}$. This procedure gives a substantial improvement over the simple $R_{-\mathrm{f}}$ reconstruction, since the perturbing virtual image is now defocused by $-4f$ instead of $-2f$ (and has negative sign). Similarly, by adding $R_{-5\mathrm{f}}$, the virtual image is further defocused to $-6f$. Consequently, an enhanced reconstruction ($R'_{-\mathrm{f}}$) can be obtained by gradually defocusing the undesired virtual image contribution:

$$R' = R_{-\mathrm{f}} + \sum_{m=1}^{M} (-1^{m}) R_{-(1+2m)f}. \tag{4.1}$$

After a few iterations up to a certain maximum depth M, the disturbing background is sufficiently defocused and approaches a homogenous offset, that is, structure from the unwanted image is effectively removed. For contributions of higher FZP orders, this method can be repeated in a similar fashion. However, the impact of defocused higher-order superpositions in the reconstruction is much weaker since the diffraction efficiency of an ideal binary FZP drops with $n - 2$ (ref. [Att07]). In addition, the FZP focal length shortens for increasing diffraction orders, and contributions of higher orders are strongly defocused in a particular lower-order plane. We therefore restrict our attention exclusively to the first orders.†

4.2 Experimental demonstration

To demonstrate our method, we have fabricated a sample (Fig. 4.3(a)) consisting of a 40-zone FZP with an outermost zone width of 50 nm, a conventional pinhole reference aperture and a test object. The test object comprises a gecko-shaped aperture surrounding a quadrant of a Siemens sector star, which allows evaluating the resolution achieved in the reconstruction. The conventional pinhole reference has a diameter of 60 nm, rendering the pinhole reconstruction directly comparable to the FZP-based FTH image. All objects are produced on a 100-nm-thick silicon nitride (Si_3N_4) support membrane, which is coated by a 1-µm-thick gold film. In Fig. 4.3, selected object features are presented as magnifications,

including the geckos right feet (cyan, blue), an alignment hole closed by a deposited platinum dot (red) and some dirt grains (green, yellow) within the gecko object. The Pt deposit and the dirt grains are depicted from the Si_3N_4 side where they are located. The gecko feet including the toes are shown from both sides. These features are not patterned completely through the entire gold mask thickness owing to the limited aspect ratio and the finite resolution achieved in fabrication via focused ion beam (FIB).

The sector star is 4 µm in diameter, comprises 64 periods and facilitates an evaluation of smallest resolvable feature sizes from 98 nm down to 23 nm (196-46 nm period). A FIB was used to mill a reference pinhole of 60 nm diameter and the gecko-shaped aperture as well as to unmask the FZP and the sector star. The apertures were positioned with the help of small alignment holes. After alignment, all alignment markers were closed by FIB-assisted deposition of 1 µm thick Pt dots on both membrane sides. The alignment hole located within the gecko aperture was closed from the Si_3N_4 side only. In the scanning electron microscopic images in Fig. 4.3(a), the deposited dots are visible as bright squares and disks.†

4.2.1 Experimental setup

The experiment was performed at the UE52-SGM beamline of BESSY II in Berlin, Germany. The integrated mask was placed 170 mm downstream of the beamline focus and 325 mm in front of a back-illuminated, in-vacuum CCD camera (2048 x 2048 pixels) with pixels of 13.5 µm edge lengths. To increase the dynamic range of the holograms beyond the CCD limitations, a diffraction pattern recorded with a central beam stop was numerically combined with a diffraction pattern of the centre region, which was recorded by attenuating the incident X-ray beam with a gold filter of 150 nm thickness.†

4.2.2 Results

The mask is illuminated with coherent synchrotron radiation of 400 eV photon energy and the recorded hologram is presented in Fig. 4.3(b). The maximum momentum transfer recorded on the detector is 86 μm^{-1} and corresponds to a diffraction-limited resolution of 36 nm (half-period) in the reconstruction. The resolution of both pinhole and FZP reconstructions is therefore limited by the spatial extent of the reference structures. In Fig. 4.3(c) and (d), we show the second quadrant of the Fourier-transformed hologram before and after numerical propagation of $p = -1f$, respectively. To provide a uniform contrast of the different features in the overview figure, the reconstruction is high-pass filtered and depicted in logarithmic scale (amplitude).†

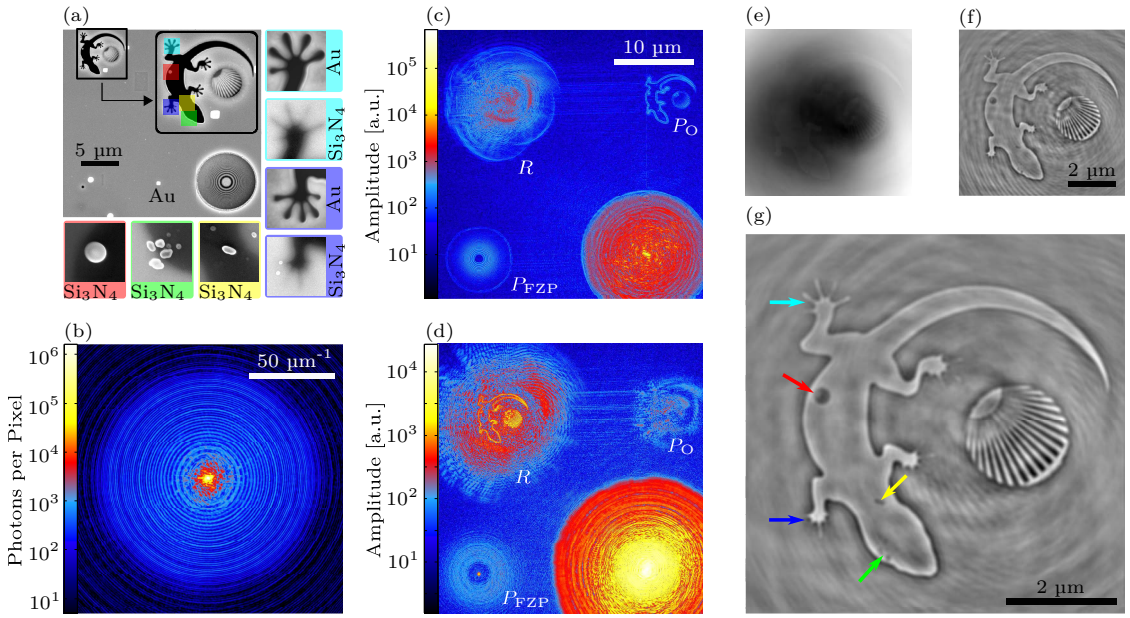

Figure 4.3: (a) Integrated mask with test object, conventional reference pinhole and FZP reference imaged by scanning electron microscopy (SEM) from the Au side of the sample (high dynamic range image to visualize features at front and back of the membrane). The bright squares and disks correspond to Pt deposits used to close alignment holes. These structures are opaque to soft X-rays. In the magnified inset (dimensions: 7x7 µm^2), selected features of the object have been marked. SEM-imaged sections of these features with a size of 1x1 µm^2 were taken from the Si_3N^4 or Au side as indicated. Scale bar, 5 µm distance. (b) Far-field X-ray diffraction pattern depicted in logarithmic intensity scale. Scale bar, 50 µm^{-1} momentum transfer. (c) High-pass filtered holographic reconstruction (logarithmic amplitude) containing the cross-correlation of FZP and test object (R), the cross-correlation of test object and reference pinhole (P_o), and the cross-correlation of reference pinhole and FZP (P_{FZP}). Scale bar, 10 µm distance. (d) Holographic reconstruction after numerical propagation by the FZP focal length. (e) Cropped reconstruction of the desired image (real part) after numerical propagation by the FZP focal length. (f) The same image after removal of the zeroth order offset by high-pass filtering. Scale bar, 2 µm distance. (g) Image reconstruction after gradual defocusing the unwanted contribution from the opposite focal plane reconstruction. The arrows point to the features that were selected from SEM images in panel a. Scale bar, 2 µm distance.†

Apart from the central autocorrelation, the Fourier transform of the hologram consists of three contributions: (R) the cross-correlation of the FZP exit wave with the exit wave from the object, emerging as a superposition of defocused images related to all FZP foci, (P_o) the cross-correlation of the exit waves of the pinhole and the object, and (P_{FZP}) the pinhole reconstruction of the FZP. After numerically propagating the wave field by the FZP first-order focal length (Fig. 4.3 (d)), P_o appears defocused while P_{FZP} shows a

bright first-order focus. The desired reconstruction R is now focused but superposed by defocused reconstructions from all other FZP foci. The propagated FZP reconstruction without high-pass filtering is enlarged in Fig. 4.3(e). The zeroth order is removed by suppressing low-frequency signals in the hologram with a Gauss function filter, and the sum of both filtered first-order reconstructions is shown in Fig. 4.3(f). The final image is retrieved after applying $M = 5$ iterations of our method to remove the associated image contribution in the opposite focal plane individually on both first-order reconstructions before summation (Fig. 4.3(g)). To demonstrate the efficiency of our method, holograms with different exposure times have been recorded, and the fully filtered FZP reconstructions are compared with the pinhole reconstructions in Fig. 4.4(a).†

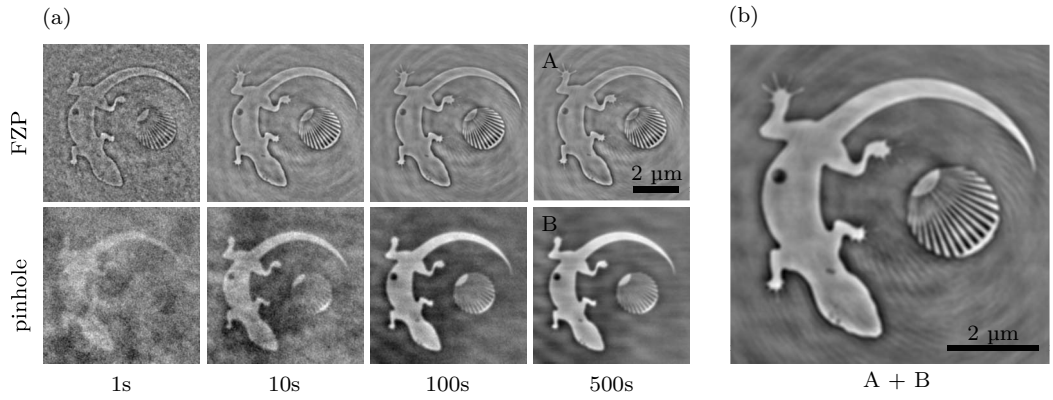

Figure 4.4: (a) The images show the reconstructions of our test object (real part) via the pinhole reference and the Fresnel zone plate (FZP) reference, obtained from the same holograms of the integrated mask (Fig. 4.3(a)) for different exposure times. Focused reference beam holographic images are reconstructed with our algorithm to remove contributions from the associated reconstruction in the opposite focal plane. The FZP reference reconstructions feature an improved signal-to-noise ratio and a higher spatial resolution. (b) Combined object reconstruction. In contrast to Fig. 4.3(g), low-frequency components of the object are now included via summation of pinhole and FZP reconstructions. Scale bars, 2 µm distance.†

4.3 Discussion

Evidently, reconstructions of the FZP feature a significantly improved signal-to-noise ratio for short exposures and a superior spatial resolution due to the small FZP focal spot. The superior resolution in FZP reconstruction is also evident at the gecko's right hind foot, which shows clearly resolved toes. Most of the other toes transmit the X-rays too faintly to be resolved. As an option, one can to some extent recover low-frequency components of the test object not present in the FZP reconstruction via a pixel-wise summation of the pinhole reconstruction containing low-frequency data and the FZP, as illustrated in Fig.

4.4(b). The resolution limit for the pinhole and the FZP reconstruction is determined by evaluating the contrast of the sector star in the centre of the test object for different radii (Fig.4.5). The Rayleigh resolution limit [Att07] is found at 124 nm full period for the pinhole (62 nm feature size) and 92 nm (46 nm feature size) for the FZP reconstruction. By using state-of-the-art FZPs with outermost zone widths approaching 10 nm [Cha12] and the possibility to utilize higher diffraction orders [Reh09; Sch97] sub-10 nm spatial resolution will become accessible on this basis in FTH.†

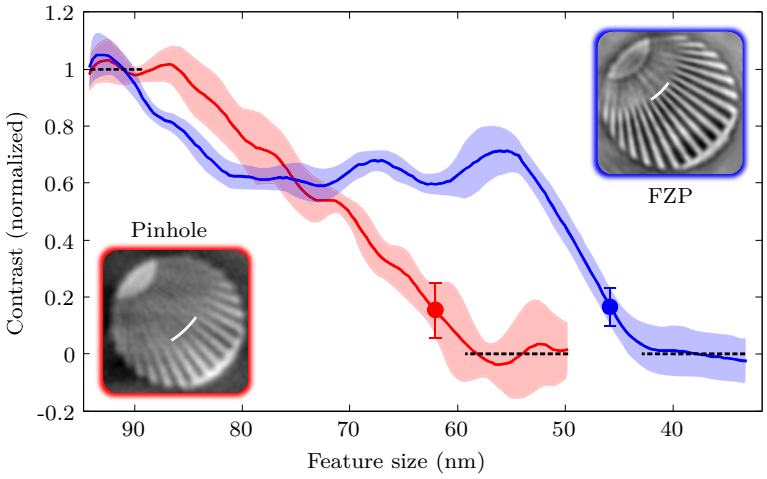

Figure 4.5: The plot shows the normalized image contrast in the sector star depending on the sector star's line width for pinhole (red) and zone plate reconstruction (blue). Since the image background is not perfectly homogenous, the contrast is determined for the four central sectors (covered by the white arc) individually. The lines show the mean image contrast, whereas minima and maxima for normalization are obtained by averaging the contrast along the dashed lines. The confidence intervals according to the onefold s.d. of the contrast in the four different sectors are indicated by error bars and by the pale-coloured areas. The smallest resolvable feature sizes according to the Rayleigh resolution limit is determined with 62 nm (124 nm period) for the pinhole and 46 nm (92 nm period) for the FZP reconstruction (indicated by the points in the plot and by white arcs in the images).†

In conclusion, monolithic focused reference beam X-ray holography enhances signal strength and resolution of FTH images even when employing rather primitive FZPs. In particular, the approach decouples the formation of image contrast from the spatial resolution. Focused reference beam X-ray holography is straightforward to implement and permits the application of easy-to-fabricate FZPs, that is, by FIB milling [Ove12]. We provide a robust algorithm to remove image artefacts arising from the diffractive nature of the FZP lens, yielding high-quality images. We note that the energy dispersion of a FZP and the resulting spatial separation of foci from distinct photon energies opens the

possibility to encode the spectral response of an object in a multi-colour experiment into a single hologram, even in a single-shot exposure. In conjunction with the possibility to holographically encode images of multiple samples [Sch06] and dynamic processes [Cha07; Gün10; Gün11], we envision the approach to enable dynamic studies on the few-nanometre level in particular at coherent X-ray sources.†

5 Extracting depth information from a single-view X-ray Fourier-transform hologram

In microscopy in general and nanoscience in particular, the extraction of depth information from three-dimensional (3D) objects of interest is often important. In optical microscopy, where numerical apertures are large, the depth-of-field can be of the same order as the lateral resolution limit and 3D objects are predominantly investigated by combining images from different focal depths [Dub99; Str85]. On the other hand, when using an X-ray probe, the depth of field is typically orders of magnitude larger than the lateral resolution limit, allowing to obtain in good approximation a projection image of a sample. A 3D reconstruction of the object can then be retrieved in a tomographic approach by utilizing a set of projection images from different angular perspectives. These 2-dimensional (2D) projection images can be obtained by different imaging methods such as X-ray full-field microscopy [Wei00], coherent diffraction imaging (CDI) [Mia02; Pfe06], ptychography [Die10] or holography [Gue12]. CDI alternatively allows reconstructing a 3D model of the specimen from a 3D reciprocal-space data set that again was composed out of many 2D diffraction patterns taken from different sample orientations [Cha06b; Loh12]. Even though tomographic methods are powerful in that they can achieve a depth resolution as high as the lateral resolution, the requirement of several exposures can be a limitation. This can for example be the case in the study of non-triggerable or non-deterministic dynamical phenomena [Cha07] such as fluctuations in thermal equilibrium or in general in situations when single-shot experiments are indicated, e.g. in order to follow a "diffract before destroy" approach for delicate samples via intense and ultrashort X-ray pulses [Cha06a; Sei10].♯

Two techniques that have proven to be compatible with femtosecond snapshot imaging at the nanometer scale are X-ray holography [Cha07; Gün11; Mar08; Pfa10] and CDI [Cha06a; Sei10]. Both imaging methods record the specimen's diffraction pattern in the far-field without any optical elements between sample and detector. When using holographic methods, the specimen's exit wave is reconstructed using the phase information encoded in the diffraction pattern by the interference of object and reference wave [Eis04; McN92; Pag06]. In the case of CDI, a solution of the phase problem is iteratively retrieved from the sample's diffraction pattern alone. In order to minimize the solution space, phase retrieval algorithms rely on certain constraint conditions which necessitate a priori information about the specimen [Cha06b; Loh12; Pfe06]. For CDI experiments, it has already been suggested that 3D structures can be determined from a single view. The 2D diffraction pattern needs to be recorded with sufficiently fine sampling and projected

on an Ewald sphere within a 3D coordinate space [Rai10]. Therefore, the reconstruction algorithm is computationally intensive and requires many iterations involving 3D Fourier transformations.♯

In contrast, the non-iterative approach demonstrated here is based on a conventional X-ray Fourier-transform holography (FTH) experiment and determines an unambiguous reconstruction by exploiting the information contained in a *single* hologram recorded on a 2D pixel detector. The holographic reconstruction of the wave field in the plane of the reference source allows to propagate the angular spectrum of the reconstructed object wave along the beam axis [Goo96; Gue10] and thereby refocus specimen features outside the depth-of-field. The finite depth-of-field resulting from the scattering geometry can be used to measure the distance between features along the beam axis as has been demonstrated for holography experiments using soft X-rays [22] and extreme ultra-violet (EUV) radiation [23,24]. In this work, the depth information is used to reconstruct a complete 3D model of a specimen. The method can be seen as an analogue to digital holographic microscopy (DHM) [2,24] as the position of different features along the optical axis (i.e. the longitudinal position) is determined by bringing the feature into focus. Similar to DHM and contrary to non-holographic methods, this information is retrieved post-experimentally from a single Fourier-transform hologram, which can hence be recorded in a single exposure if required. As specimen we use an artificial, extended 3D test structure whose longitudinal dimension exceeds the optical setup's depth-of-field. From the hologram reconstructions at different longitudinal coordinates, the displacements of the specimen features from the sample substrate are measured and transferred into a 3D model reconstruction. A suitable specimen feature is utilized to determine the transversal and longitudinal resolution. The results are compared to the theoretical prediction. ♯

5.1 Refocus method and depth measurement

In the single pinhole reference case further considered here, the image reconstruction is retrieved by a 2D spatial Fourier transformation of the recorded hologram and results in a 2D information of the amplitude and phase of the object's exit wave, i.e. one obtains the 2D, complex wavefield leaving the object. The in-focus contribution of this wavefield is obtained from the plane parallel to the detector which includes the reference source. The 2D reconstruction of a conventional Fourier-transform hologram shows optimally resolved features for the portion of the specimen that has a sufficiently small longitudinal separation from this plane of the reference source, i.e. features within the depth-of-field. However, the holographic reconstruction of the wave field in the plane of the reference source allows to propagate the angular spectrum of the reconstruction [Goo96; Pag06] along the beam axis and thereby refocus specimen features outside the depth-of-field. It has been shown that the plane of least confusion can be separated from the plane of the reference by numerically propagating the reconstructed specimen wave front according to the physical separation between both planes [Gei14b; Gue10]. Similarly, a thoroughly focused reconstruction of an

extended 3D object can be obtained by numerically propagating the reconstructed wave fronts of individual object features outside the depth-of-field into focus. Additionally, the finite depth-of-field can be used to measure the position of a particular feature along the optical axis by examining the feature's reconstruction for different propagation lengths [Mon14; Wac10]. We thus consider the depth-of-field as the longitudinal resolution limit that allows a clear distinction between features that are closely displaced along the optical axis.♯

The application of the free-space propagator requires a homogeneous wavelength throughout the object, i.e. the refractive index is assumed to be constant. For large spatial deviations of the specimen refractive index within the propagation distance, the actual wave front is distorted and might deviate significantly from the numerically retrieved reconstruction. Generally, in the X-ray regime, the refractive index is close to unity [Att07] and spatial distortions caused by an inhomogeneous refractive index within one attenuation length are expected to be much smaller than the longitudinal and lateral resolution limits.♯

In the following we assume that the geometry of the FTH experiment allows to record sufficiently large scattering angles such that the limit for the lateral spatial resolution is set by the lateral size of the reference aperture and not by the maximum momentum transfer. The phase information in the hologram is encoded by the object-reference interference and is accessible only up to scattering angles with sufficiently high fringe contrast, i.e. up to scattering angles with adequate reference and object beam intensity. For a circular reference pinhole of diameter d, illuminated by a plane wave, the intensity distribution of the reference beam in the mask plane is a circular disk with constant intensity. In the far-field, the reference beam intensity on the detector is given by the Airy pattern. Typically, image information is gathered predominantly for scattering angles within the radius of the central Airy disk, still containing sufficient intensity of the reference beam. Considering the Airy disk's first minimum as the upper limit for the definition of the system's effective numerical aperture ($\mathrm{NA}_{\mathrm{eff}} = 1.22\lambda/d$), both the lateral resolution Δr and depth-of-field are defined by the diameter of the reference pinhole. For illumination with radiation of wavelength λ, the modulus of the depth of field ($\Delta z = \pm\lambda/2\mathrm{NA}^2$) [Att07] can be assessed by substituting NA with $\mathrm{NA}_{\mathrm{eff}}$:

$$|\Delta z| > \frac{1}{2\lambda}\left(\frac{d}{1.22}\right)^2. \tag{5.1}$$

Remarkably, in the case of reference-limited FTH, the lateral resolution only depends on the size of the reference aperture ($\Delta r = d$) while the depth-resolution additionally depends on the wavelength of the illumination and improves for larger wavelengths. This at first sight counterintuitive effect is the result of the increasing divergence of the reference beam with increasing wavelength. Please note, that relation (5.1) represents the lower boundary of the depth-of-field given by the first minimum (with zero intensity) of the diverging reference beam. For real detection systems affected by noise and limited photon statistics, the maximum detected scattering angle with sufficient signal-to-noise ratio and

the corresponding $\mathrm{NA}_{\mathrm{eff}}$ will be smaller resulting in a larger depth-of-field than the given boundary. ♯

5.1.1 Error estimation for biological applications in the water window

For soft X-ray energies, the absorption is generally strong and the refractive index is close to unity [Att07]. Deviations of the numerically anticipated wavefront from the actual truth for propagation distances up to one absorption length can therefore expected to be small.

Fig. 5.1 shows an estimation of the maximum error expectable due to an inhomogeneous refractive index (real part) for FTH in the water window. Biological imaging in the water window is one application where deviations of the refractive index potentially play a role. A simple model of a biological cell with inhomogeneous refractive index is a water body that consists of gas bubbles. The refractive index (real part) of the gas bubble is approximated by $n_1 = 1$. For the evaluation only the real part of the refractive index of water $n_2 < 1$ is taken into account. Fig. 5.1(a) shows the scenario for an error in z-direction. Here, the free space propagator is utilized under the assumption of a homogenous refractive index of n_1. The wavelength within the medium of refractive index n_2 however is slightly larger than the wavelength for n_1. The numerically retrieved wavefront is found for propagation distance that deviates by e_z from the real conditions.

Apart from the propagation error in z direction, also the numerically propagated wave front in the image might be distorted. Fig. 5.1(b) shows the scenario for a laterally distorted wavefront. Here, only a part of the wave travels through a different refractive index. The numerically retrieved wavefront deviates from the real wave front which is refracted at the interfaces between both mediums. Panel (c) shows an estimation of the maximum error along the beam ($|\hat{e}_z|$) and in the xy-plane ($|\hat{e}_r|$) relative to the corresponding resolution limits. The resolution limits are typical values for a high resolution FTH setup with a reference diameter $d_{\mathrm{ref}} = 50$ nm. Assuming a large detector, the lateral resolution limit will be the pinhole diameter whereas the longitudinal resolution is set by the reference limited depth of field $\Delta z = \pm 0.5\lambda^{-1}(d/1.22)^2$ (Eq. (5.1)). For this chart, the maximum longitudinal error is evaluated by calculating $\Delta\lambda = |\lambda_1 - n_1\lambda_2/n_2|$. The result is extrapolated to the propagation distance, i.e., one attenuation length.

The maximum lateral error depends on the deviation of the incoming wave front's angle caused by refraction. Therefore, the lateral error increases for larger α_1 and the estimation needs to based on the largest diffraction angle in the reconstruction. For the reference limited setup, the largest diffraction angle is assumed to be set by the pinhole reference $\alpha_1 = \mathrm{asin}(1.22\lambda/d_{ref})$. For the estimation of the maximum lateral error, the wave front is expected to travel one attenuation length after refraction.

The results show that the longitudinal and lateral errors within one attenuation length in the water window are much smaller than the corresponding resolution limits. The attenuation length of water dependent on the energy as shown by the green curve corresponds to the right vertical axis of the chart whereas the relative errors correspond to the left axis.

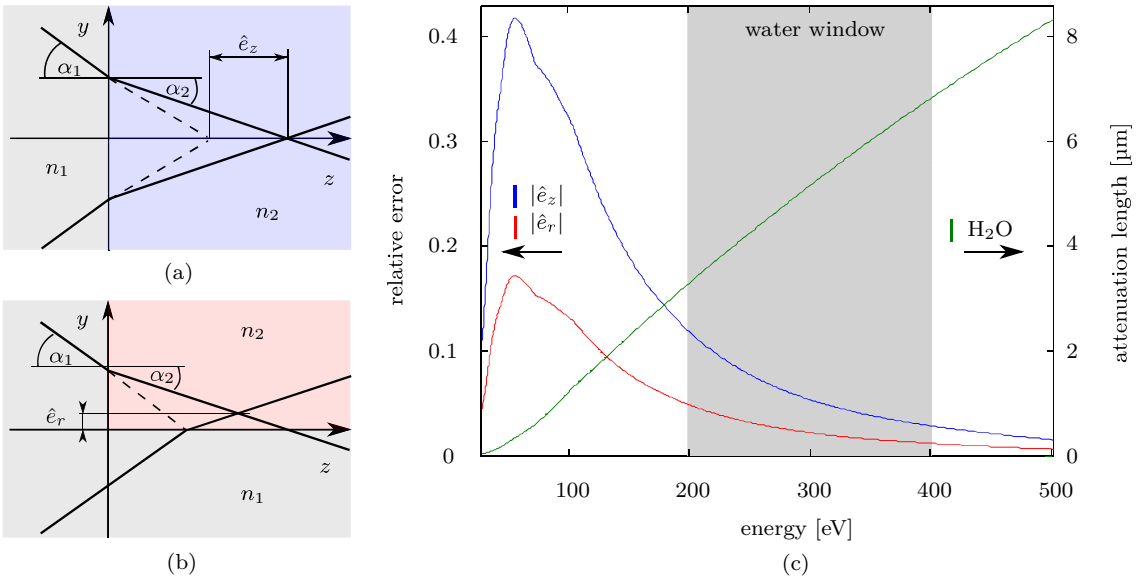

Figure 5.1: Estimation of the deviation of the numerically propagated wavefront from the true wavefront for photon energies around the water window. (a) Scenario for a longitudinal deviation. The medium with refractive index n_1 is optically more dense compared to n_2. The numerically retrieved solution converges for smaller propagation distances compared to the true wavefront. (b) Scenario for an lateral deviation. Only one part of the wave travels through a medium with different refractive index. The numerically predicted wavefront converges on the optical axis while the true wavefront converges off-axis. (c) Estimation of the maximum longitudinal (blue) and lateral (red) propagation error dependent on the photon energy within one attenuation length in water (left axis). The attenuation length in water is shown with the green curve which corresponds to the right axis.

5.1.2 Sample design

The 3D test object was produced together with the holographic mask on a 350 nm thick silicon nitride membrane coated with a 1.3 µm gold film. In a first step, an object aperture of 4.4 µm in diameter was milled into the metal film utilizing a focused ion beam (FIB). Subsequently, the reference pinhole was produced at a distance of 10 µm from the centre of the object aperture with an exit diameter of 80 nm. The actual test structure was fabricated by FIB-assisted deposition of platinum (Fig. 5.2). The sample includes a diagonal ramp that extends over the object aperture and a group of five differently shaped bodies deposited within the object aperture on the silicon nitride substrate. The ramp is 1.1 µm wide and has an inclination angle of 45° relative to the substrate. Apertures of different shape were milled into the ramp corresponding to four different elevations above the substrate.♯

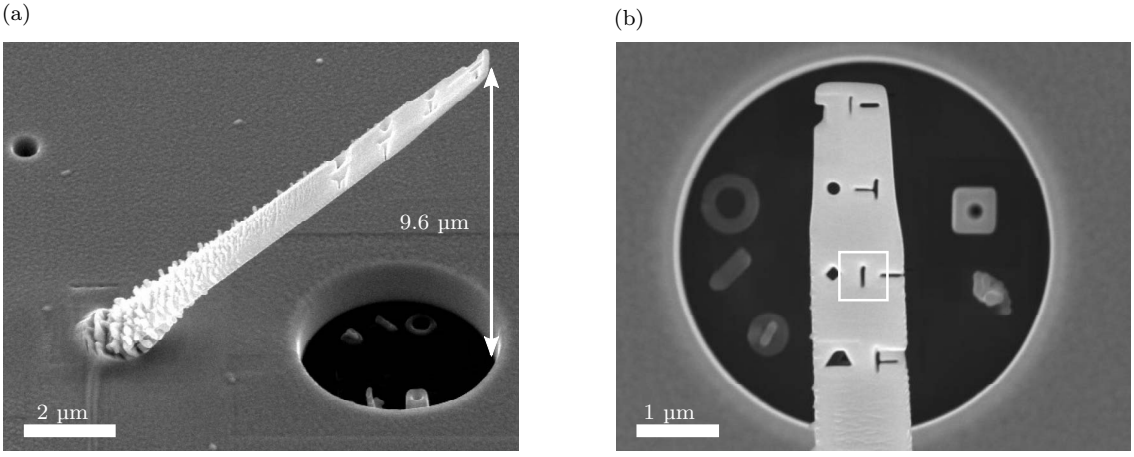

Figure 5.2: Scanning electron microscopy images of the test sample made of 3D platinum structures. The side view of the sample (a) shows the structured ramp which extends above the object hole. The ramp is deposited with 45° inclination on a gold mask. The small pinhole seen on the upper left represents the reference source, while the large circular aperture seen at the bottom right constitutes the object aperture. The top view (b) shows different platinum structures deposited on the silicon nitride membrane on a Si_3N_4 membrane at the bottom of the object aperture. Corresponding to four equidistant height levels, differently shaped marker apertures have been milled into the ramp. The width of the vertical slit in the centre of the white box is measured to 43 ± 7 nm.

5.2 Experimental demonstration

The masked-based FTH experiment was performed at the undulator beamline U41-PGM at the BESSY II synchrotron source, in a configuration described in Ref [Eis04]. The sample was placed 220 mm upstream of a back-illuminated charge-coupled device (CCD) with 2048 x 2048 pixels (pixel size 13.5 µm). Soft X-rays with a photon energy of 400 eV corresponding to a wavelength of $\lambda = 3.1$ nm were used to illuminate the sample. The hologram was recorded by accumulating 200 frames with 250 ms exposure time each. In this configuration we expect a lower boundary for the depth of field of $|\Delta z| > 693$ nm in the reconstruction. The direct beam was blocked by a circular beamstop to reduce the dynamic range of the scattering signal to the technical capabilities of the CCD detector. The missing intensity at low scattering angles corresponds to high-pass filtering of the hologram. In addition to the first measurement, the centre of the diffraction pattern was recorded in a second exposure without beamstop, but using a 150 nm thick gold filter to attenuate the beam. In order to decrease the CCD readout time, the region of interest was limited to a 200 × 200 pixel matrix which was centred in the hologram. The centre was recorded by accumulating 1000 frames with 0.9 s exposure time each. In the final single-view hologram, both exposures where patched together after matching the intensities in the overlap region. The patched hologram shown in 5.3(b) was reconstructed

by a 2D Fourier transformation after zero-padding the hologram to 4096 x 4096 pixels. The focus was shifted along the beam axis by applying the free space propagator to the reconstruction as described in Refs. [Goo96; Pag06].♯

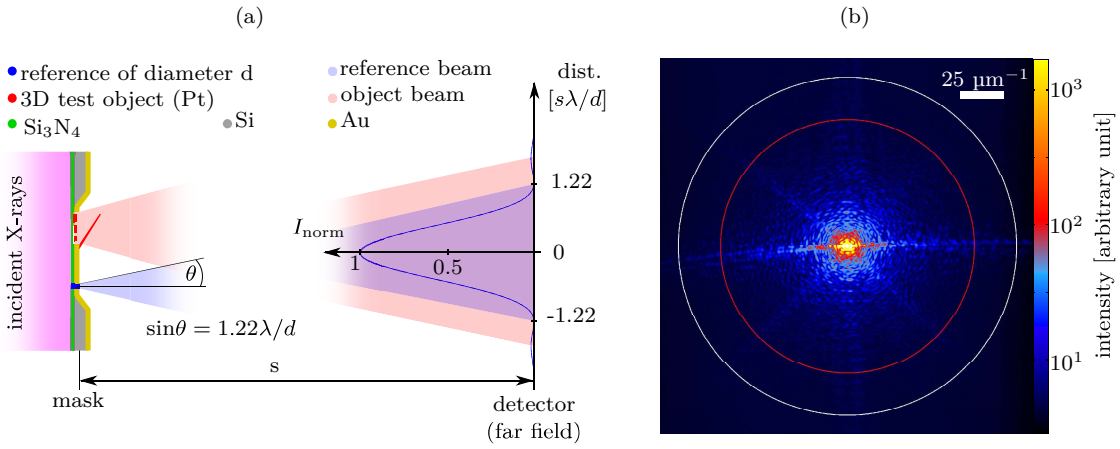

Figure 5.3: Fourier-transform holography experiment. (a) Scheme of FTH setup. With a coherent X-ray beam incident from the left side, the holographic mask defines a reference wave and the object illumination. The blue curve on the right side corresponds to the far field as recorded on the detector and shows the normalized intensity (I_{norm}) profile of the phase encoding reference beam which originates from the small pinhole of diameter d in the mask plane. (b) Coherent diffraction pattern from the 3D test structure in Fig. 5.2 constituting a Fourier transform hologram, recorded with soft X-rays with $\lambda = 3.1$ nm. The intensity is plotted in logarithmic scale. The white circle has a radius of $q_{\mathrm{zero}} = 96$ µm^{-1} momentum transfer and corresponds to the first minimum of Airy pattern of the reference pinhole. The evaluation of depth-of-field and smallest resolved spot size in the reconstruction relies on a small real space feature that corresponds to a momentum transfer of qmax = 73 µm^{-1} indicated by the red circle.

5.3 Results

Figure 5.4(a) shows the reconstruction of the patched hologram without application of the free space propagator. By default, the focus is in the plane of the reference-wave source, i.e. in the mask plane. This initial reconstruction, hence, corresponds to a zero propagation length. As seen in Fig. 5.4(a), features on the bottom of the object hole (marked by arrows) are reproduced without defocus blurring while the ramp is out of focus. Depending on the longitudinal separation from mask plane, the ramp shows ever more pronounced diffraction fringes towards the top. At the photon energy utilized for illumination, the object shows strong absorption without significant phase shift. For a numeric identification of the refocus distance of a particular feature from the mask plane, suitable focus criteria thus rely on an analysis of the reconstructed amplitudes [Che09;

Dub06; Gil89]. Numerically indentifying the optimal focus is especially promising for a single extended focal plane with many features [Dub06; Gil89], or for small objects that are well separated [Che09]. In our reconstruction a numerical focussing was hampered by two aspects: (i) For extended features that are permeating different focal planes (the platinum ramp), the common numeric approaches would rely only on a limited amount of pixels that can be brought into focus at a time. (ii) The in-focus part of the specimen is often superimposed by fringes of nearby features of a different focal plane. Additionally, Fourier transform holograms are often high-pass filtered via use of a central beam block (in contrast to this work). In these cases, edge ringing is amplified in the reconstruction of high-pass filtered holograms and a numeric evaluation is even more challenging. On the other hand, the optimal propagation length can conveniently be determined by a visual inspection of the reconstruction.

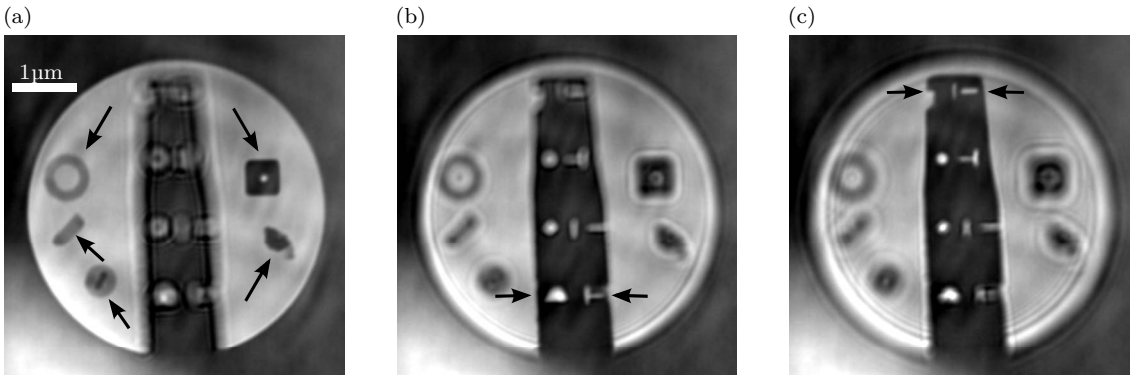

Figure 5.4: Real part of the reconstructed object wave field corresponding to different longitudinal displacements from the substrate. Reconstruction (a) corresponds to the mask plane whereas (b) and (c) are retrieved after numerically propagating the reconstructed wave field upstream by 6 µm and 9 µm, respectively. Focused features are indicated by black arrows.

By observing the reconstruction for different propagation lengths, fringes of defocused edges are seen to converge for the propagation distance approaching the separation between the particular feature and the mask plane. It is thus possible to reliably find the optimal propagation length of sharp features without any a priori knowledge. For the evaluation of the recorded hologram data, the visual approach delivered results that were superior over numeric methods relying on an analysis of the variance [Ma04], modulus [Dub06] or entropy [Gil89] of the reconstructed amplitude.

In Fig. 5.4(b) we present the reconstructed wave field after numerically propagating the initial reconstruction 6 µm upstream. This distance corresponds to a separation from the mask plane that shifts the lower part of the ramp into focus. As a result, the height markers on the low side of the ramp are in focus and clearly resolved while features at the bottom of the object hole and at the top of the ramp are defocused. The associated propagation length was found by minimizing fringes around the features of interest. The

tip of the ramp including the markers located at this position can be brought into focus by propagating the initial reconstruction 9 µm upstream (Fig. 5.4(c)). This value is in agreement with the total longitudinal extent of our sample as determined via scanning electron microscopy.♯

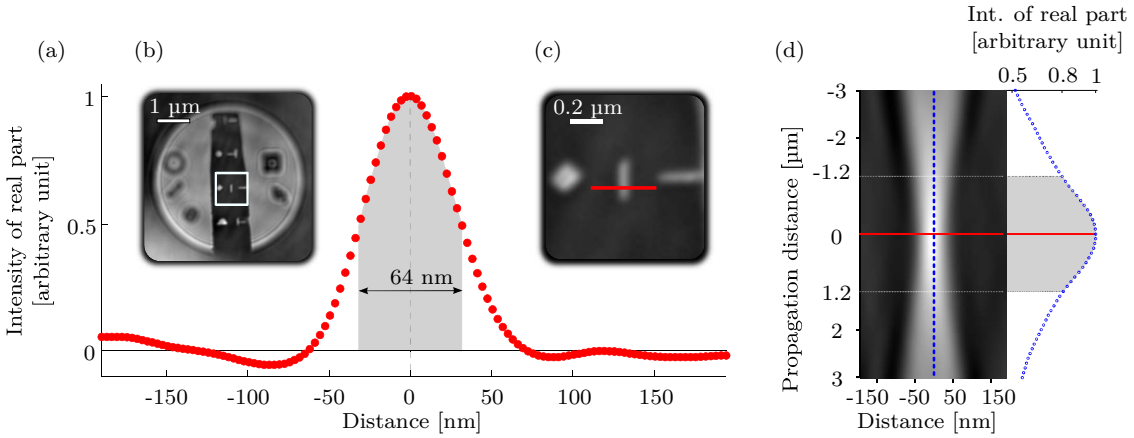

Figure 5.5: Determination of lateral and longitudinal resolution limits in the reconstruction. The line scan (a) is obtained in the region indicated by the white box in (b) and evaluates the reconstructed exit wave associated with the fine slit as marked in the close-up image (c). For the same line, this procedure was repeated as a function of longitudinal propagation distance to determine the depth-of-field, the result is compiled in (d) along the dashed blue line, the intensity of the real part decreases by 20% after propagating by 1.2 µm. For the resolution determination the sampling in the reconstruction was increased by a factor of 8 via zero-padding the original hologram prior to Fourier transformation.

The lateral resolution and the depth-of-field of the reconstruction were evaluated in a certain region of interest (ROI) on the ramp indicated by the white box in Fig. 5.5 (b). Features in the 1 µm × 1 µm ROI as magnified in Fig. 5.5 (c) are focused at a propagation distance of 7 µm. The lateral resolution was determined by evaluating the pixels indicated by a red line through the fine central slit. In the scanning electron micrograph, the width of the slit was measured to 43 ± 7 nm. Figure 5.5 (a) shows the normalized values (real part) of the corresponding pixels in the reconstruction. The smallest reconstructed feature size in lateral direction, corresponding to the full width at half maximum (FWHM) as determined from Fig. 5.5 (a) is 64 nm. In the reconstruction, the measured feature size corresponds to the finite width of the fine slit which is convoluted with the FTH point spread function. Considering Gaussian transmission profiles of slit and reference, we estimate a resolution limit of 48±8 nm (FWHM). In Fig. 5.5 (d) we show the reconstructed wave field (real part) along the slice marked by the red line in Fig. 5.5 (c) for different numerical propagation distances of the reconstruction. The data plotted in Fig. 5.5 (a) is thus identical to a transverse line profile at zero propagation distance in Fig. 5.5 (d). A longitudinal line profile (dotted blue line) is extracted on the right side of Fig. 5.5

(d). The depth-of-field, identified by a 20% drop of the reconstructed real part [Att07] is determined to be ±1.2 µm.‡

From the quantitave assessment of the longitudinal position of the reconstructed features, we are able to compile a 3D model of our object. As in-focus features are distinguished visually by the appearance or disappearance of fringes at their edges, we aim to identify these edges and their respective longitudinal height in a second step. The edges were found by computing the variance of the real parts in a 9 x 9 pixel matrix (corresponding to 225 µm x 225 µm) that was shifted pixelwise across the whole reconstruction resulting in 2D variance map. These variance maps were calculated for different propagation lengths. The presence of edges within the depth-of-field results in a strong increase in variance [Ma04] and corresponding pixels could be isolated by simply thresholding the variance map. The resulting wireframe style 3D model maps the specimen edges at their respective longitudinal positions and is presented in Fig. 5.6 (a). A visualisation of the 3D surface topography information in a 2D plot is illustrated in Fig. 5.6 (b).

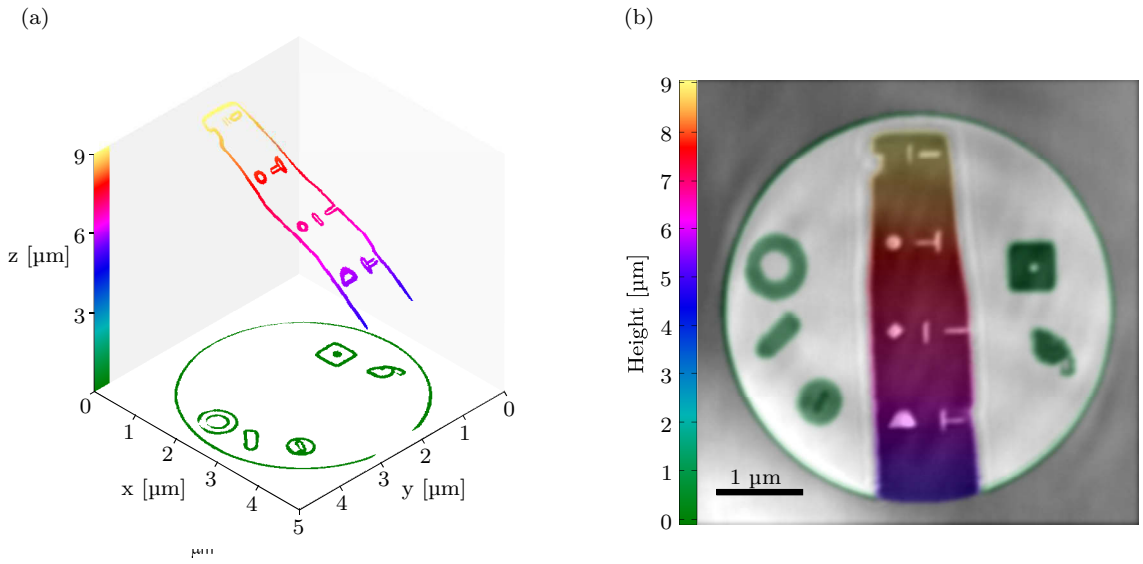

Figure 5.6: 3D representations of the reconstructions at different longitudinal coordinate z ("height"). (a) Wireframe model only displaying feature boundaries at their respective in-focus propagation distance relative to the mask plane. (b) Color-coded representation of the longitudinal coordinate of the test sample surface. For object parts not placed close to sharp features (such as the non-structured parts in the center of the ramp) the height coordinate was obtained by interpolation.

Here, we have combined reconstructions for different propagation lengths into an entirely focused, color-coded reconstruction. The color overlay in this reconstruction corresponds to the longitudinal height of the particular feature while the local image brightness still

corresponds to the reconstructed specimen wave field (real part). The longitudinal feature positions are taken from the model presented in Fig. 5.6 (a) and were interpolated between feature boundaries. The longitudinal position of edges from strongly absorbing features as plotted in Fig. 5.6 corresponds to distance from the FTH mask where the respective edge first intercepts the beam. Once a strong absorber brings the beam to extinction, no information on downstream objects shadowed in this way can be obtained. This is a principal limitation and fully analogous the situation encountered when recording focus series in microscopy, e.g. using visible light. For this reason, specimen that are best dedicated for this 3D imaging method show features that are well separated or semi-transparent. ♯

As expected from the geometry of the experimental setup, the lateral resolution is far superior to the longitudinal resolution limit. The measured depth-of-field in the experiment deviates considerably from the predicted lower boundary of relation (5.1) for two reasons. Firstly, the feature used for the evaluation of the depth-of-field is not point-like but has a finite width of 43 ± 7 nm. In the reconstruction, the intensity profile through the slit is wider than the profile of the point spread function of the FTH imaging process. As a consequence, the depth-of-field of the FTH setup is overestimated. Secondly, the detection of the hologram is affected by noise of the CCD and the limited photon statistic, in particular, at high scattering angles (cf. Fig. 5.3). The phase-encoding interference signal on the detector is not recorded with sufficient signal-to-noise ratio up to the given zero-intensity boundary of the reference wave's Airy disk at $q_{\mathrm{zero}} = 96\ \mu\mathrm{m}^{-1}$ (white circle in Fig. 5.3 (b)). Instead, the effective maximum scattering angle up to which the hologram is modulated will be smaller, resulting in a larger depth-of-field The effective maximum momentum transfer of qmax= 73 $\mu\mathrm{m}^{-1}$ considering both the finite feature width and the detection limitations is shown as red circle in Fig. 5.3 (b). It can be concluded that the true effective depth-of-field of the FTH setup considering hologram signal-to-noise (and not considering the limitations of the finite test feature) lies between 0.7 µm and 1.2 µm.

Relation (5.1) for Δz above also suggests that the longitudinal resolution can be improved by using lower photon energies while still maintaining sub-100 nm lateral resolution. For instance, the lower boundary for the longitudinal resolution reduces to $\Delta z = \pm 159$ nm when the FTH mask in this experiment would have been illuminated with a wavelength of $\lambda = 13.5$ nm, i.e., a prominent wavelength for destructive single-shot experiments at the free-electron laser in Hamburg (FLASH) [Ack07; Sei10].♯

5.4 Conclusion

We demonstrate the extraction of depth information from a single soft-X-ray Fourier transform hologram. Our approach allows a precise and intuitive measurement of longitudinal displacements of object features, analogous to a focus series "through an object" in light microscopy. Using this information, we are able to reconstruct a 3D model of a test object. In the reconstruction, we estimate a lateral resolution of 50 nm and a

longitudinal resolution of ±1.2 µm. The depth resolution can significantly be improved by either increasing the wavelength of the X-ray illumination or by further reducing the size of the reference wave source, given that the coherent photon flux and the resulting signal-to-noise ratio is not a limiting factor. As the method is compatible to FTH with more complex reference structures for increased efficiency, [Gei14b; Mar08] a reduction of the reference wave intensity when reducing the reference aperture diameter can be compensated to optimize the hologram fringe visibility.♯

Given the limitations of the approach demonstrated here as compared to obtaining 3D information via tomography [Gue12; Wei00], we anticipate the application of this 3D imaging method especially for weakly absorbing samples, e.g. for research in life science, in situations where the acquisition of many projection images is not possible. In particular, this is the case when the sample is structurally changing in time due to dynamic processes such as inherent or triggered dynamics or radiation damage. In this case, our approach allows to obtain 3D information on the sample from a single-view snapshot hologram in a diffract-before-destruct [Cha06a; Sei10] approach.♯

6 Summary and Outlook

FTH is a powerful, lensless imaging method with numerous application possibilities in physics, material science and biology. As the source of the reference beam, FTH comprises a small pinhole which is monolithically integrated into a metal film next to an object aperture that defines the field-of-view [Eis04]. Due to this integrated mask design, the optical setup is very simple and the method is remarkably robust against sample drifts and vibrations. By illuminating such an integrated mask with coherent X-rays, the hologram can conveniently be recorded on a CCD detector placed in the far-field. Contrary to non-holographic CDI where the phase information of the object wave is iteratively anticipated from a far-field, intensity diffraction pattern [Die10; Mia02; Pfe06], a hologram represents a direct measurement of the object wave's complex amplitude, i.e., amplitude and phase information of the object wave. The reconstruction of the recorded hologram is therefore a unique solution which is numerically accomplished by a Fourier transform. Contrary to lens based microscopy where the image represents a spatial distribution of intensities, the holographic reconstruction reproduces the complex amplitude of the object wave in the plane of the integrated mask.

The efficiency of FTH depends largely on the extent of the source of the reference wave. For common configurations with pinhole references, the reference pinhole's exit wave approximates the FTH system's point-spread function. For smaller references, the resolution of the FTH reconstruction thus improves whereas the reference signal on the detector and ultimately the image contrast in the reconstruction diminishes. For this reason, the choice of the reference pinhole's diameter is a compromise that trades photon efficiency for image resolution. One aspect of this dissertation is the formulation of a theoretical framework that allows a determination of the resolving capabilities for an FTH configuration dependent on basic design parameters. For a convenient discussion of an FTH setup, these basic design parameters have been combined in a single quality factor (R_{Airy}), i.e., the ratio of the diameter of the Airy disk from the reference wave relative to the side length of the (quadratic) detector. Nearly diffraction limited FTH configurations correspond to $R_{\mathrm{Airy}} \ll 1$ and the imaging properties of such a setup are characterized by the shape of the CCD detector. For larger R_{Airy} the reference source increasingly affects the reconstruction which for $R_{\mathrm{Airy}} \gg 1$ is sufficiently characterized by the reference pinhole alone. An optimal configuration of the FTH setup is found for $R_{\mathrm{Airy}} = 1$. This configuration represents a reasonable compromise between photon efficiency and spatial resolution limit.

For strongly reference limited setups, imaging artifacts are identified and characterized. For such configurations, it is demonstrated that a numeric low-pass filter can be applied

to the hologram to improve the image quality and to prevent imaging artifacts. In addition, it is also demonstrated that the reference beam of strongly reference limited FTH configurations is not optimally confined in the reconstruction plane of the reference pinhole, i.e., in the holographic reconstruction as retrieved by the Fourier transform of the hologram. The resolution of strongly reference limited holograms can therefore be enhanced by propagating the reconstructed object wave along the beam axis into a plane of least confusion. The theoretically expectable photon efficiency by an application of this approach however is much reduced compared to conventional FTH and a practical application of the method does not seem beneficial. Another more promising approach to enhance the image resolution in the reconstruction is to characterize and directly modify the FTH transfer function in reciprocal space. This approach allows to improve the resolution of a pinhole based FTH reconstruction without decreasing the photon efficiency of the FTH system. By performing a proof-of-principle FTH experiment with soft X-ray synchrotron radiation, the existence of the imaging artifacts anticipated for reference limited holograms as well as the effectiveness of the proposed numeric treatments to enhance the image quality are demonstrated. Characterizing and modifying the FTH transfer function utilizing a dedicated test pattern which is fabricated adjacent to the object aperture into the integrated mask is a promising outlook with significantly enhanced resolution limits for future FTH experiments.

The efficiency of FTH can drastically be improved by implementing a new and innovative mask design. Instead of a reference pinhole, this novel mask layout relies on a focusing FZP which serves as reference structure. The corresponding new holographic imaging method is another key aspect of this dissertation. Similar to the conventional, pinhole reference, the FZP is directly fabricated into the metal mask adjacent to the object. Due to this monolithic design, FTH is very robust against sample drifts and vibrations. In contrast to the conventional, pinhole based mask design where the FTH system's point-spread function is related to the mask plane, an FZP based reference beam is monolithically focused into several focal planes. In order to obtain a focused image, the reconstructed complex amplitude of the object needs to be numerically propagated from a particular FZP focus to the mask plane. After propagation, the particular focal order reconstruction is focused but superposed by the defocused contributions of the remaining FZP focal orders. The reconstruction algorithm for FTH with monolithically focusing references thus includes an additional processing step that separates the desired focal order reconstruction from the remaining defocused focal order contributions. This newly developed, iterative method further defocusses the undesired focal order plane contributions until the image background is sufficiently homogenous. Focused reconstructions of different diffraction orders can be added to a combined reconstruction with enhanced image contrast. The efficiency of FTH with monolithically focusing references is demonstrated by a proof-of-principle experiment with soft X-ray synchrotron radiation. Both, image contrast and resolution are significantly enhanced compared to conventional, pinhole based FTH. The method prospects dynamic single shot FTH experiments with high resolution and strong contrast. Due to the vibration robustness, the method gives also prospect to FTH experiments

with long exposure times at low flux facilities such as HHG sources. Another promising outlook for synchrotron experiments is to utilize the FZP's higher diffraction orders to improve the spatial resolution of the reconstruction beyond the FZP outermost zone width. Since the FZP diffraction efficiency declines for higher orders, exposure times for higher order imaging significantly increase [Reh09]. For this reason, an FTH experiment that capitalizes on higher FZP diffraction orders benefits from the vibration robustness of the FTH method. The signal of a higher order reference beam can be improved by utilizing a dedicated FZP design [Sch97].

Another major topic of this dissertation is the exploitation of the holographically recorded phase information to obtain structural information of three-dimensional specimen from the hologram. The reconstruction of the object exit wave's complex amplitude in the plane of the integrated mask can numerically be propagated along the beam axis. By this approach, the focus plane in the reconstruction is effectively separated from the point reference in the plane of the integrated mask. Features of extended three-dimensional specimen outside the depth-of-field can thus be refocused by numeric wave field propagation. The finite depth-of-field is used to measure the displacement of the particular feature from the mask plane. For such measurements, the resolution along the propagation axis is set by the FTH system's depth-of-field. The wave front retrieved by numeric wave propagation is thereby an anticipation that implies a homogenous phase velocity throughout the specimen. For potential applications with inhomogeneous phase velocities such as FTH bio-imaging in the water window, distortions of the numerically anticipated object wave reconstruction are however estimated to be much below the resolution limits of common FTH setups. Contrary to tomographic approaches [Gue12], the propagation method extracts three-dimensional information from a single view measurement. The method is experimentally demonstrated by utilizing an artificial, three-dimensional test structure which is illuminated with coherent synchrotron radiation of 400 eV photon energy. The structural information obtained from a single exposure hologram are combined in a three-dimensional model of the test structure. In the reconstruction, the spatial resolution in the direction lateral to the beam axis is 55 nm whereas the resolution in beam direction is determined to 1.2 µm. The depth resolution along the propagation direction in the reconstruction of the recorded hologram is thus far inferior to the lateral resolution. For applications with soft X-ray illumination light, the method can be seen as a complementary approach to extract depth information when tomographic methods are impractical or impossible. The depth resolution is expected to improve for lower photon energies [Gei14a] and a repetition of the experiment with EUV energies prospects an isotropic spatial resolution limit significantly below 100 nm. Another interesting perspective is to perform a similar experiment in reflection geometry. In such an experiment, the phase information in the reconstruction can be expected to interferometically encode the three-dimensional structure of the specimen and depth information should be extractable with an accuracy in the order of the wave length of the illumination light.

The integrated mask design as first demonstrated ten years ago [Eis04], represented a kick start for a new class of coherent X-ray imaging experiments. During the past years,

the method has been constantly developed and FTH is now routinely applied to numerous experiments, predominantly to investigate magnetic thin films [Büt13; Büt14; Kor14; Pfa11; Pfa12; Sch13]. The scientific insights of magnetism and its dynamics is an interesting research area with promising potential for industrial applications. Efficient reference schemes [Gei14b; Mar08; Sch06] in conjunction with FELs already enable future FTH experiments with unprecedented temporal and spatial resolutions. Combining CXI and FTH is a promising path to gain diffraction limited resolution on a photon budget [Mar08] or over a wide field of view [Hes14]. New technical developments like X-ray detectors with short readout times [Kis13] promise holograms with drastically enhanced dynamic ranges. Increasingly powerful computers provides additional means for the development of coherent lensless imaging methods by facilitating numerically demanding reconstructions in ever shorter processing times. For this reasons, FTH can be expected to continue strengthening it's established position in the future by routinely offering quality X-ray images with nanometer resolution on ultra-short timescales.

Bibliography

[Abb73] E. Abbe, 'Beiträge zur Theorie des Mikroskops und der mikroskopischen Wahrnehmung', *Archiv für Mikroskopische Anatomie* **9**, 413–418 (Dec. 1873), DOI: 10.1007/BF02956173 (cit. on p. 13).

[Ack07] W. Ackermann, G. Asova, V. Ayvazyan, et al., 'Operation of a free-electron laser from the extreme ultraviolet to the water window', *Nature Photonics* **1**, 336–342 (June 2007), DOI: 10.1038/nphoton.2007.76 (cit. on p. 71).

[Amb56] E. J. Ambrose, 'A Surface Contact Microscope for the study of Cell Movements', *Nature* **178**, 1194–1194 (Nov. 1956), DOI: 10.1038/1781194a0 (cit. on p. 13).

[Att07] D. T. Attwood, 'Soft X-Rays and Extreme Ultraviolet Radiation: Principles and Applications', 1st, Cambridge University Press, 2007 (cit. on pp. 1, 8, 9, 20, 32, 49, 51, 52, 55, 59, 63, 64, 70).

[Bod09] R. Boddy and G. Smith, 'Statistical Methods in Practice: For Scientists and Technologists', John Wiley & Sons, 2009 (cit. on p. 41).

[Bor99] M. Born and E. Wolf, 'Principles of Optics: Electromagnetic Theory of Propagation, Interference and Diffraction of Light', 7th, Cambridge University Press, 1999 (cit. on p. 21).

[Bra51] W. L. Braff and G. L. Rogers, 'Elimination of the Unwanted Image in Diffraction Microscopy', *Nature* **167**, 190–191 (Feb. 1951), DOI: 10.1038/167190a0 (cit. on p. 54).

[Bry68] O. Bryngdahl and A. Lohmann, 'Single-Sideband Holography', *Journal of the Optical Society of America* **58**, 620 (May 1968), DOI: 10.1364/JOSA.58.000620 (cit. on p. 54).

[Bur01] W. E. Burns, 'The Scientific Revolution: An Encyclopedia', 1st editio, ABC-CLIO, 2001 (cit. on p. 1).

[Büt13] F. Büttner, C. Moutafis, A. Bisig, et al., 'Magnetic states in low-pinning high-anisotropy material nanostructures suitable for dynamic imaging', *Physical Review B* **87**, 134422 (Apr. 2013), DOI: 10.1103/PhysRevB.87.134422 (cit. on pp. 11, 76).

[Büt14] F. Büttner, C. Moutafis, M. Schneider, et al., 'Topological mass of magnetic Skyrmions', *submitted* (2014) (cit. on p. 76).

[Cha12] W Chao, P Fischer, T Tyliszczak, S Rekawa, E Anderson, and P Naulleau, 'Real space soft x-ray imaging at 10 nm spatial resolution.', *Optics express* **20**, 9777–83 (Apr. 2012) (cit. on pp. 2, 11, 51, 59).

[Cha06a] H. N. Chapman, A. Barty, M. J. Bogan, et al., 'Femtosecond diffractive imaging with a soft-X-ray free-electron laser', *Nature Physics* **2**, 839–843 (Nov. 2006), DOI: 10.1038/nphys461 (cit. on pp. 2, 61, 72).

[Cha06b] H. N. Chapman, A. Barty, S. Marchesini, et al., 'High-resolution ab initio three-dimensional x-ray diffraction microscopy', *Journal of the Optical Society of America A* **23**, 1179 (2006), DOI: 10.1364/JOSAA.23.001179 (cit. on p. 61).

[Cha07] H. N. Chapman, S. P. Hau-Riege, M. J. Bogan, et al., 'Femtosecond time-delay X-ray holography.', *Nature* **448**, 676–9 (Aug. 2007), DOI: 10.1038/nature06049 (cit. on pp. 51, 60, 61).

[Che09] W. Chen, C. Quan, and C. J. Tay, 'Extended depth of focus in a particle field measurement using a single-shot digital hologram', *Applied Physics Letters* **95**, 201103 (2009), DOI: 10.1063/1.3263141 (cit. on pp. 67, 68).

[Die10] M. Dierolf, A. Menzel, P. Thibault, P. Schneider, C. M. Kewish, R. Wepf, O. Bunk, and F. Pfeiffer, 'Ptychographic X-ray computed tomography at the nanoscale.', *Nature* **467**, 436–9 (Sept. 2010), DOI: 10.1038/nature09419 (cit. on pp. 61, 73).

[Dub99] F. Dubois, L. Joannes, and J.-C. Legros, 'Improved Three-Dimensional Imaging with a Digital Holography Microscope With a Source of Partial Spatial Coherence', *Applied Optics* **38**, 7085 (Dec. 1999), DOI: 10.1364/AO.38.007085 (cit. on p. 61).

[Dub06] F. Dubois, C. Schockaert, N. Callens, and C. Yourassowsky, 'Focus plane detection criteria in digital holography microscopy by amplitude analysis.', *Optics express* **14**, 5895–5908 (2006) (cit. on p. 68).

[Eis04] S Eisebitt, J Lüning, W. F. Schlotter, M Lörgen, O Hellwig, W Eberhardt, and J Stöhr, 'Lensless imaging of magnetic nanostructures by X-ray spectro-holography.', *Nature* **432**, 885–8 (Dec. 2004), DOI: 10.1038/nature03139 (cit. on pp. 2, 10, 14, 52, 61, 66, 73, 75).

[Gab48] D. Gabor, 'A New Microscopic Principle', *Nature* **161**, 777–778 (May 1948), DOI: 10.1038/161777a0 (cit. on pp. 5, 51).

[Gau10] D. Gauthier, M. Guizar-Sicairos, X. Ge, W. Boutu, B. Carré, J. R. Fienup, and H. Merdji, 'Single-shot Femtosecond X-Ray Holography Using Extended References', *Physical Review Letters* **105**, 093901 (Aug. 2010), DOI: 10.1103/PhysRevLett.105.093901 (cit. on p. 51).

[Gei14a] J. Geilhufe, C. Tieg, B. Pfau, C. M. Günther, E. Guehrs, S. Schaffert, and S. Eisebitt, 'Extracting depth information of 3-dimensional structures from a single-view X-ray Fourier-transform hologram', *Optics Express* **22**, 24959 (Oct. 2014), DOI: 10.1364/OE.22.024959 (cit. on pp. 75, 87).

[Gei14b] J Geilhufe, B Pfau, M Schneider, et al., 'Monolithic focused reference beam X-ray holography.', *Nature communications* **5**, 3008 (Jan. 2014), DOI: 10.1038/ncomms4008 (cit. on pp. 62, 72, 76, 87).

[Gil89] J. Gillespie and R. A. King, 'The use of self-entropy as a focus measure holography in digital', **9**, 19–25 (1989) (cit. on p. 68).

[Goo96] J. W. Goodman, 'Introduction to Fourier Optics McGraw-Hill Series in Electrical and Computer Engineering', 2nd, Mc. Graw-Hill, 1996 (cit. on pp. 5, 14, 18–20, 32, 34, 49, 52, 62, 67).

[Gor11] T Gorniak, R Heine, a. P. Mancuso, et al., 'X-ray holographic microscopy with zone plates applied to biological samples in the water window using 3rd harmonic radiation from the free-electron laser FLASH.', *Optics express* **19**, 11059–70 (June 2011) (cit. on p. 52).

[Gue09] E. Guehrs, C. M. Günther, R. Könnecke, B. Pfau, and S. Eisebitt, 'Holographic soft X-ray omni-microscopy of biological specimens.', *Optics express* **17**, 6710–6720 (2009) (cit. on pp. 2, 11).

[Gue10] E. Guehrs, C. M. Günther, B. Pfau, T. Rander, S. Schaffert, W. F. Schlotter, and S. Eisebitt, 'Wavefield back-propagation in high-resolution X-ray holography with a movable field of view.', *Optics express* **18**, 18922–18931 (2010) (cit. on pp. 2, 11, 52, 62).

[Gue12] E. Guehrs, A. M. Stadler, S. Flewett, S. Frömmel, J. Geilhufe, B. Pfau, T. Rander, S. Schaffert, G. Büldt, and S. Eisebitt, 'Soft x-ray tomoholography', *New Journal of Physics* **14**, 013022 (Jan. 2012), DOI: 10.1088/1367-2630/14/1/013022 (cit. on pp. 2, 11, 61, 72, 75).

[Gün08] C. M. Günther, F Radu, A Menzel, S Eisebitt, W. F. Schlotter, R Rick, J. Lüning, and O Hellwig, 'Steplike versus continuous domain propagation in Co/Pd multilayer films', *Applied Physics Letters* **93**, 72505 (2008), DOI: 10.1063/1.2968305 (cit. on p. 2).

[Gün10] C. M. Günther, O. Hellwig, A. Menzel, et al., 'Microscopic reversal behavior of magnetically capped nanospheres', *Physical Review B* **81**, 064411 (Feb. 2010), DOI: 10.1103/PhysRevB.81.064411 (cit. on pp. 2, 11, 60).

[Gün11] C. M. Günther, B. Pfau, R. Mitzner, et al., 'Sequential femtosecond X-ray imaging', *Nature Photonics* **5**, 99–102 (Jan. 2011), DOI: 10.1038/nphoton.2010.287 (cit. on pp. 60, 61).

[Gus05] M. G. L. Gustafsson, 'Nonlinear structured-illumination microscopy: wide-field fluorescence imaging with theoretically unlimited resolution.', *Proceedings of the National Academy of Sciences of the United States of America* **102**, 13081–6 (Sept. 2005), DOI: 10.1073/pnas.0406877102 (cit. on p. 13).

[Hau08] T. Hauet, C. Günther, B. Pfau, M. Schabes, J.-U. Thiele, R. Rick, P. Fischer, S. Eisebitt, and O. Hellwig, 'Direct observation of field and temperature induced domain replication in dipolar coupled perpendicular anisotropy films', *Physical Review B* **77**, 184421 (May 2008), DOI: 10.1103/PhysRevB.77.184421 (cit. on p. 2).

[Hec02] E. Hecht, 'Optics', 4th Editio, vol. 48, *1*, San Francisco: Addison Wesley, 2002, 5 (cit. on p. 23).

[Hec98] J. M. Heck, D. T. Attwood, W Meyer-Ilse, and E. H. Anderson, 'Resolution determination in X-ray microscopy: an analysis of the effects of partial coherence and illumination spectrum.', *Journal of X-ray science and technology* **8**, 95–104 (Jan. 1998) (cit. on pp. 20, 23).

[Hei11] R Heine, T Gorniak, T Nisius, C Christophis, M. E. Pettitt, F Staier, T Wilhein, S Rehbein, M Grunze, and A Rosenhahn, 'Digital in-line X-ray holography with zone plates.', *Ultramicroscopy* **111**, 1131–6 (July 2011), DOI: 10.1016/j.ultramic.2011.02.002 (cit. on p. 52).

[Hel94] S. W. Hell and J Wichmann, 'Breaking the diffraction resolution limit by stimulated emission: stimulated-emission-depletion fluorescence microscopy.', *Optics letters* **19**, 780–2 (June 1994) (cit. on p. 13).

[Hes14] P. Hessing, 'Holography guided ptychography with soft X-rays', *TU Berlin, Diplomarbeit* (2014) (cit. on p. 76).

[Kir74] J. Kirz, 'Phase zone plates for x rays and the extreme uv', *Journal of the Optical Society of America* **64**, 301 (Mar. 1974), DOI: 10.1364/JOSA.64.000301 (cit. on p. 52).

[Kis13] S Kishimoto, H Yonemura, S Adachi, S Shimazaki, M Ikeno, M Saito, T Taniguchi, and M Tanaka, 'A fast X-ray detector using silicon avalanche photodiodes of 64-pixel linear array', *Journal of Physics: Conference Series* **425**, 062007 (Mar. 2013), DOI: 10.1088/1742-6596/425/6/062007 (cit. on p. 76).

[Kor14] C. V. Korff Schmising, B. Pfau, M. Schneider, et al., 'Imaging Ultrafast Demagnetization Dynamics after a Spatially Localized Optical Excitation', *Physical Review Letters* **112**, 217203 (May 2014), DOI: 10.1103/PhysRevLett.112.217203 (cit. on p. 76).

[Lat07] T. Latychevskaia and H.-W. Fink, 'Solution to the Twin Image Problem in Holography', *Physical Review Letters* **98**, 233901 (June 2007), DOI: 10.1103/PhysRevLett.98.233901 (cit. on p. 54).

[Loh12] N. D. Loh, C. Y. Hampton, A. V. Martin, et al., 'Fractal morphology, imaging and mass spectrometry of single aerosol particles in flight.', *Nature* **486**, 513–7 (June 2012), DOI: 10.1038/nature11222 (cit. on p. 61).

[Ma04] L. Ma, H. Wang, Y. Li, and H. Jin, 'Numerical reconstruction of digital holograms for three-dimensional shape measurement', *Journal of Optics A: Pure and Applied Optics* **6**, 396–400 (Apr. 2004), DOI: 10.1088/1464-4258/6/4/016 (cit. on pp. 68, 70).

[Mal13] E. B. Malm, N. C. Monserud, C. G. Brown, P. W. Wachulak, H. Xu, G. Balakrishnan, W. Chao, E. Anderson, and M. C. Marconi, 'Tabletop single-shot extreme ultraviolet Fourier transform holography of an extended object', **21**, 9959–9966 (2013), DOI: 10.1364/OE.21.009959 (cit. on pp. 10, 52).

[Mar08] S. Marchesini, S. Boutet, A. E. Sakdinawat, et al., 'Massively parallel X-ray holography', *Nature Photonics* **2**, 560–563 (Aug. 2008), DOI: 10.1038/nphoton.2008.154 (cit. on pp. 2, 11, 51, 61, 72, 76).

[McE08] C. P. McElhinney, B. M. Hennelly, and T. J. Naughton, 'Twin-image reduction in inline digital holography using an object segmentation heuristic', *Journal of Physics: Conference Series* **139**, 012014 (Nov. 2008), DOI: 10.1088/1742-6596/139/1/012014 (cit. on p. 54).

[McN92] I McNulty, J Kirz, C Jacobsen, E. H. Anderson, M. R. Howells, and D. P. Kern, 'High-Resolution Imaging by Fourier Transform X-ray Holography.', *Science (New York, N.Y.)* **256**, 1009–12 (May 1992), DOI: 10.1126/science.256.5059.1009 (cit. on pp. 8, 10, 52, 61).

[Mia02] J. Miao, T. Ishikawa, B. Johnson, E. Anderson, B. Lai, and K. Hodgson, 'High Resolution 3D X-Ray Diffraction Microscopy', *Physical Review Letters* **89**, 088303 (Aug. 2002), DOI: 10.1103/PhysRevLett.89.088303 (cit. on pp. 61, 73).

[Mon14] N. C. Monserud, E. B. Malm, P. W. Wachulak, V. Putkaradze, G. Balakrishnan, W. Chao, E. Anderson, D. Carlton, and C Mario, 'Recording oscillations of sub-micron size cantilevers by extreme ultraviolet Fourier transform holography', **22**, 4161–4167 (2014), DOI: 10.1364/OE.22.004161 (cit. on p. 63).

[Ove12] J. Overbuschmann, J. Hengster, S. Irsen, and T. Wilhein, 'Fabrication of Fresnel zone plates by ion-beam lithography and application as objective lenses in extreme ultraviolet microscopy at 13 nm wavelength', *Optics letters* **37**, 5100–5102 (2012), DOI: 10.1364/OL.37.005100 (cit. on p. 59).

[Pag06] D. M. Paganin, 'Coherent X-ray Optics', 2006 (cit. on pp. 12, 32, 52, 61, 62, 67).

[Pfa10] B Pfau, C. M. Günther, S Schaffert, et al., 'Femtosecond pulse x-ray imaging with a large field of view', *New Journal of Physics* **12**, 095006 (Sept. 2010), DOI: 10.1088/1367-2630/12/9/095006 (cit. on pp. 51, 61).

[Pfa11] B. Pfau, C. M. Günther, E. Guehrs, et al., 'Origin of magnetic switching field distribution in bit patterned media based on pre-patterned substrates', *Applied Physics Letters* **99**, 062502 (2011), DOI: 10.1063/1.3623488 (cit. on pp. 2, 11, 76).

[Pfa12] B Pfau, S Schaffert, L Müller, et al., 'Ultrafast optical demagnetization manipulates nanoscale spin structure in domain walls.', *Nature communications* **3**, 1100 (Jan. 2012), DOI: 10.1038/ncomms2108 (cit. on p. 76).

[Pfe06] M. A. Pfeifer, G. J. Williams, I. A. Vartanyants, R. Harder, and I. K. Robinson, 'Three-dimensional mapping of a deformation field inside a nanocrystal.', *Nature* **442**, 63–6 (July 2006), DOI: 10.1038/nature04867 (cit. on pp. 61, 73).

[Rai10] K. S. Raines, S. Salha, R. L. Sandberg, H. Jiang, J. A. Rodríguez, B. P. Fahimian, H. C. Kapteyn, J. Du, and J. Miao, 'Three-dimensional structure determination from a single view.', *Nature* **463**, 214–7 (Jan. 2010), DOI: 10.1038/nature08705 (cit. on p. 62).

[Rav09] A. Ravasio, D. Gauthier, F. Maia, et al., 'Single-Shot Diffractive Imaging with a Table-Top Femtosecond Soft X-Ray Laser-Harmonics Source', *Physical Review Letters* **103**, 028104 (July 2009), DOI: 10.1103/PhysRevLett.103.028104 (cit. on p. 51).

[Reh09] S. Rehbein, S. Heim, P. Guttmann, S. Werner, and G. Schneider, 'Ultrahigh-Resolution Soft-X-Ray Microscopy with Zone Plates in High Orders of Diffraction', *Physical Review Letters* **103**, 110801 (Sept. 2009), DOI: 10.1103/PhysRevLett.103.110801 (cit. on pp. 59, 75).

[Sch13] S. Schaffert, B. Pfau, J. Geilhufe, C. M. Günther, M. Schneider, C. V. Korff Schmising, and S. Eisebitt, 'High-resolution magnetic-domain imaging by Fourier transform holography at 21 nm wavelength', *New Journal of Physics* **15**, 093042 (Sept. 2013), DOI: 10.1088/1367-2630/15/9/093042 (cit. on pp. 54, 76).

[Sch06] W. F. Schlotter, R. Rick, K. Chen, et al., 'Multiple reference Fourier transform holography with soft x rays', *Applied Physics Letters* **89**, 163112 (2006), DOI: 10.1063/1.2364259 (cit. on pp. 44, 51, 60, 76).

[Sch97] G. Schneider, 'Zone plates with high efficiency in high orders of diffraction described by dynamical theory', *Applied Physics Letters* **71**, 2242 (1997), DOI: 10.1063/1.120069 (cit. on pp. 59, 75).

[Sch03] C. J. Schwarz, Y. Kuznetsova, and S. R. J. Brueck, 'Imaging interferometric microscopy.', *Optics letters* **28**, 1424–6 (Aug. 2003) (cit. on p. 13).

[Sei10] M. M. Seibert, S. Boutet, M. Svenda, et al., 'Femtosecond diffractive imaging of biological cells', *Journal of Physics B: Atomic, Molecular and Optical Physics* **43**, 194015 (Oct. 2010), DOI: 10.1088/0953-4075/43/19/194015 (cit. on pp. 2, 61, 71, 72).

[Sta08] L.-M. Stadler, C. Gutt, T. Autenrieth, O. Leupold, S. Rehbein, Y. Chushkin, and G. Grübel, 'Hard X Ray Holographic Diffraction Imaging', *Physical Review Letters* **100**, 245503 (June 2008), DOI: 10.1103/PhysRevLett.100.245503 (cit. on p. 51).

[Sti11] D. Stickler, R. Frömter, H. Stillrich, et al., 'Domain size in systems with canted magnetization', *Physical Review B* **84**, 104412 (Sept. 2011), DOI: 10.1103/PhysRevB.84.104412 (cit. on p. 11).

[Str85] N. Streibl, 'Three-dimensional imaging by a microscope', *Journal of the Optical Society of America A* **2**, 121 (Feb. 1985), DOI: 10.1364/JOSAA.2.000121 (cit. on p. 61).

[Str65] G. W. Stroke, 'Lensless Fourier-Transform Method for Optical Holography', *Applied Physics Letters* **6**, 201 (1965), DOI: 10.1063/1.1754131 (cit. on pp. 6, 7).

[Tho69] B. J. Thompson, 'IV Image Formation with Partially Coherent Light', **7**, 169–230 (1969), DOI: 10.1016/S0079-6638(08)70595-X (cit. on pp. 20–22).

[Wac10] P. W. Wachulak, M. C. Marconi, R. A. Bartels, C. S. Menoni, and J. J. Rocca, 'Holographic imaging with a nanometer resolution using compact table-top EUV laser', **18**, 80–90 (2010), DOI: 10.2478/s11772 (cit. on p. 63).

[Wan12] T. Wang, D. Zhu, B. Wu, et al., 'Femtosecond Single-Shot Imaging of Nanoscale Ferromagnetic Order in Co/Pd Multilayers Using Resonant X-Ray Holography', *Physical Review Letters* **108**, 267403 (June 2012), DOI: 10.1103/PhysRevLett.108.267403 (cit. on pp. 11, 51).

[Wei00] D Weiß, G Schneider, B Niemann, P Guttmann, D Rudolph, and G Schmahl, 'Computed tomography of cryogenic biological specimens based on X-ray microscopic images', *Ultramicroscopy* **84**, 185–197 (Aug. 2000), DOI: 10.1016/S0304-3991(00)00034-6 (cit. on pp. 61, 72).

[You72] M. Young, 'Zone Plates and Their Aberrations', *Journal of the Optical Society of America* **62**, 972 (Aug. 1972), DOI: 10.1364/JOSA.62.000972 (cit. on p. 54).

Publications

J. Geilhufe, B. Pfau, M. Schneider, F. Büttner, C.M. Günther, S. Werner, S. Schaffert, E. Guehrs, S. Frömmel, M. Kläui and S. Eisebitt "Monolithic focused reference beam X-ray holography" *Nature Communications* **5**, 3008 (2014). http://dx.doi.org/10.1038/ncomms4008

J. Geilhufe, C. Tieg, B. Pfau, C. M. Günther, E. Guehrs, S. Schaffert, and S. Eisebitt "Extracting depth information of 3-dimensional structures from a single-view X-ray Fourier-transform hologram" *Optics Express* **22**, 24959 (2014). http://dx.doi.org/10.1364/OE.22.024959

S. Schaffert, B. Pfau, J. Geilhufe, C. M. Günther, M. Schneider, C. von Korff Schmising and S. Eisebitt, "High-resolution magnetic-domain imaging by Fourier transform holography at 21 nm wavelength" *New J. Phys.* **15**, 093042 (2013). http://dx.doi.org/10.1088/1367-2630/15/9/093042

F. Büttner, C. Moutafis, A. Bisig, P. Wohlhüter, C. M. Günther, J.Mohanty, J. Geilhufe, M. Schneider, C. v. Korff Schmising, S.Schaffert, B. Pfau, M. Hantschmann, M. Riemeier, M. Emmel, S. Finizio, G. Jakob, M. Weigand, J. Rhensius, J. H. Franken, R. Lavrijsen, H. J. M. Swagten, H. Stoll, S. Eisebitt, and M. Kläui "Magnetic states in low-pinning high-anisotropy material nanostructures suitable for dynamic imaging " *Phys. Rev. B* **87**, 134422 (2013). http://dx.doi.org/10.1103/PhysRevB.87.134422

L. Müller, S. Schleitzer, C. Gutt, B. Pfau, S. Schaffert, J. Geilhufe, C. von Korff Schmising, M. Schneider, C. M. Günther, F. Büttner, F. Capotondi, E. Pedersoli, S. Düsterer, H. Redlin, A. Al-Shemmary, R. Treusch, J. Bach, R. Frömter, B. Vodungbo, J. Gautier, P. Zeitoun, H. Popescu, V. Lopez-Flores, N. Beaulieu, F. Sirotti, N. Jaouen, G. Malinowski, B. Tudu, K. Li, J. Lüning, H. P. Oepen, M. Kiskinova, S. Eisebitt and G. Grübel "Ultrafast Dynamics of Magnetic Domain Structures Probed by Coherent Free-Electron Laser Light" *Sync. Rad. News* **26**, 27-32 (2014). http://dx.doi.org/10.1080/08940886.2013.850384

L. Müller, C. Gutt, B. Pfau, S. Schaffert, J. Geilhufe, F. Büttner, J. Mohanty, S. Flewett, R. Treusch, S. Düsterer, H. Redlin, A. Al-Shemmary, M. Hille, A. Kobs, R. Frömter, H. P. Oepen, B. Ziaja, N. Medvedev, S.-K. Son, R. Thiele, R. Santra, B. Vodungbo, J. Lüning, S. Eisebitt, and G. Grübel "Breakdown of the X-Ray Resonant Magnetic Scattering Signal during Intense Pulses of Extreme Ultraviolet Free-Electron-Laser

Radiation" *Physical Review Letters* **110**, 234801 (2013). http://dx.doi.org/10.1103/PhysRevLett.110.234801

L. Müller, C. Gutt, S. Streit-Nierobisch, M. Walther, S. Schaffert, B. Pfau, J. Geilhufe, F. Büttner, S. Flewett, C. M. Günther, S. Eisebitt, A. Kobs, M. Hille, D. Stickler, R. Frömter, H. P. Oepen, J. Lüning, and G. Grübel "Endstation for ultrafast magnetic scattering experiments at the free-electron laser in Hamburg" *Rev. Sci. Instrum.* **84**, 013906 (2013). http://dx.doi.org/10.1063/1.4773543

B. Pfau, S. Schaffert, L. Müller, C. Gutt, A. Al-Shemmary, F. Büttner, R. Delaunay, S. Düsterer, S. Flewett1, R. Frömter, J. Geilhufe, E. Guehrs, C.M. Günther, R. Hawaldar, M. Hille, N. Jaouen, A. Kobs, K. Li, J. Mohanty, H. Redlin, W.F. Schlotter, D. Stickler, R. Treusch, B. Vodungbo, M. Kläui, H.P. Oepen, J. Lüning, G. Grübel, S. Eisebitt "Ultrafast optical demagnetization manipulates nanoscale spin structure in domain walls" *Nature Communications* **3**, 1100 (2012). http://dx.doi.org/10.1038/ncomms2108

S. Flewett, S. Schaffert, J. Mohanty, E. Guehrs, J. Geilhufe, C. M. Günther, B. Pfau, and S. Eisebitt "Method for Single-Shot Coherent Diffractive Imaging of Magnetic Domains" *Phsical Review Letters* **108**, 223902 (2012). http://dx.doi.org/10.1103/PhysRevLett.108.223902

E. Guehrs, A. M. Stadler, S. Flewett, S. Frömmel, J. Geilhufe, B. Pfau, T. Rander, S. Schaffert, G. Büldt and S. Eisebitt "Soft X-ray tomoholography" *New Journal of Physics* **14**, 013022 (2012). http://dx.doi.org/10.1088/1367-2630/14/1/013022

Acknowledgements

It was the exciting perspective to work on the relatively new field of lensless imaging methods for coherent X-rays that drove me to Berlin four years ago. Im very grateful to *Stefan Eisebitt* for giving me the great opportunity to be part of his group. Stefan is a very inspiring, motivational and supportive group leader who always encourages new ideas. I would like to acknowledge and thank him for constantly being a step ahead and for his ability to make complex ideas comprehensible. The work presented in this thesis would not have been possible without Stefan's ongoing support and the valuable help of many other people.

During the last four years, I truly enjoyed the creative and positive working atmosphere and I wish to thank the whole group. In particular, I would like to express my sincere gratitude to *Bastian Pfau* who was a great mentor from my early days in the group. His scientific thinking and his creative ideas always impressed and motivated me. He contributed a lot of great ideas to this work through sacrificing countless hours on the phone discussing imaging theory with me. I would not be where I am today without his patience and his generosity.

I am also deeply indebted to *Christian Günther*, *Erik Gührs* and *Stefan Schaffert*. Together with Bastian they first introduced me to the world of Fourier Transform holography experiments at BESSYII and patiently answered all of my questions. Many thanks also to *Felix Büttner* who was always a good source for scientific advice and never missed out to offer help. I also want to thank *Michael Schneider*, *Christian Günther* and *Stephan Werner* for producing the samples for the experiments. Chapter 4 and 5 of this thesis have recently been published in Ref. [Gei14b] and Ref. [Gei14a]. I therefore want to thank all co-authors for their valuable help and support.

Apart from the work as an experimental physicist, I had the chance to gather first hand experiences in designing experiments. On this account, I would like to express my deepest gratitude to my fellow colleague *Tino Noll* for providing many valuable insights and explanations in constructing experiments. Tino is an exceptionally creative design engineer who always strives to find the perfect solutions even when faced with the most challenging tasks. With Tino's continuous support, *Stefan Schaffert* and I were able to design a mobile experimental setup that was used not only for the experiments in this work but also for many others.

My sincere thanks also go to my co-adviser *Thomas Wilhein* for his continuous encouragement since my undergraduate studies. His passion for X-ray optics and holography was vividly transmitted through his exciting lectures. I thank him for his inspirations that finally led me to work in the field of Fourier transform X-ray holography.

Last but not least, I want to thank my family for their love and continuous support. Especially my dear wife *Neo* for always believing in me even when I doubted myself. I will forever be indebted to her continuous love and for her support in every possible way.